Mixing in a Novel Rocket Engine

Fiona Spencer

A dissertation

submitted in partial fulfillment of the

requirements for the degree of

Doctor of Philosophy

University of Washington
2025

Reading Committee:
Robert Breidenthal, Chair
James Hermanson
Dana Dabiri
Marco Salviato

Program Authorized to Offer Degree:
Aeronautics and Astronautics

University of Washington

Abstract

Mixing in a Novel Rocket Engine

Fiona Spencer

Chair of the Supervisory Committee:

Robert Breidenthal
Aeronautics and Astronautics

A novel rocket engine concept, based on a transverse combustor design, is explored and modeled using Computational Fluid Dynamics (CFD). The design utilizes both Direct Numerical Simulation (DNS) and Large Eddy Simulation (LES) to simulate the flows of fuel and oxidizer pairs over a simple cylindrical combustion chamber geometry.

Two nozzles, positioned radially along the upstream end of the cylinder, serve as inlets for the fuel and oxidizer reactants. Mixing is achieved by a pair of large, counter-rotating vortices. The mixing behavior is analyzed, both spatially and temporally, across transverse cross sections along the characteristic length of the chamber.

Cylinder lengths are varied to optimize the cavity, aiming for near-perfect mixing. The determination of regions where near perfect mixing occurs informs the design configurations of the transverse rocket engine chamber by optimizing the cavity length. This configuration is anticipated to be more cost effective to manufacture, lighter, and more reliable than existing designs.

Acknowledgments

I would like to express my sincere gratitude to my advisor, Dr. Robert Breidenthal, for his unwavering support, guidance, and encouragement throughout the duration of my research and thesis. His insightful feedback and constructive criticism have been invaluable to the success of this work. I also extend my appreciation to the individuals in my lab, Dr. Giovanni Nino and Dr. Janna Wai. Janna generously shared her expertise, teaching me tools that greatly accelerated my ability to generate results. Giovanni provided crucial technical feedback that refined my research.

I would further like to thank the members of my thesis committee for their valuable input and advice throughout this process. A special thank you goes to my family and friends for their endless love and support. To my husband, Herrick Spencer, for his constant encouragement, belief in my abilities, and patience during the countless hours I dedicated to this project.

Lastly, I am grateful to my colleagues and peers for making the research process both enjoyable and enriching. Their flexibility and support in creating a manageable work environment allowed me to continue pursuing my career while completing my degree.

Contents

List of Figures

List of Tables

Nomenclature

Symbols

$\overline{c}$	Mean concentration
c'	Concentration fluctuations
u'^2	Fluctuating velocity field in x direction
v'^2	Fluctuating velocity field in y direction
w'^2	Fluctuating velocity field in z direction
α	Thermal diffusivity
$\triangle x$	Spatial resolution
δ_H	Boundary layer thickness for hydrogen
δ_{O2}	Boundary layer thickness for oxygen
ϵ_H	Turbulent dissipation rate for hydrogen
ϵ_{O2}	Turbulent dissipation rate for oxygen
η	Kolmogorov length scale
μ	Dynamic viscosity

ν	Kinematic viscosity
$\overline{c}$	Average mass fraction concentration
$\overline{U}$	Average velocity
ϕ	Equivalency ratio
τ	Characteristic mixing time
τ_a	Acoustic transit time
τ_t	Thrust force duration
τ_v	Vortex rotation period
d	Inlet diameter
I	Turbulent intensity
k_H	Turbulent kinetic energy for hydrogen
k_{O2}	Turbulent kinetic energy for oxygen
l_{o_H}	Integral length scale for hydrogen
$l_{o_{O2}}$	Integral length scale for oxygen
l_o	Integral length scale
ε	Turbulent dissipation rate
a_t	Stagnation chamber speed of sound
c	Concentration
c_p	Specific heat

CFD Computational fluid dynamics

D Combustion chamber diameter

d Inlet diameter

DNS Direct numerical simulation

g Gravity

JANAF Joint Army, Navy and Air Force

k Turbulent kinetic energy

k_{RES} Kinetic energy of resolved eddies

k_{SGS} Turbulent kinetic energy

L Length of combustion chamber

LES Large eddy simulation

N Number of vortex rotations

PDF Probability density function

Re Reynolds number

Re_H Reynolds number hydrogen

Re_{O2} Reynolds number oxygen

U Velocity

U' Velocity fluctuations

Chapter 1: Introduction

The discovery of large scale structures by Brown & Roshko (1974) [1] has since led to extensive studies into the mixing and structure of self similar vortices. These flows are relatively simple when dealing with turbulence and provide a path towards studying more complex flows. Confining flows by means of a duct or pipe to study structure and mixing of the resulting flow is the next logical step [2]. Confinement may alter the flow in three ways. First, the vortex size is limited to the size of the duct. The second is that the vortices can no longer entrain fluid once they grow to fill the duct. Third, viscous effects may become important once the vortices fill the duct.

Industrial applications of confined vortices are broad, and the performance of the mixing can impact product quality and cost. Among the most important performance characteristics are mixer length and pressure loss. It is often desirable to have a shorter mixing length and small total pressure loss. For combustion, this can lead to a reduction in polluting emissions by minimizing the time required for complete combustion. There is extensive prior work on the axial injection rocket engine, but very little on a transverse injection chamber design.

Transverse jets into a combustion chamber is not a conventional choice for rocket engines. Conventional engines use axial jets, though with many disadvantages, including complexity from numerous nozzles, excessive weight, multiple failure modes, high cost, and complexity in fabrication. Leaks in the injector plate would lead to combustion in areas outside the combustion zone, thereby potentially damaging the engine. Other potential problems include erosion, melting, and explosions from combustion instabilities. In contrast, a transverse jet configuration would reduce

engineering and manufacturing complexity and weight and improve reliability.

Conventional bi-propellant rocket engines utilize many small injection nozzles for the two reactants. The turbulent eddies intended to accomplish the mixing are relatively small with short rotation periods, much shorter than the acoustic transit time across the combustion chamber. Rocket engines must be designed to avoid combustion instabilities that create destructive detonation waves capable of damaging the engine. One approach is to separate the mixing time scale from the wave transit time. In conventional engines, the vortex rotation period τ_v is much less than the acoustic transit time τ_a. In contrast, for the transverse rocket engine design, the inequality is reversed, and the vortex rotation period is much greater than the acoustic transit time.

$$\tau_v >> \tau_a \tag{1.1}$$

$$\tau_a = \frac{D}{a} \tag{1.2}$$

Here, a is the stagnation chamber speed of sound, and τ_a is the acoustic time across a combustion chamber of diameter D.

A novel engine configuration injects fuel and oxidizer radially inward into an axisymmetric combustion chamber near the upstream end. One nozzle is for the fuel, and the other is the oxidizer (Figure 1.1). Both nozzles are close to the upstream wall of the combustion chamber and pointed towards the chamber center. A minimum distance between the inlets and the upstream wall is maintained, as this area only serves as a recirculation region and is unlikely to act as anything but a flameholder. By placing the injection nozzles as far upstream as possible, the total streamwise length of the combustion chamber could be shortened, thereby minimizing the total weight and heat losses to the wall.

Large counter-rotating vortices are expected to grow and fill the combustion chamber, Figure 1.2. The mixed fluid resides within Taylor layers and within the cores of the large vortex pair

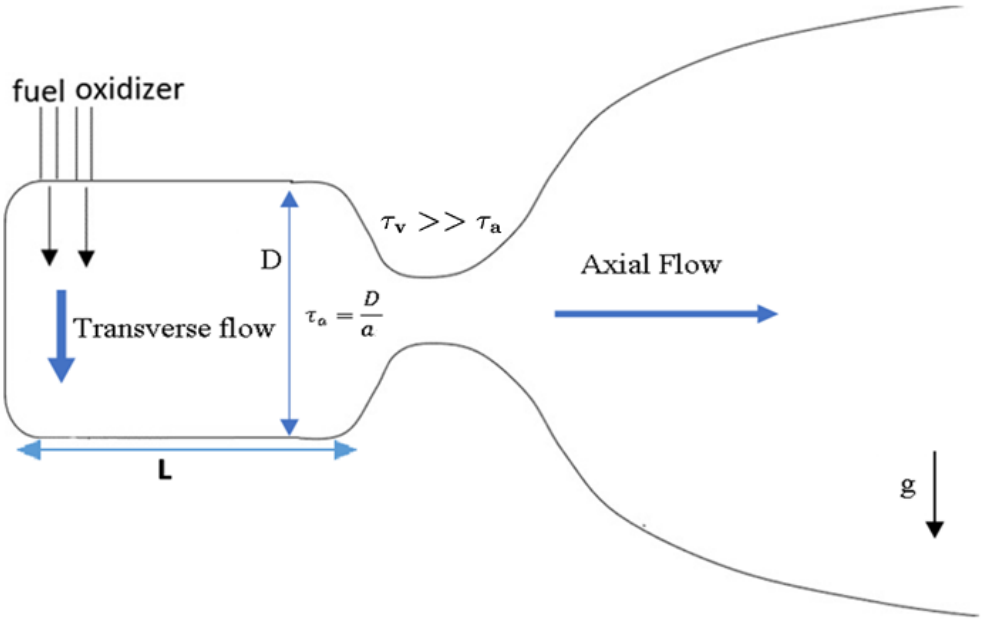

Figure 1.1: 2D de Laval nozzle modified for transverse injection

[3]. Experiments with transverse jets in a tube and a rectangular duct indicate that the mixing behavior of the vortices is largely insensitive to the cross sectional geometry [4, 5]. For a sufficiently long combustion chamber, there is no pure injected fluid remaining, as the fluid will be perfectly mixed.

A practical streamwise length L of the combustion chamber is a tradeoff between uniformity of mixing and the weight and size of the engine. The total amount of heat released by the combustion is increased by extending the length of the chamber, but this results in additional wall heat loss and an increase in engine weight.

Conventional wisdom is that a pure oxygen jet should not impinge on a hot surface in the combustion chamber. Otherwise, the wall will react with the oxygen and burn. The proposed new engine design has the potential to overcome this issue. The transverse oxygen jet does impinge on the opposite chamber wall. However, there is little mixed fluid at this early stage, so the impinging fluid is still cold. Consequently, the chamber wall there remains cool. Experimental results from Boening et al. [6] used a related transverse injection geometry to achieve mixing in a rotating

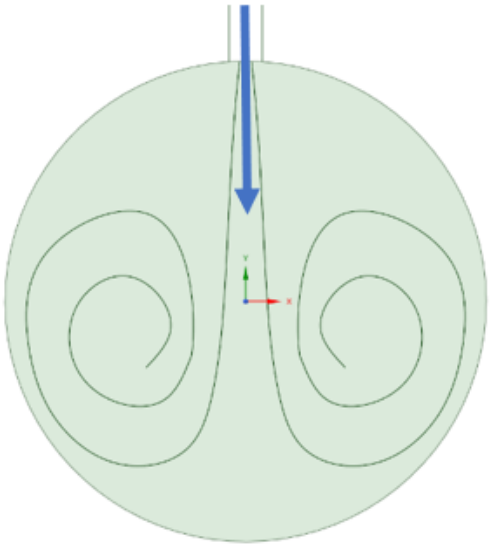

Figure 1.2: Cross section view of transverse injection flow

detonation wave engine. During the experiment, the upstream end plate of the engine remained cool. Lower thermal requirements for the combustion chamber offer the benefits of reducing the use of expensive materials, thicker walls, and/or time consuming manufacturing methods. As a result, the design of the transverse rocket engine will be more affordable and lighter in weight, depending on the performance metrics of the system.

1.1 Turbulent Mixing

The model for turbulent mixing relies on two assumptions [7]. The first is that any appreciable turbulent mixing requires a vortex to complete approximately one rotation. The second has the resulting mixed fluid residing in the vortex core, at the Batchelor layer, and in the Taylor layers. The mixed fluid resides in about equal amounts within the vortex cores and the nearby Taylor layers. The Taylor layer is the diffusive scale associated with the strain rate of the largest eddies. The Batchelor layer is the diffusive scale associated with the strain rate of the smallest eddies, which are at the Kolmogorov microscale. To the first order, mixed fluid resides within the vortex

cores [8]. Transverse jets are known to generate a pair of counter-rotating vortices [9]. There is no incident primary flow in the proposed transverse nozzle geometry, which differs from most of the previous work. An exception is the rotating detonation wave engine [10]. There are two central assumptions underlying the proposed new rocket design [4]:

Self-similar mixing

$$\frac{c'}{\overline{c}} = e^{-N} \tag{1.3}$$

Self-similar vorticity

$$N = \int \frac{dt}{t} \tag{1.4}$$

where N is the number of vortex rotations, $\overline{c}$ is the mean concentration of an inert scalar, c' is the rms width of the concentration peak. The theoretical model describes the evolution of the concentration field once all injected fluid has been mixed at least a little such that $t \gg \tau$. Concentration fluctuations can then be expressed as,

$$\frac{c'}{\overline{c}} = e^{-\int(\frac{dt}{t})} = \frac{\tau}{t} \tag{1.5}$$

From dimensional considerations, τ is the characteristic mixing time for confined mixing, which is proportional to the vortex rotation period when the vortex pair first fills the duct. For a 2D flow, it is the square root of the cube of the diameter D divided by the thrust per unit mass and per unit span.

Empirical results from Edwards et al. [4] were in accord with theory when all dimensionless constants in the equations were unity. However, in an analogous flow, Aarnio [2] found that the concentration fluctuations declined exponentially instead of inversely with time or downstream distance.

Chapter 2: Computational Model

The requirements on the computation domain must satisfy both computational and experimental complexity. A simple geometry as that of a circular cylinder, would reduce computational complexity. Similarly, a cylindrical geometry eliminates sharp edges within the nozzle that can lead to combustion instability. Fuel and oxidizer inlets maybe placed nearer to the upstream wall and radially to produce transverse flow. Varying the characteristic length of the cylinder allows for optimization of mixing within the chamber.

The Reynolds number must be kept low to reduce the computational complexity but high enough for turbulent flow. A Re of approximately 500 or slightly above would satisfy this condition. The flow would remain quasi-turbulent while maintaining a low spatial resolution. Using meshing tools as Ansys and Ennova CFD, a characteristic length of 0.09m at a spatial resolution of 5×10^{-5}m produces a mesh that is approximately 8Gb. Finer meshes present issues with quality, skewness, orthogonality, visualization, and simulation time increases to the point that timely design iterations are hindered. A mesh of L=0.09m and $\Delta x = 5 \times 10^{-5} m$ approaches the limit of what is feasible with a DNS simulation.

2.1 Design Parameters

Direct Numerical Simulation (DNS) is a computational fluid dynamics (CFD) technique to solve the Navier-Stokes equations without using any turbulence models. This means that all of the

spatial temporal scales of turbulence are resolved directly. DNS involves simulating the fluid flow by numerically solving for the Navier-Stokes simulations for every small scale of turbulence, from the smallest dissipative scales (Kolmogorov microscale) to the largest scales containing the most kinetic energy. This is the most robust and accurate simulation, but most computationally expensive. It requires significant computational resources, especially for high Re.

For DNS simulations, the smallest required scale to resolve is that of the smallest vortices, with a diameter on the order of the Kolmogorov length scale, η. Conventional wisdom is that to resolve such a flow, a mesh consisting of cells with lengths smaller than η is necessary to properly resolve a given flow. However, prior work by Moin and Mahesh [11] suggests this requirement might be too strict and the spatial resolution can be relaxed to $\mathcal{O}(\eta)$ rather than a fraction of it. For some of the DNS simulations, the cell diagonal can be as large as 15η [12]. This is kept in mind as grid convergence and alternative mesh evaluation techniques are explored to evaluate the accuracy and feasibility of the simulations. The equation for Re was based on the inlet velocity U and diameter *d*,

$$Re = \frac{Ud}{\nu} \tag{2.1}$$

Re_H was the Reynolds number for hydrogen at the first inlet closest to the left wall of the cylinder and computed using the data from Table 2.1,

$$Re_H = \frac{Ud}{\nu_H} = 590. \tag{2.2}$$

Re_{O2} was the Reynolds number for oxygen at the second inlet and was computed using the data from Table 2.1,

$$Re_{O2} = \frac{Ud}{\nu_{O2}} = 571 \tag{2.3}$$

where ν_H and ν_{O2} were the kinematic viscosity of hydrogen.

The velocity was selected to keep Re above 500. The turbulent intensity, *I*, was estimated at

	H	O2
ρ[kg/m^3]	0.0808	1.283
μ[Ns/m^2]	1.37×10^{-5}	3.37×10^{-5}
ν[m^2/s]	1.70×10^{-4}	2.63×10^{-5}
U[m/s]	10	1.5
d[m]	0.01	0.01
I	5%	5%

Table 2.1: Simulation parameters for H and O2 at 300K.

5%. At 5% the turbulent intensity represents a medium flow of simple geometries or low Re [13]. The Kolmogorov length scale η was computed from

$$\eta = (\frac{\nu^3}{\epsilon})^{1/4} \tag{2.4}$$

where the kinematic viscosity ν was,

$$\nu = \frac{\mu}{\rho} \tag{2.5}$$

and the turbulent dissipation rate, ϵ. It was a measure of the rate at which turbulent kinetic energy converts into thermal internal energy due to viscous forces. It represents the rate at which energy of the turbulent eddies was dissipated into heat due to viscosity and was computed from equation,

$$\epsilon = \frac{C_\mu k^{\frac{3}{2}}}{l_o} \tag{2.6}$$

where l_o was the integral length scale and k was the turbulent kinetic energy.

The integral length scale, l_o is a measure of the size of the largest energy containing eddies in turbulent flow. It provides valuable insight into the spatial extent of turbulence and crucial in turbulence modeling and analysis. The integral length scale is commonly related to the boundary layer thickness (δ), but the exact factor can vary depending on the specific flow conditions and empirical observations.

In fully developed pipe flows the integral length scale is approximately 40% of the diameter [14], [15], [16]. For flow around a cylinder the integral length scale would be the 40% of the diameter of the cylinder. The relationship is commonly approximated as

$$l_o \sim 0.4\delta \tag{2.7}$$

In this study, 40% of the cylinder diameter was an approximation of the largest eddies that contained most of the turbulent energy within the flow. The integral length scale for each reactant used in this simulation was,

$$l_{o_H} \sim 0.4\delta_H = 3.91 \times 10^{-4}[m] \tag{2.8}$$

$$l_{o_{O2}} \sim 0.4\delta_{O2} = 3.93 \times 10^{-4}[m] \tag{2.9}$$

Here l_{o_H} and $l_{o_{O2}}$ correspond to the integral length scale for hydrogen and oxygen, respectively.

Turbulent kinetic energy, k, is a measure of the intensity of turbulence within the fluid flow. It was computed using the following equation,

$$k = (\frac{3}{2})(UI)^2 \tag{2.10}$$

where I, U_H, U_{o2} were defined in Table 2.1.

$$k_H = (\frac{3}{2})(0.05U_H)^2 = 0.375[\frac{m^2}{s^2}] \tag{2.11}$$

$$k_{O2} = (\frac{3}{2})(0.05U_{O2})^2 = 0.008[\frac{m^2}{s^2}] \tag{2.12}$$

The boundary layer thickness δ was computed using,

$$\delta \sim \frac{0.37d}{Re^{1/5}} \tag{2.13}$$

where *d* was the diameter of the inlets and the Re was computed from equations 2.2 and 2.3. The boundary layer thickness for hydrogen δ_H and oxygen δ_{O2} were,

$$\delta_H \sim \frac{0.37(d)}{Re_H^{1/5}} = 1.03 \times 10^{-3}[m] \tag{2.14}$$

$$\delta_{O2} \sim \frac{0.37d}{Re_{O2}^{1/5}} = 1.04 \times 10^{-3}[m] \tag{2.15}$$

Using the calculations above and the factor C_μ, the energy dissipation from equation 2.6 was computed. The turbulence model constant, C_μ, was initially derived from experiments and evolved over time. The CFD community agrees on a value of 0.09, as found by Launder and Sharma (1974) [17]. However, other values may be used.

$$\epsilon_H = \frac{0.09 * k_H}{l_{o_H}} = 50.03[\frac{m^2}{s^2}] \tag{2.16}$$

$$\epsilon_{O2} = \frac{0.09 * k_{O2}}{l_{o_{O2}}} = 0.17[\frac{m^2}{s^2}] \tag{2.17}$$

Using the calculations above and equation 2.4 the Kolmogorov length scale computed to be,

$$\eta_H = (\frac{\nu_H}{\epsilon_H})^{1/4} = 5.59 \times 10^{-4}[m] \tag{2.18}$$

$$\eta_{O2} = (\frac{\nu_{O2}}{\epsilon_{O2}})^{1/4} = 5.73 \times 10^{-4}[m] \tag{2.19}$$

A computational mesh with a spatial resolution $\Delta x = 5 \times 10^{-4}$m and cylinder length L=0.09m produced a mesh of approximately 8Gb to 10Gb in size. Over 100Gb of RAM needed to be allocated to manage the mesh, and the time to collect a second of data was about 1-2 weeks. A finer mesh presented issues with mesh qualify, computational stability, and significantly increased computation time and memory allocation [18]. This was at the limit of what was feasible with DNS and mesh generating tools.

To meet the criteria for resolving the Kolmogorov length scale for DNS, it was necessary to consider a coarser mesh. The mesh could be further relaxed by considering an empirical approximation of 70% instead of 40% in equation 2.7. A factor of 70% of the boundary layer thickness can be used for simulations that examine mixing length based turbulent flows in pipes or channels, [19], [20], [21]. The spatial resolution could be relaxed to $\Delta x = 6 \times 10^{-4} m$. However, this adjustment in spatial resolution was not significant enough to alleviate the complexity of the mesh generation or feasibility for DNS. Therefore, alternative turbulence simulations were explored and compared with DNS to address the challenges of resolving the spatial scales with the Kolmogorov length scale.

2.2 CFD software and hardware

The CFD software used for this study was OpenFoam, a widely adopted open source computational fluid dynamic tool chosen for its flexibility, modularity, and powerful set of solvers. OpenFoam supports mesh generation, parallel computing, multi-physics solvers, and customization of solvers. Ennova CFD provided a mesh generation tool compatible with OpenFoam. Mesh generation was performed using Ennova CFD while OpenFoam ran the CFD model. Paraview, an open-source, multiplatform data analysis and visualization application, was utilized for post processing of the

simulation results and visualization.

The HYAK supercomputer at the University of Washington provided free but limited cluster usage. Only a limited amount of memory was provided to run the simulations. Cluster availability was based on a queue system. Running a job for months was unlikely with maintenance, queues, and memory restrictions. It was necessary to develop simulations that could restart after interruptions. This was done by saving more simulation time steps, resulting in greater memory demands.

2.3 Computational Domain

The computational domain was comprised of two inlets for fuel and oxidizer injection, the cylinder walls, and the outlet. Walls of the cylinder were set to zero gradient, no slip boundary conditions, Figure 2.2. The outlet was set to inlet/outlet where the flow was zero gradient unless reversed, then it was fixed value. The fixed value was set to that of the internal field. Both inlets were set to fixed velocities, see Table 2.1.

Lengths of 0.09m, 0.1m, 0.25m, and 0.50m were used. Inlet diameters for both fuel and oxidizer were both set to 0.01m. The fuel was hydrogen, and the oxidizer was oxygen. Both gases were injected radially and transverse to the cylinder axis, see Figure 2.1. A minimum distance of 0.01m was maintained between the center of the hydrogen inlet and the upstream wall. The hydrogen inlet was placed closer to the left wall at a distance of 0.01m away. The oxygen inlet followed at 0.03m from the upstream wall and 0.02m from the center of the hydrogen inlet. Ambient conditions inside the cylinder were kept at room temperature of 293K and air comprising of 77% nitrogen and 23% oxygen.

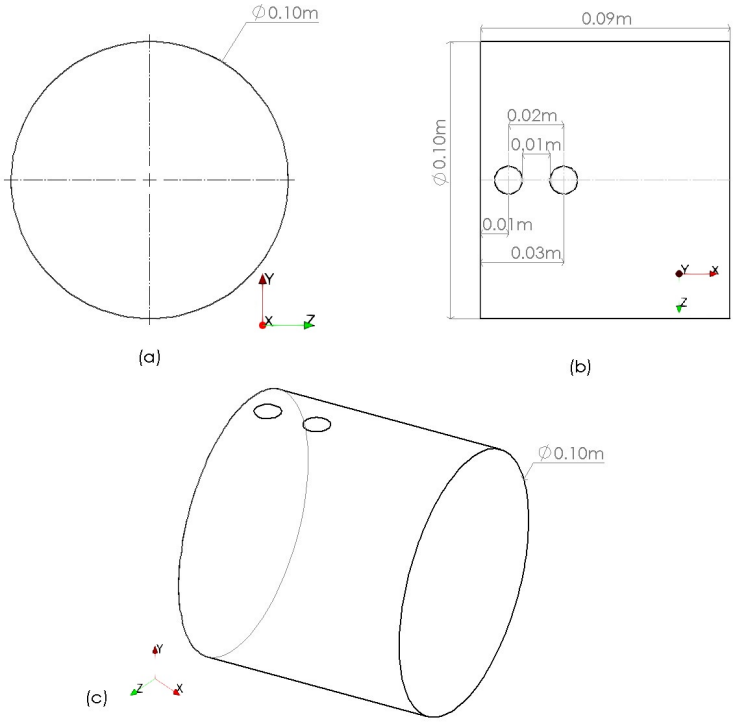

Figure 2.1: Combustion chamber cylinder L=0.09m (a) Side View, (b) Top View, (c) Isometric View

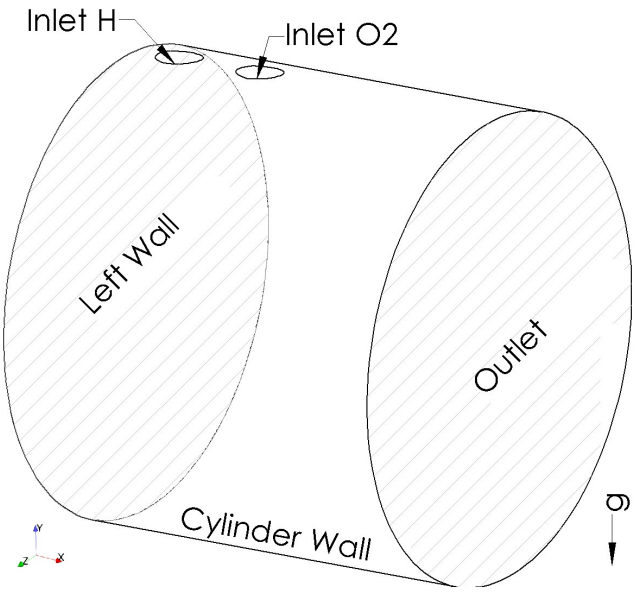

Figure 2.2: Computational domain

2.4 Mesh

DNS required a mesh with a spatial resolution that could resolve the energy spectrum down to the Kolmogorov length scale. However, this requirement was often too strict for the computational resources available. Larger meshes required more RAM to run the simulation and more memory to store the results. HYAK supercomputing cluster was used to run the more computationally expensive simulations. However, even with this resource there were still memory constraints with extremely long computational times.

Building the mesh at the Kolmogorov length scale presented another challenge. As the spatial resolution of the mesh became smaller, issues with skewness, orthogonality, and quality were more prevalent. Time to build the mesh ran weeks, while the simulation time ran for months. These restrictions limited the ability to make design iterations based on simulation results. It was necessary to consider LES in lieu of the limitations from DNS.

Both polyhedral and tetrahedral, see Figure 2.3 and Figure 2.4, meshes were compared. Any improvements in accuracy and speed would lead to a more manageable DNS simulation. The polyhedral resulted in faster simulations with similar accuracy to that of the tetrahedral mesh. At a Re 500 and spatial resolution approximately 5×10^{-4}m, minimum allocations of 150Gb and 10 nodes of HYAK resources were used. A finer mesh, running DNS, with spatial resolution $\eta < 5 \times 10^{-4}$ or $Re >> 500$, was unfeasible with current supercomputing resources.

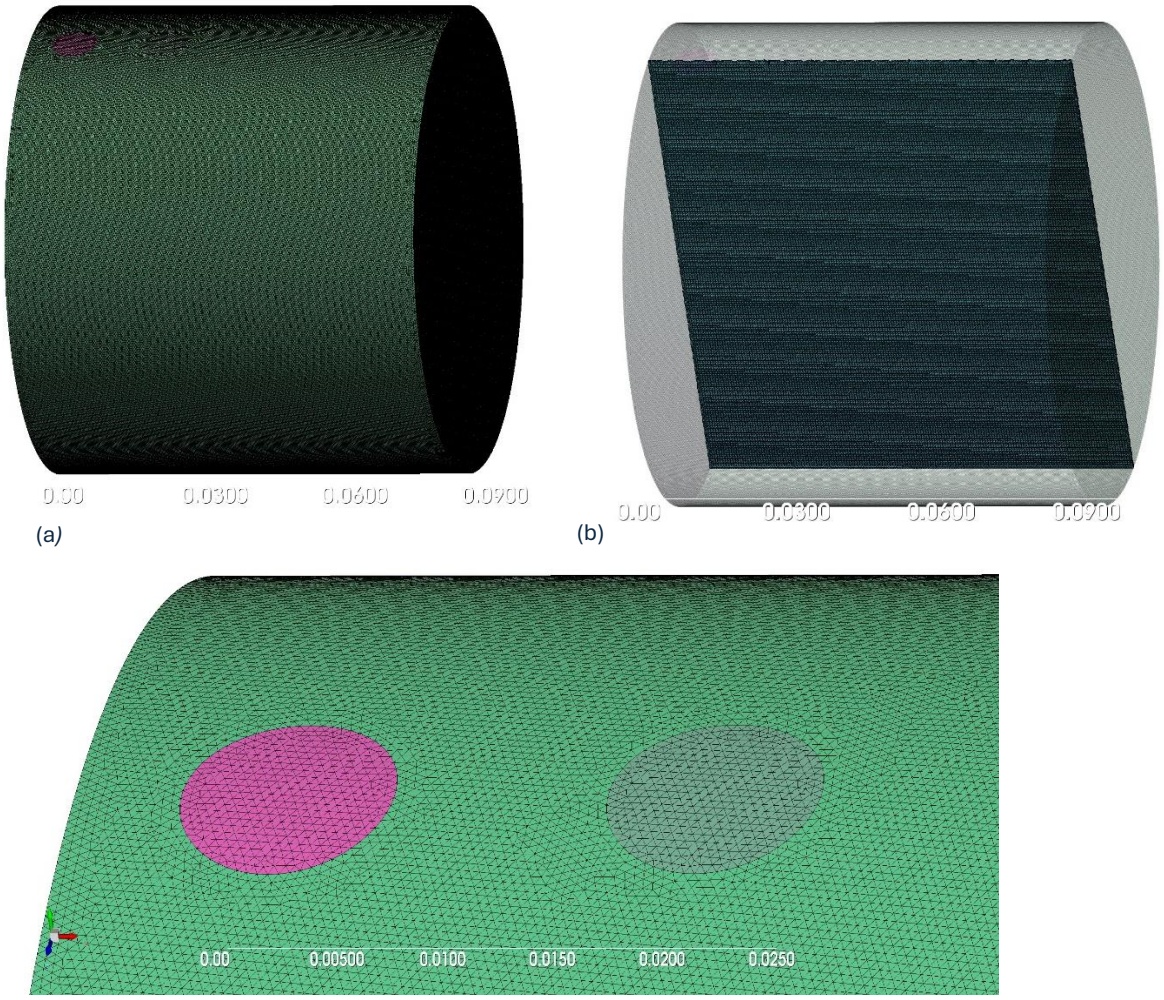

Figure 2.3: (a) Tetrahedral mesh for domain of L=0.09m, inlet diameters at 0.01m, spatial resolution of 5e-4m (b) slice showing internal tetrahedral mesh (c) meshed inlets

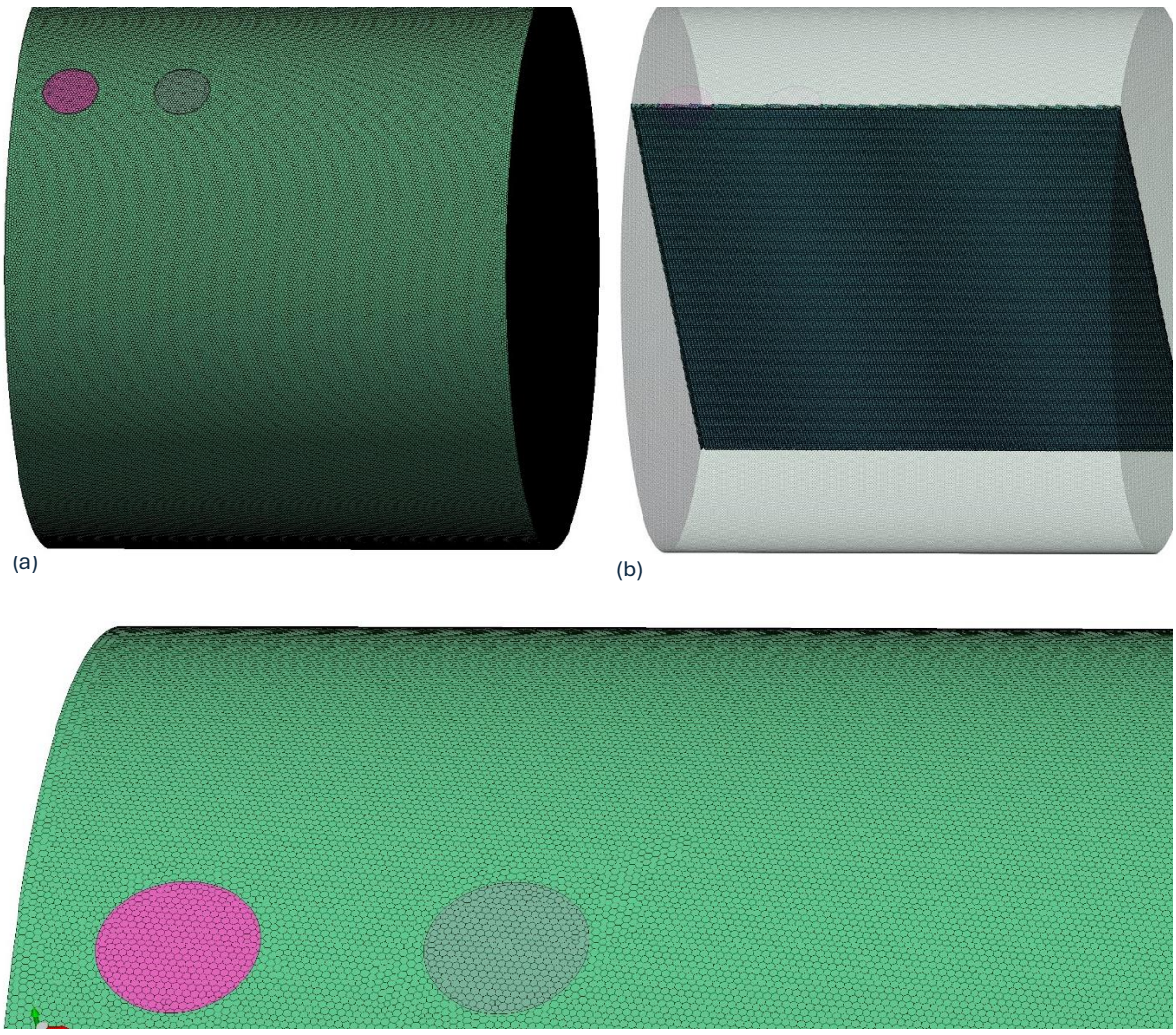

Figure 2.4: (a) Polyhedral mesh for domain of L=0.09m, inlet diameters at 0.01m, spatial resolution of 5e-4m (b) slice showing internal polyhedral mesh (c) meshed inlets

Chapter 3: Simulation

A direct numerical simulation (DNS) is a high-fidelity computational technique used to solve the Navier-Stokes equations without any turbulence model. Consequently, DNS must resolve all spatial and temporal scales for turbulence, from the smallest Kolmogorov scales (dissipative scale) to the largest energy scales. Unlike other models that approximate turbulence, DNS directly solves the governing equations. It is the simplest approach, and most accurate [14]. However, the computational cost of DNS is extremely high, and the requirements increase with the Reynolds number [22].

The spatial scales must be resolved with a fine mesh to capture the smallest dissipative scale at the Kolmogorov microscale, up to the integral length scale, l_o, associated with kinetic motion. This often requires a mesh of millions, or even billions, of grid points. By comparison, a Large Eddy Simulation (LES) can use a coarser grid. However, further studies are needed to evaluate the accuracy of resolving the energy scales.

3.1 Combustion Model

The simulations were set up with a combustion model to replicate realistic conditions. However, to focus on the mixing behavior of inert reactants, the combustion modeling was deliberately turned off. This approach allowed for a clear observation of the mixing dynamics without the complexities introduced by combustion reactions.

With the combustion turned off, the transport equations for species and other scalar fields remained active. This ensured the simulation still accounted for essential transport phenomena, including the advection, diffusion, and dispersion of species within the flow. Turning off combustion excluded the chemical reactions and their associated calculations related to source terms from the governing equations. These excluded terms include heat release, thermal expansion, turbulence-chemistry interactions, and species consumption or production. By excluding these source terms, the simulation focused solely on the transport and mixing of inert species. This approach allowed for a detailed analysis of non-reactive processes while avoiding the added complexities of combustion chemistry. Consequently, the results provided insights into the behavior of the flow and the mixing dynamics of species without any interference from chemical reactions or heat-related effects.

The combustion model employed in this study is centered on the fundamental elementary reaction for hydrogen and oxygen combustion, involving the hydrogen atom and oxygen molecule [23]. This reaction serves as the main chain-branching reaction for oxidation of hydrogen and hydrocarbon-based fuels.

$$\mathrm{H} + \mathrm{O2} \longrightarrow \mathrm{O} + \mathrm{OH} \tag{3.1}$$

This reaction is part of a broader series of combustion reactions, making it ideal for studying new combustion chamber configurations [24], [25], [26], [27], [28], [29], [30], [31], [32]. The optimized mechanisms of the GRI-mech version 3.0 contained the reversible Arrhenius reaction for hydrogen and oxygen. In OpenFOAM, GRI-mech 3.0 and associated rate and thermodynamic data were used in the modeling of the chemistry [33].

The Sutherland transport model [34], [35] computed dynamic viscosity μ, thermal conductivity κ and thermal diffusivity α. The model is known for its accuracy in predicting transport properties in gases over a range of temperatures. It accounts for temperature dependency and pro-

vides a reliable method for calculating these properties. The simplicity and empirical basis of the Sutherland model made it an excellent choice for combustion modeling, as it ensures precise transport property predictions across varying conditions. In addition, its integration with CFD code, such as OpenFOAM, facilitates seamless and accurate simulations.

The JANAF (Joint Army Navy Air Force) thermochemical tables were used to compute the specific heat c_p. These tables provided a reliable and comprehensive thermodynamic data for a wide variety of compounds, including gases, liquids, and solids [36]. The tables contained important information such as enthalpy, entropy, Gibbs free energy, and specific heat capacities over a range of temperatures. This data was essential for precise thermodynamic calculations, particularly in combustion simulations, where accurate thermodynamic properties were crucial for predicting reaction rates, heat transfer, and overall system behavior. Using the JANAF tables ensured that the thermodynamic properties of the combustion reaction were accurately represented [36].

The simulation employs a compressible solver using the PIMPLE algorithm. PIMPLE is an adaptive method capable of handling both incompressible and compressible flows. The parameters displayed in the box represent key configurations specific to OpenFoam. In this simulation, the physical and thermodynamic properties of the modeled gases were set to hePsiThermo, perfectGas, sensibleEnthalpy, and Sutherland, see Appendix A. The hePsiThermo is the thermophysical model designed for compressible flows and incorporates calculations for density, temperature, and enthalpy. The perfectGas equation of state explicitly accounts for density variations due to pressure and temperature, which are critical for solving compressible flows. The Sutherland transport model is used for compressible gases, as it accounts for temperature-dependent viscosity. The sensibleEnthalpy model solves energy equations for both temperature and energy, further confirming the compressible nature of the simulation.

The Arrhenius equation models the temperature dependence of the chemical reaction; see Appendix B. It was necessary to adjust the Arrhenius coefficients to account for stiffness in chemistry, where high reaction rates lead to numerical instability. Stiffness in chemistry occurs when some

reactions are faster than others. The disparity in timescales creates numerical instability.

Tuning the Arrhenius coefficients was necessary to optimize the reaction rates and manage the stiffness in chemical kinematics. This adjustment helped align the timescales of different reactions, ensuring that the fastest chemical timescales are those that controlled the simulation time step [37]. Tuning the coefficients was essential because the solvers would simply not run or encounter instability issues. Once the reaction rates were appropriately adjusted, selecting the appropriate numerical schemes for stiff ODE's was the next step in ensuring numerical accuracy and stability.

The seulex ODE implicit solver was chosen for its particularly effective handling of stiff problems. The seulex ODE implicit solver solved the solution by considering both the current and next timestep. In the context of numerical simulations that use ODE's, stiffness refers to situations where there are rapidly changing components in the solution. This required very small timesteps to maintain stability and accuracy [38]. In contrast, for explicit methods, the value of the solution is calculated directly using only the known values from previous timesteps. This can lead to instability when dealing with stiff problems [39].

The absolute tolerance for the seulex ODE solver was set at 1×10^{-8} and relative tolerance at 0.1. This defined the acceptable absolute error for the solution. The absolute and relative tolerance were tuned to maintain the stability of the simulations and the accuracy of the solution. To maintain accuracy, the simulation required small adjustable timesteps and a Courant Friedrich Lewy, CFL, number set to 0.5. The CFL is a dimensionless quantity, that ensures the simulations's timestep is appropriate for the spatial grid size and Re. A CFL<1 maintains a stable and accurate simulation.

First-order implicit Euler bounded transient solver was used to determine the time discretization scheme. This method was chosen for its stability and ease of implementation, particularly in transient simulations. The implicit nature of the Euler method was effective in handling stiff problems, as it allows for larger time steps without compromising the numerical stability of the solution. This made it particularly suitable for simulations where rapid changes occur over time [40]. For this study, there were rapidly changing reactants over short time intervals and the problem was

stiff.

An implicit solver iterates to find the next time step that satisfies the equation and maintains stability. This iterative process ensures that the solution remains stable even in the presence of stiffness. In this study, stiffness played a major role in the stability of the simulation. By using the first-order implicit Euler method, the simulations were able to maintain stability and accuracy while dealing with highly dynamic and transient phenomena.

The Gauss linear-discretization scheme was used to compute the gradients, interpolations, and integrals in the simulation. This scheme relies on the Gaussian integration, which involves summing values on cell faces that are interpolated from cell centers. The Gauss linear scheme known for its second-order accuracy, made it a suitable choice for combustion modeling using CFD [41].

The divergence schemes were second order accurate, enhancing the overall precision of the numerical solutions. These schemes are crucial for minimizing numerical diffusion and improving the fidelity of the simulation results. To ensure numerical accuracy and stability, modifications were made to the divergence scheme to prevent overshoots and undershoots in the computations. This study used the limitedLinearV 1 and limitedLinear 1 schemes; see Appendix C. A modification of 1 for the bending factor, ensures second-order accuracy while applying limiting. Both schemes combined the accuracy of the linear scheme with the stability of the upwind scheme. The limiters, or bounded schemes, constrain the interpolated values within physical limits. By doing so, the scheme maintain the integrity of the solution and avoid numerical artifacts that could compromise the results [42].

The combination of the Gaussian linear discretization and the applied modifications to the divergence schemes ensured that the gradients computed at each iterative step in the simulation were second order accurate and stable. This helped to minimize numerical diffusion and improve the precision of the numerical solutions, leading to more reliable and valid simulation results [43], [44].

Turbulence modeling was turned off to allow for DNS. DNS resolves all the scales of turbulence directly, providing detailed insights into the flow dynamics without relying on a turbulence model. Alternatively, for LES only the large scale eddies were modeled directly, while turbulence modeling is applied to the smaller subscales using a subgrid-scale (SGS) model [45].

Achieving a stable and accurate combustion simulation required the careful integration of physically grounded models and robust numerical solvers. The Sutherland transport model and JANAF thermochemical tables ensured realistic temperature dependent material properties, while the compressible hePsiThermo model and the perfectGas equation of state captured critical flow behaviors. Managing chemical stiffness through adjustments with the Arrhenius coefficients and ODE stiffness through the seulex implicit ODE solver was essential to prevent numerical instability caused by rapid reaction kinetics. Additionally, the use of bounded second order accurate discretization schemes and implicit time integration safeguards against spurious oscillations and divergence. DNS further demanded high fidelity in both spatial and temporal resolution. Without this rigorous attention to detail, both in physical modeling and numerical strategy, the simulation would have been unstable, inaccurate, or completely non-viable.

3.2 Simulation

A Gauss linear-discretization scheme computed the gradients, with modifications to avoid over or undershoots in the computations. The divergence schemes were second order accurate. Both schemes allowed for better stability and accuracy. Turbulence modeling was turned off to for DNS. A grid of $\eta = 5 \times 10^{-4} m$, hydrogen $Re_H = 590$ and oxygen $Re_{O2} = 571$, equations 2.2 and 2.3 respectively, were used for DNS.

A simulation on a polyhedral mesh with spatial resolution $5 \times 10^{-4} m$, inlet diameters of 0.01m, and a characteristic length of 0.09m was studied. Inlet velocities were 10m/s for H and 1.5m/s for O2, see 2.1. At t=1.3s, the concentrations for H and O2 were presented in Figure 3.1 along with

	H	O2
$\rho[\mathrm{kg/m^3}]$	0.0808	1.283
$\mu[\mathrm{Ns/m^2}]$	1.37×10^{-5}	3.37×10^{-5}
$\nu[\mathrm{m^2/s}]$	1.70×10^{-4}	2.63×10^{-5}
U[m/s]	10	1.5
d[m]	0.01	0.01
I	5%	5%
Re	590	571
η	5.51×10^{-4}	5.65×10^{-4}

Table 3.1: Simulation parameters for H and O2 at 300K.

respective concentrations across the entire cylinder.

This grid posed significant challenges due to a substantial demand for large RAM, extensive memory storage, and lengthy computational time. Additionally, limitations on supercomputing memory and cluster usage allocations made continued use of this grid unfeasible. As a result, only a little over 1ms of data was collected in approximately 3 months. The increased time to collect any appreciable amount of data greatly limited the ability to iterate the combustion chamber design.

Generating results using DNS to directly compute the turbulence was too memory and time intensive. Relaxing the grid as discussed in Chapter 2, was taken into consideration to reduce both memory consumption and simulation time. A coarse mesh would not be able to resolve the turbulent kinetic energies down to the Kolmogorov length scale, a requirement for DNS. It was then necessary to evaluate an alternative to DNS, such as LES. Large Eddy Simulation (LES), unlike DNS, simulates the turbulent flow by resolving the larger eddies explicitly and modeling the smaller, subgrid-scale eddies. LES was based on the idea that large turbulent eddies, which are dependent on the geometry of the problem, contained most of the energy of the turbulent flow. These large eddies were resolved directly in the simulation, while the smaller, more universal subgrid-scale eddies were modeled using subgrid-scale (SGS) models [46], [47].

There were several methods to assess the quality of the LES grid [48], [49]. The Pope criterion was a widely used method to evaluate the quality of the LES mesh by assessing the fraction of

turbulent kinetic energy (TKE) that was resolved by the simulation.

In comparison a mesh at $\Delta x = 1 \times 10^{-3} m$ that ran LES, see Figure 3.2, shows similar results to that of a DNS mesh $\Delta x = 5 \times 10^{-4} m$, Figure 3.1. This mesh was much faster to run with results in weeks rather than months. The resolution of the finer mesh running DNS, Figures 3.1 (a) and (b), had finer developing structure than the coarser LES mesh, Figure 3.2 (a) and (b). However, the evolution of the larger vortices and the concentration profile of each fluid were similar enough to provide information on the overall mixing behavior.

3.3 Pope Criterion for LES mesh evaluation

The one-equation Large Eddy Simulation subgrid scale model used for this study solved the sub-grid scale turbulent energy using a single transport equation. This simplified approach effectively represented the unresolved small-scale turbulent motions within the computational domain. The model provided a measure of the fraction of turbulent kinetic energy contained in the resolved motions, which were determined by the grid size. By relying on this single transport equation, the model efficiently captured the energy dynamics of smaller scales without requiring a more complex multi-equation approach.

The quality of the LES simulation was assessed with the Pope criterion [50]. This criterion helped to determine the fraction of the turbulent kinetic energy that was resolved by the simulation. The Pope criterion was useful in evaluating the accuracy and reliability of the LES model. The criterion was defined as,

$$M(\mathbf{x}, t) = \frac{k_{SGS}(\mathbf{x}, t)}{k_{SGS}(\mathbf{x}, t) + k_{RES}(\mathbf{x}, t)} \tag{3.2}$$

where k_{RES} was the kinetic energy of the resolved eddies, determined by the grid size.

$$k_{RES} = 0.5(u'^2 + v'^2 + w'^2) \tag{3.3}$$

and the velocity velocity fluctuations u'^2, v'^2, w'^2

$$u'^2 = u + \overline{U} \tag{3.4}$$

$$v'^2 = v + \overline{V} \tag{3.5}$$

$$w'^2 = w + \overline{W} \tag{3.6}$$

The mean velocities were $\overline{U}, \overline{V}, \overline{W}$ and k_{SGS} was the TKE. The kinetic energy of the resolved eddies, k_{RES}, was computed during post processing of the simulation. The one-equation LES sub-grid scale model was unique in its capability to compute k_{SGS} for each timestep.

The Pope criterion was a global field computed along the entire domain. It was visualized by plotting it in cross sections of the domain. In Figure 3.3 the value of M indicates the quality of the mesh. A value of M=0 corresponds to a DNS simulation, while a value of M=1 corresponds to a RANS simulation. Values of M between 0.6 and 0.8 are indicative of a high-quality LES mesh.

Using the Pope criterion, a mesh with spatial resolution $\Delta x = 1 \times 10^{-3} m$ at 1.3s timestep was able to resolve the energy scales well enough for LES. While other areas were between M=0.4 to 0.9, the greater part of the mesh and downstream of the inlets had M~ 0.

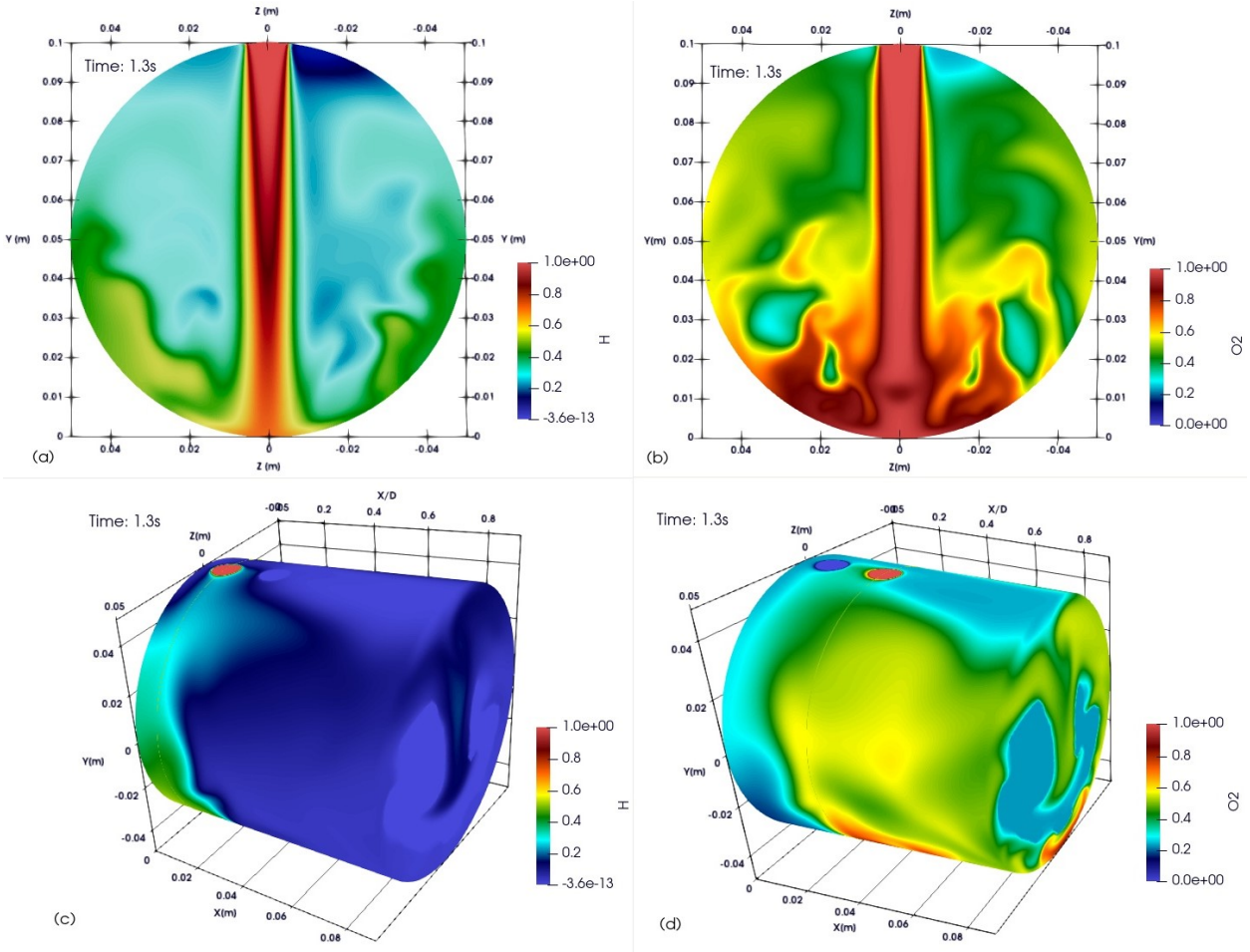

Figure 3.1: DNS at 1.3s and spectral resolution $5 \times 10^{-4} m$ (a) Cross section of H concentration at the center of H inlet x=0.01m, (b) Cross section of O2 concentration at the center of O2 inlet x=0.03m, (c) H concentration across the length of cylinder, (d) O2 concentration across the length of cylinder. Line at (c) along x=0.01m and (d) along x=0.03m represents the cross section viewed in (a) and (b).

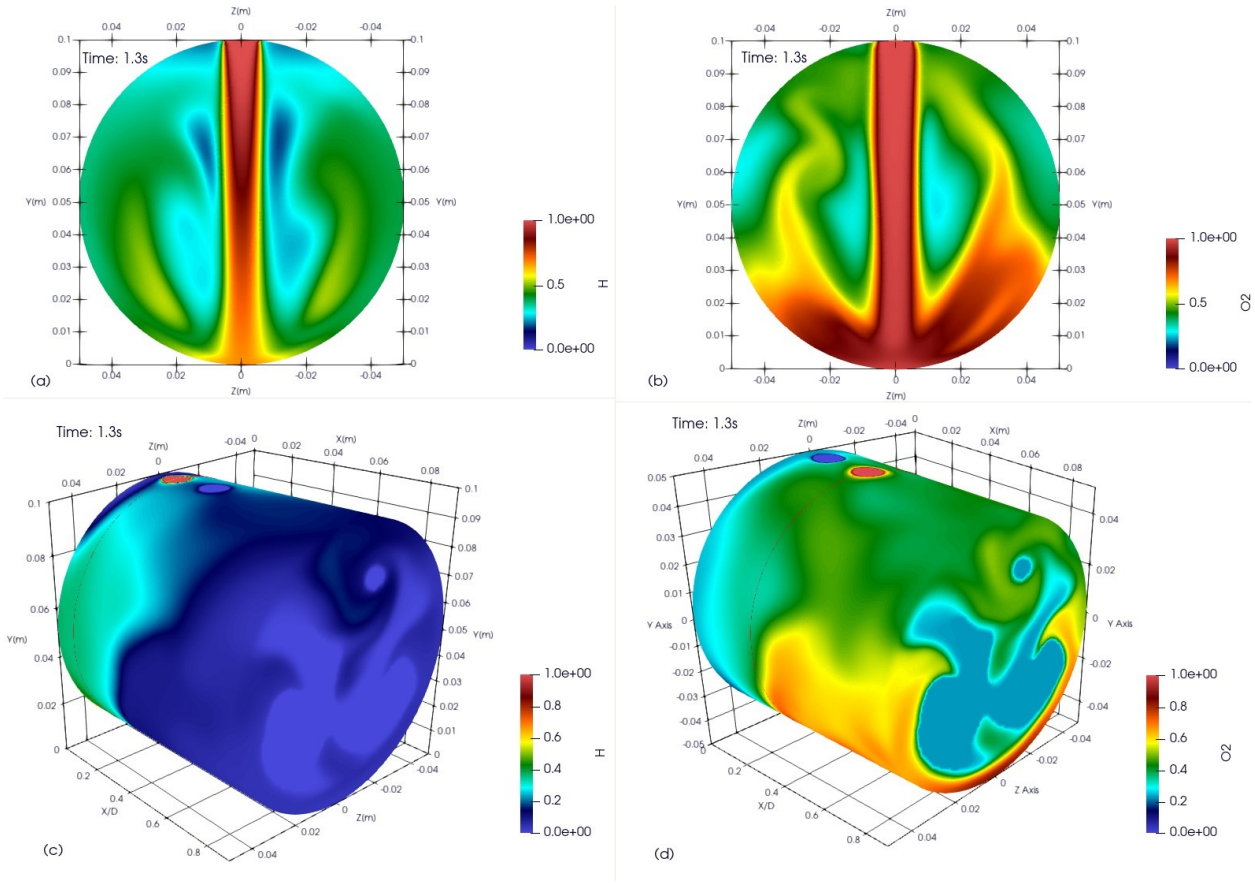

Figure 3.2: LES at 1.3s and spectral resolution $1 \times 10^{-3}m$ (a) Cross section of H concentration at center of H inlet x=0.01m, (b) Cross section of O2 concentration at center of O2 inlet x=0.03m, (c) H concentration across length of cylinder, (d) O2 concentration across length of cylinder. Line at (c) along x=0.01m and (d) along x=0.03m represents the cross section viewed in (a) and (b).

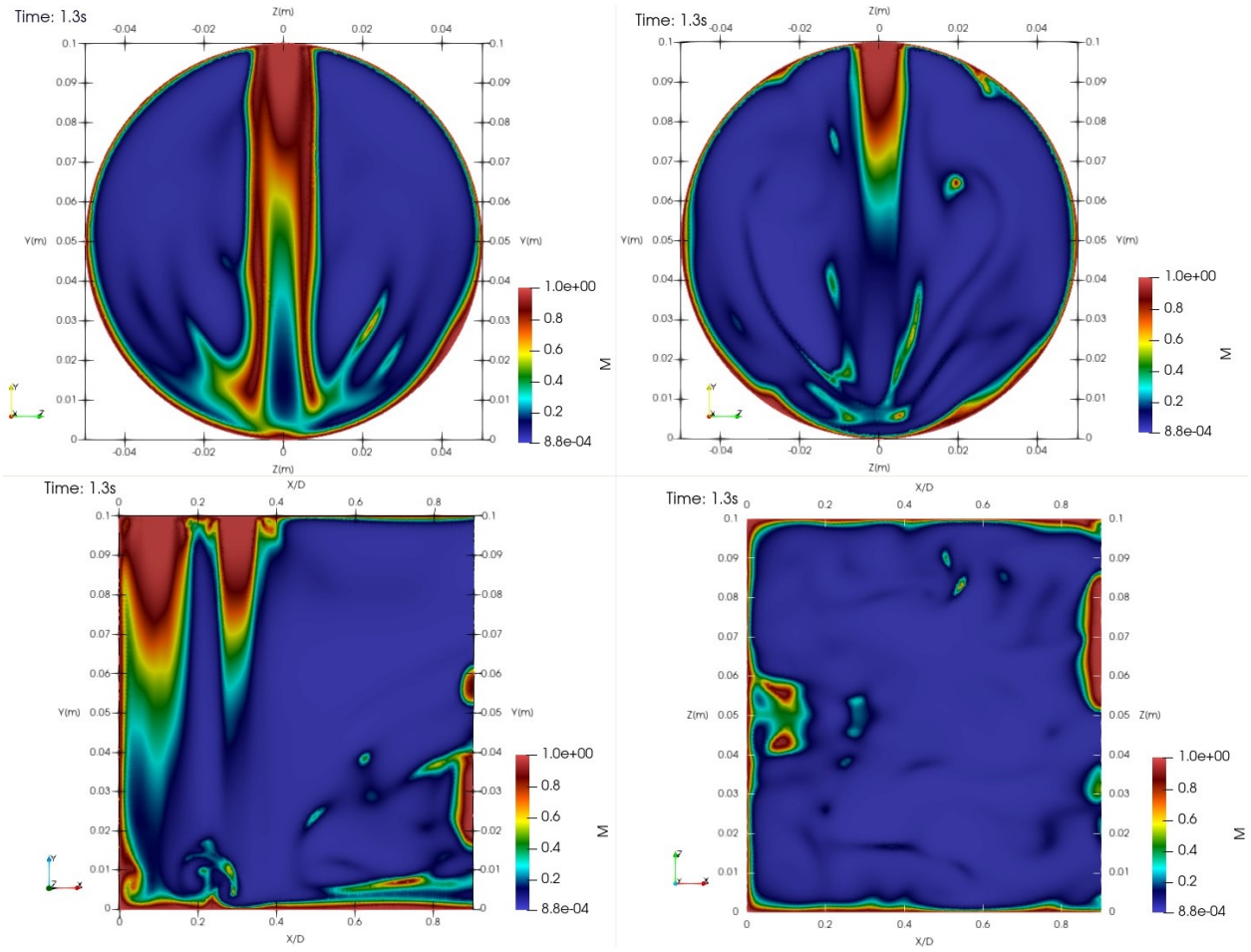

Figure 3.3: LES Pope criterion at 1.3s $\Delta x = 1 \times 10^{-3} m$ (a) Cross section of H concentration at center of H inlet x=0.01m, (b) Cross section of O2 concentration at center of O2 inlet x=0.03m, (c) Cross sectional slice along y axis (d) Cross sectional domain along z axis

Chapter 4: Concentration and Stability

The concentration profiles were examined to analyze the formation of counterrotating flows generated by the transverse jet inert species transport across the combustion chamber. To isolate the transport of inert gases, combustion was turned off, ensuring that no additional variables from combustion influenced the results. Various approaches were explored to thoroughly analyze the concentration profiles along the characteristic length of the combustion chamber.

In this analysis, Surface Line Integral Convolution (LIC) and streamlines were both employed to visualize vector fields, each providing unique insights into the evolution of the flow. LIC applies a convolution process along the direction of the vector field, producing a textured appearance that highlights flow patterns on surfaces. This method provides a smooth and continuous representation of flow over complex surfaces, making it easier to detect subtle flow features. It is particularly effective for visualizing flow on curved or intricate surfaces, such as the flow over a car body or an aircraft wing.

Streamlines, on the other hand, are lines that are tangent to the velocity field at every point, illustrating the path a particle would follow within the flow. They offer a clear and direct visualization of flow paths, enabling the tracing of specific flow directions and patterns. Streamlines are often used to visualize flow in simpler geometries or to emphasize particular flow trajectories within the flow field.

The LIC method provides a more continuous and integrated view of flow patterns across the surfaces of the two-dimensional (2D) cross sections, while the streamlines distinctly depict dis-

tinct flow paths. LIC is better at revealing finer details and subtle variations in the flow, whereas streamlines are advantageous for tracing specific flow paths. Both techniques proved essential in analyzing the flow and concentrations across the combustion chamber and in its different cross sections.

In Figure 4.1, the counterrotating flow is visualized using the LIC profile. An overlay of each reactant and the mean velocity is added to indicate where each constituent species is most concentrated. At 5s and in the 0.7D cross section, nitrogen is completely pushed out of the cavity, leaving oxygen as the predominant species. The absence of nitrogen indicates that any remaining ambient oxygen, which is part of the primary fluid, is also purged from the chamber. Here, it is assumed that the ambient oxygen purges at the same rate as the ambient nitrogen. Higher concentrations of hydrogen are found closer to the center of larger vortex cores; see Figure 4.1(c).

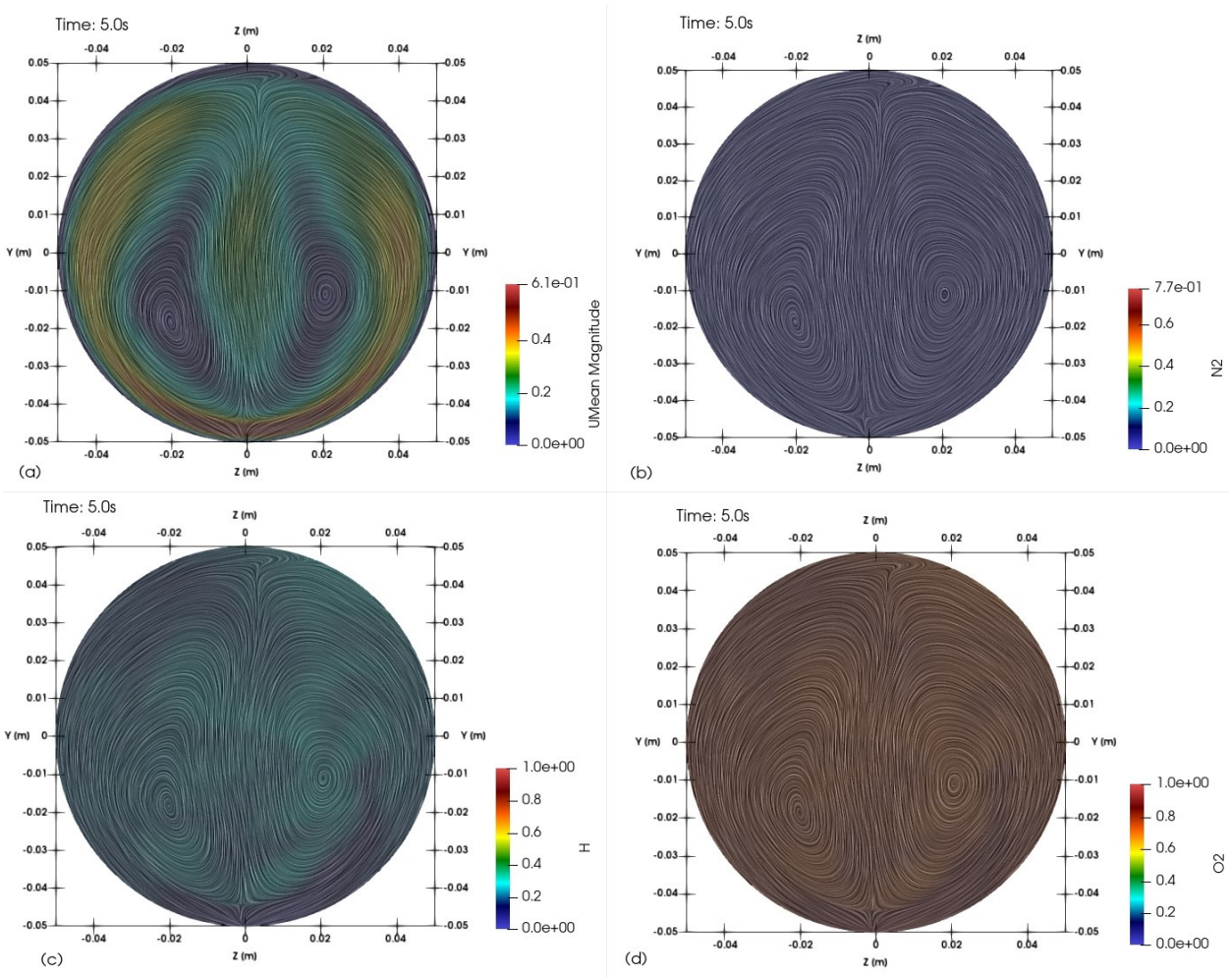

Figure 4.1: Cross sections at 5s into the simulation downstream at 0.7D. The LIC profile plotted over (a) mean velocity (b) nitrogen concentration (c) hydrogen concentration (d) oxygen concentration

At 0.7D and 5s into the simulation, it is evident that the concentrations of oxygen and hydrogen are nearly uniform. To visualize the evolution of the concentrations, the LIC downstream of the inlets was plotted in Figure 4.2, 4.3, 4.4 and 4.5.

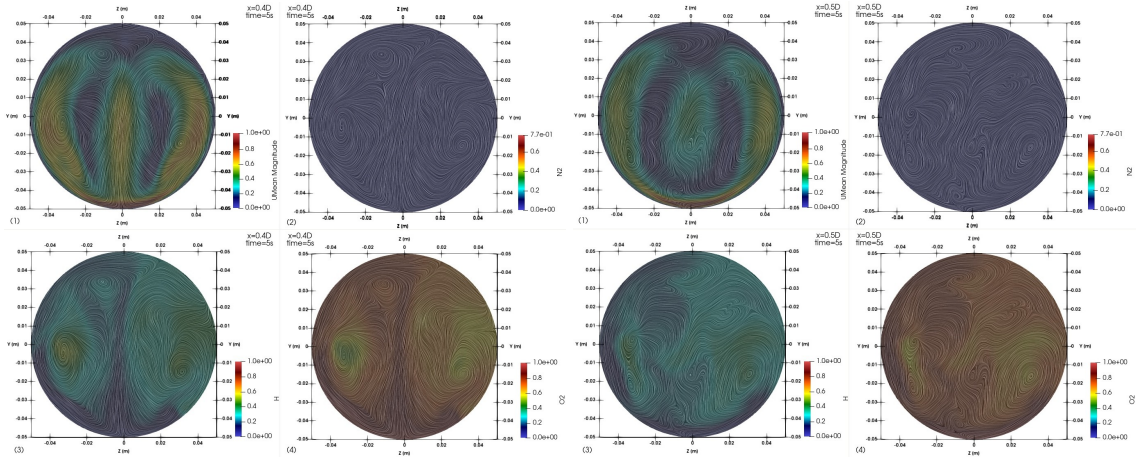

(a) x=0.4D **(b)** x=0.5D

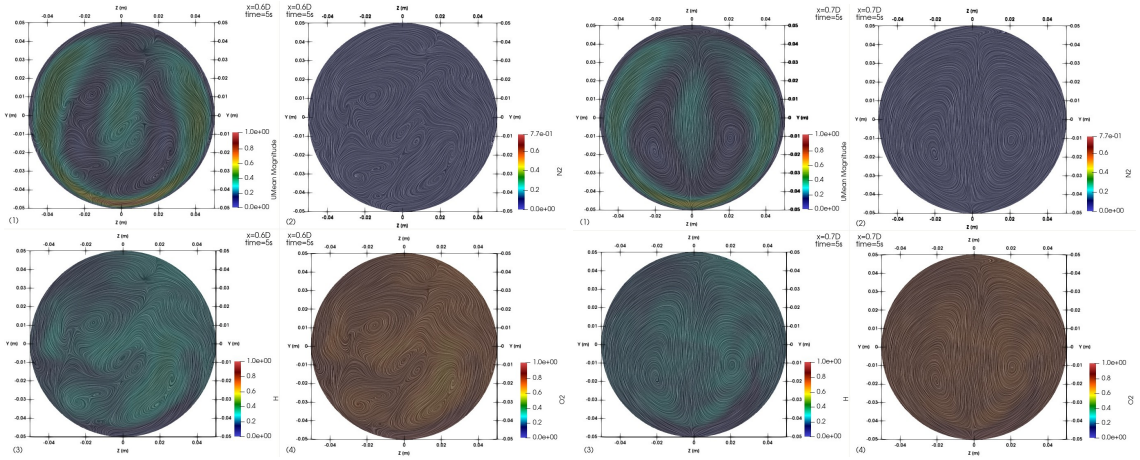

(c) x=0.6D **(d)** x=0.7D

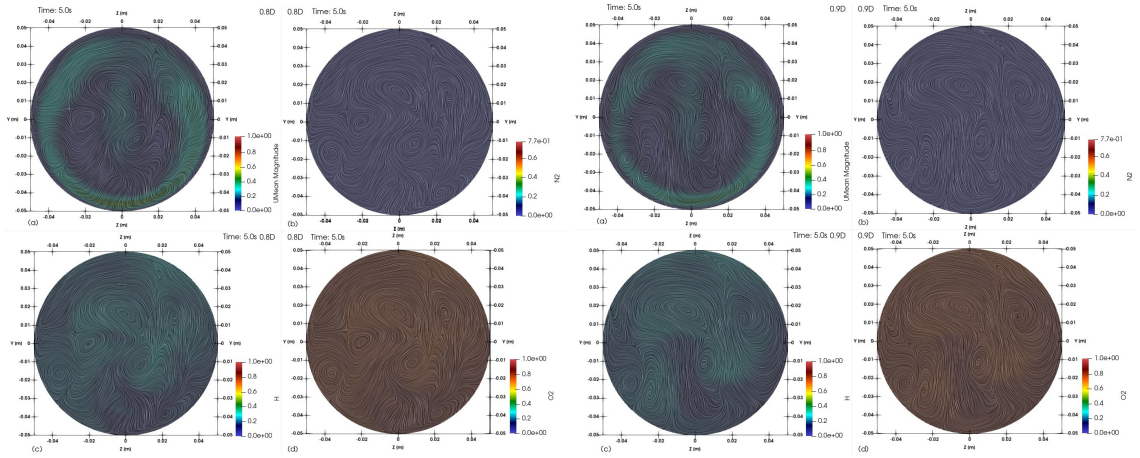

(e) x=0.8D **(f)** x=0.9D

Figure 4.2: LIC plots of consecutive cross sections downstream of inlets from x=0.4D to x=0.9D, with subplots displaying: (a) velocity profile and (b) nitrogen concentrations, (c) hydrogen and (d) oxygen concentrations

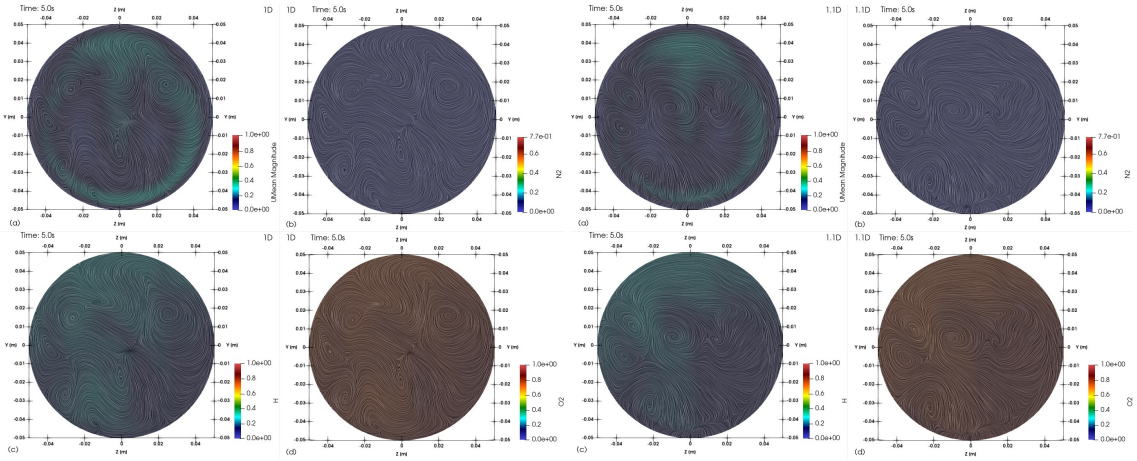

(a) x=1D

(b) x=1.1D

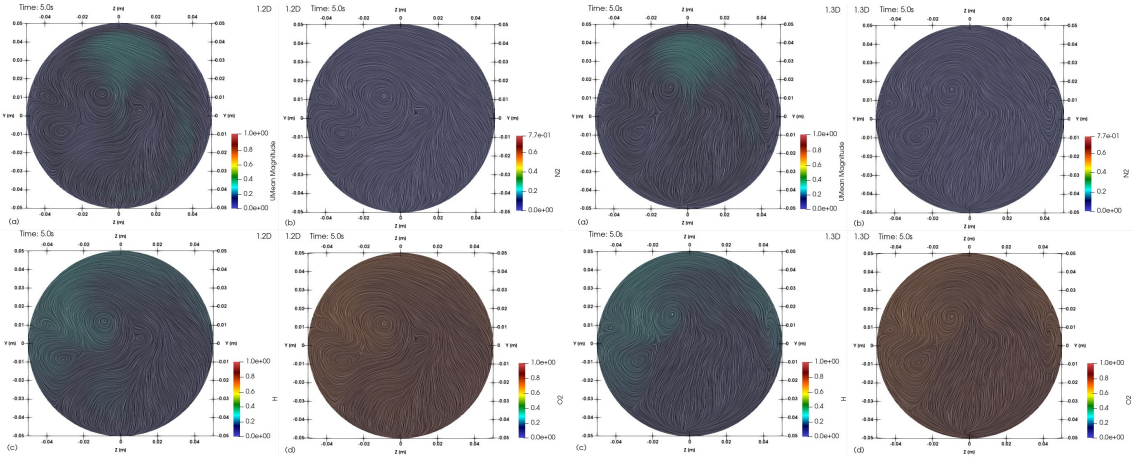

(c) x=1.2D

(d) x=1.3D

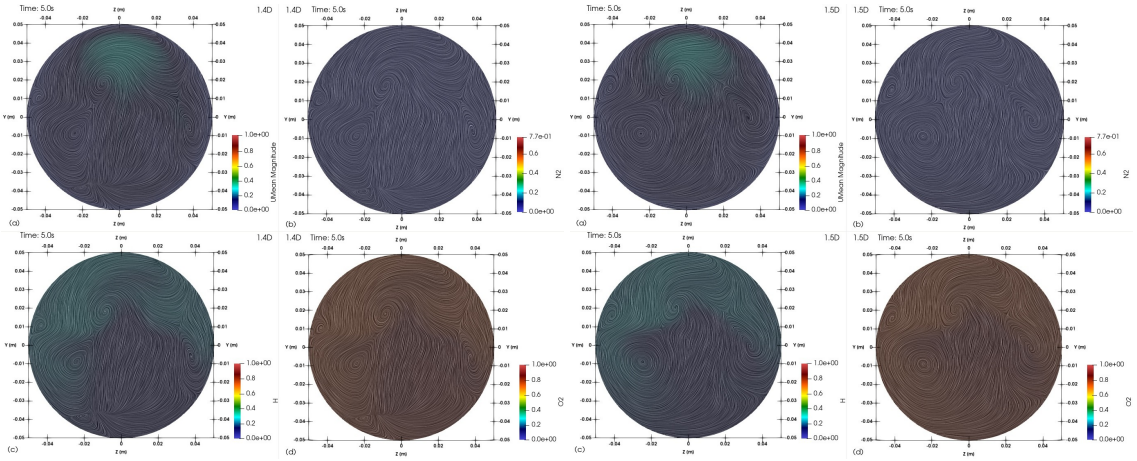

(e) x=1.4D

(f) x=1.5D

Figure 4.3: LIC plots of consecutive cross sections downstream of inlets from x=1D to x=1.5D, with subplots displaying: (a) velocity profile and (b) nitrogen concentrations, (c) hydrogen and (d) oxygen concentrations

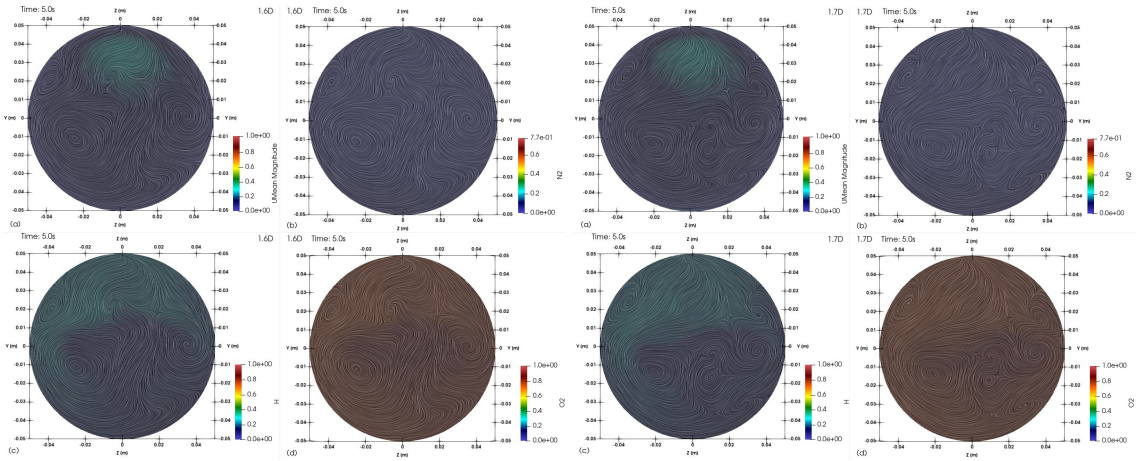

(a) x=1.6D **(b)** x=1.7D

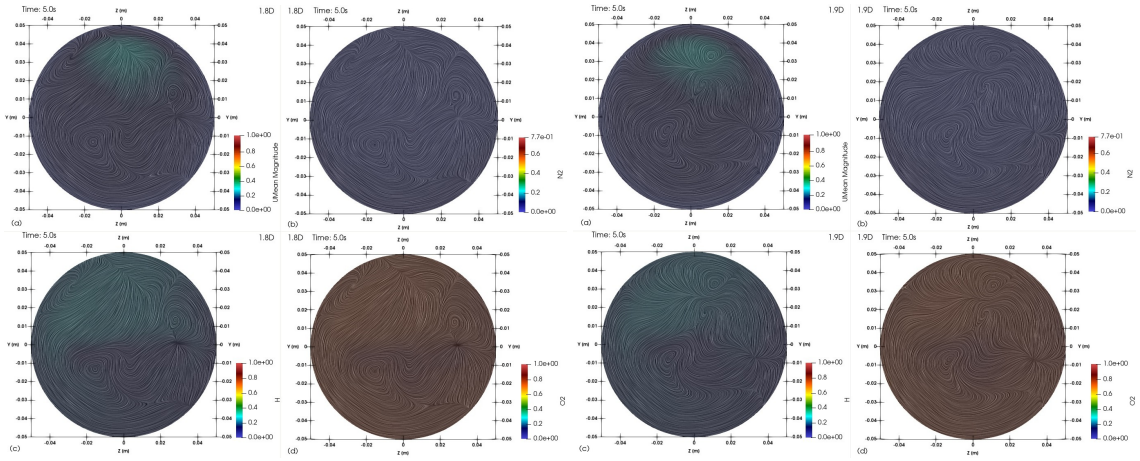

(c) x=1.8D **(d)** x=1.9D

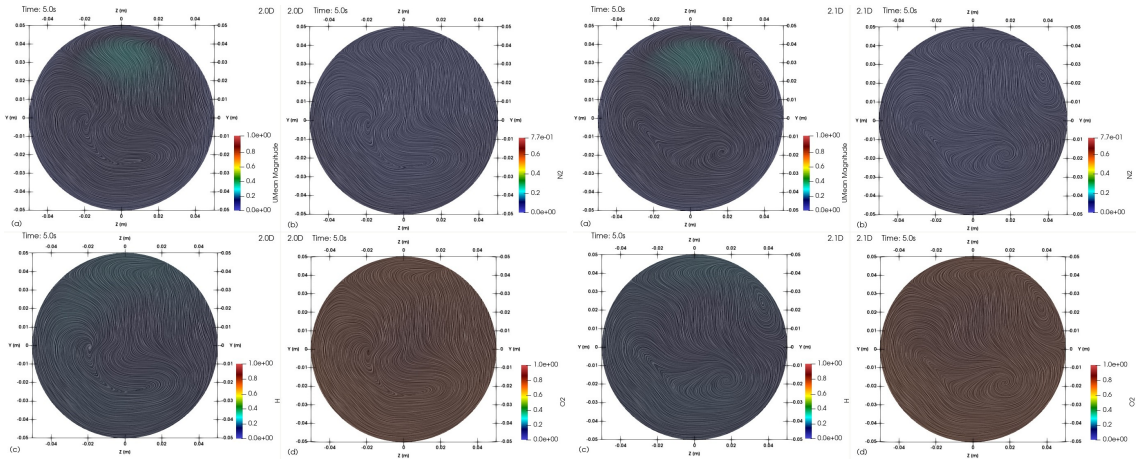

(e) x=2D **(f)** x=2.1D

Figure 4.4: LIC plots of consecutive cross sections downstream of inlets from x=1.6D to x=2.1D, with subplots displaying: (a) velocity profile and (b) nitrogen concentrations, (c) hydrogen and (d) oxygen concentrations

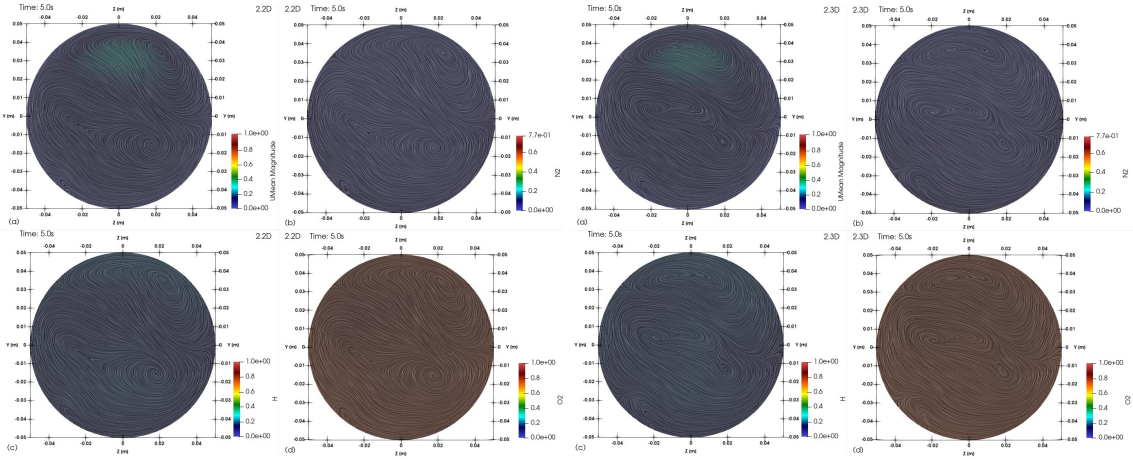

(a) x=2.2D **(b)** x=2.3D

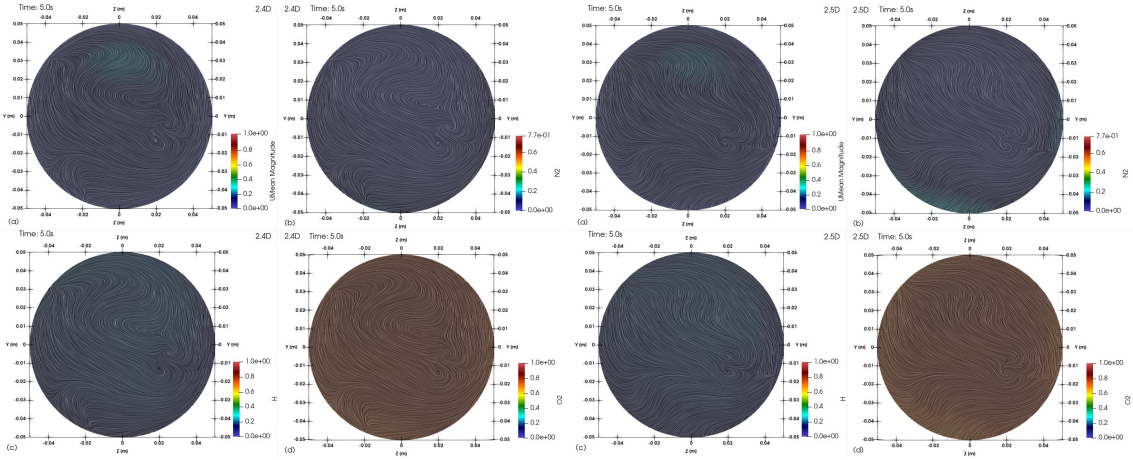

(c) x=2.4D **(d)** x=2.5D

Figure 4.5: LIC plots of consecutive cross sections downstream of inlets from x=2.2D to x=2.5D, with subplots displaying: (a) velocity profile and (b) nitrogen concentrations, (c) hydrogen and (d) oxygen concentrations

The streamline plots of Figures 4.6 and 4.7 show counterrotating flows in three-dimensional (3D). The counterrotation follows a 3D trajectory. When taking a cross section, the full flow profile is constrained to 2D and represents only a portion of the complete flow trajectory. Streamlines would weave in and out of a cross section, making it difficult to discern the counterrotation. Therefore, a projection or an LIC plot was necessary to capture the counterrotating flow and the formation of the largest eddy.

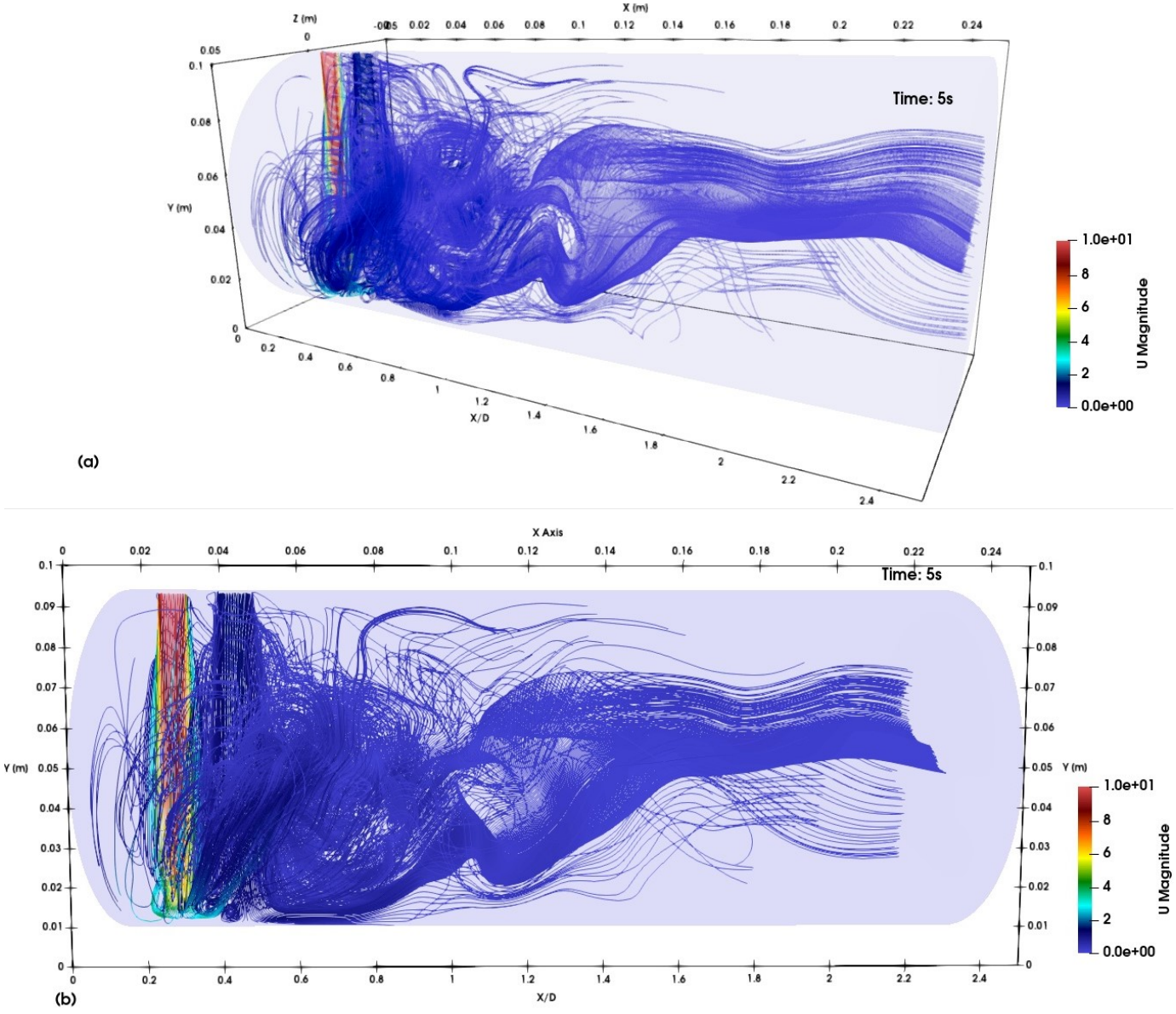

Figure 4.6: Velocity streamline plot at 5s into the simulation (a) isometric view (b) front view

In Figures 4.7 (a) and (c), the front view of the flow streamlines is overlaid with the oxygen and hydrogen concentration profiles. As the streamlines are in 3D, the front view represents a projection of the 3D profile onto a 2D view. The counterrotating flow is clearly visible in this projection. The overlaid oxygen and hydrogen mass fraction concentration distribution highlights regions of mixing, indicated by varying color gradients within the larger vortex core.

In Figure 4.7 (a) at 5s into the simulation, concentrations were represented by green, yellow, blue, and ranged from 20% to 50% non-reactant species concentrations that appeared within the vortex core. A similar pattern is seen in the hydrogen overlaid streamline profile. These regions of varying concentrations indicate areas where both hydrogen and oxygen coexist and mix. The highest degree of color contrast occurs at the center of the largest vortex core between 0.04m and 0.05m along the yaxis, slightly below the center of the chamber.

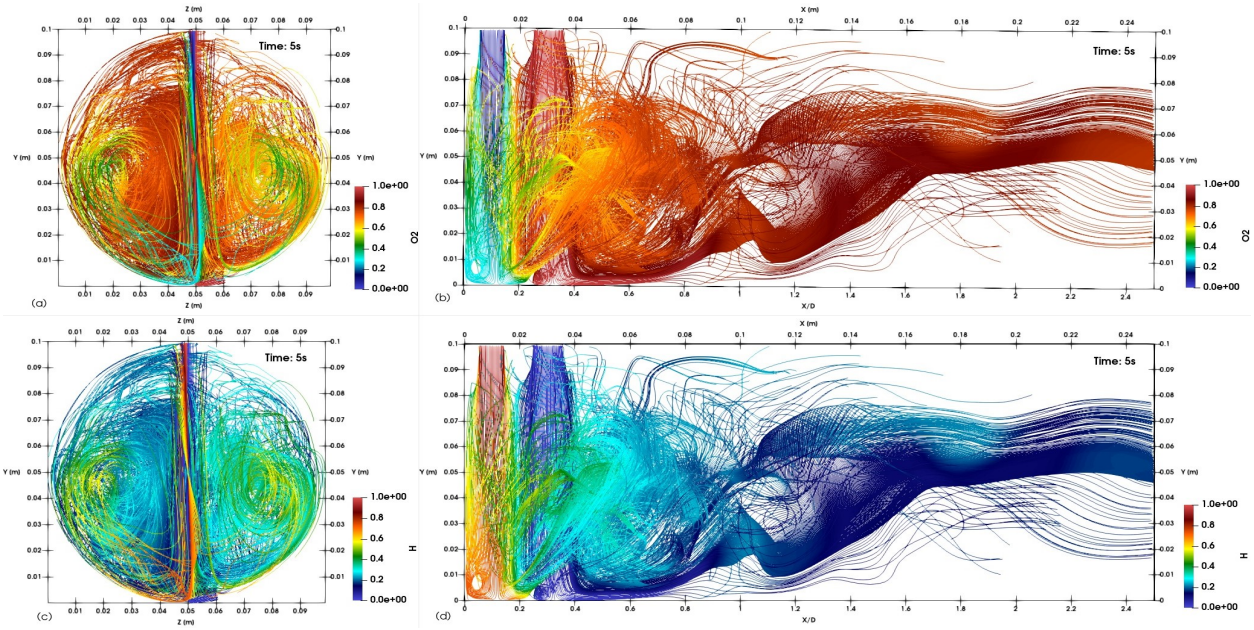

Figure 4.7: Streamline plot of flow at 5s into the simulation (a) oxygen front view (b) oxygen side view (c) hydrogen front view (d) hydrogen side view

The isosurface plot provides an additional method for visualizing the counterrotating flow. Figure 4.8 presents the isosurface of the velocity overlaid with the oxygen mass flow. Unlike the streamline, which maps numerous flow trajectories, the isosurface offers a solid, three-dimensional

visualization of the counterrotation.

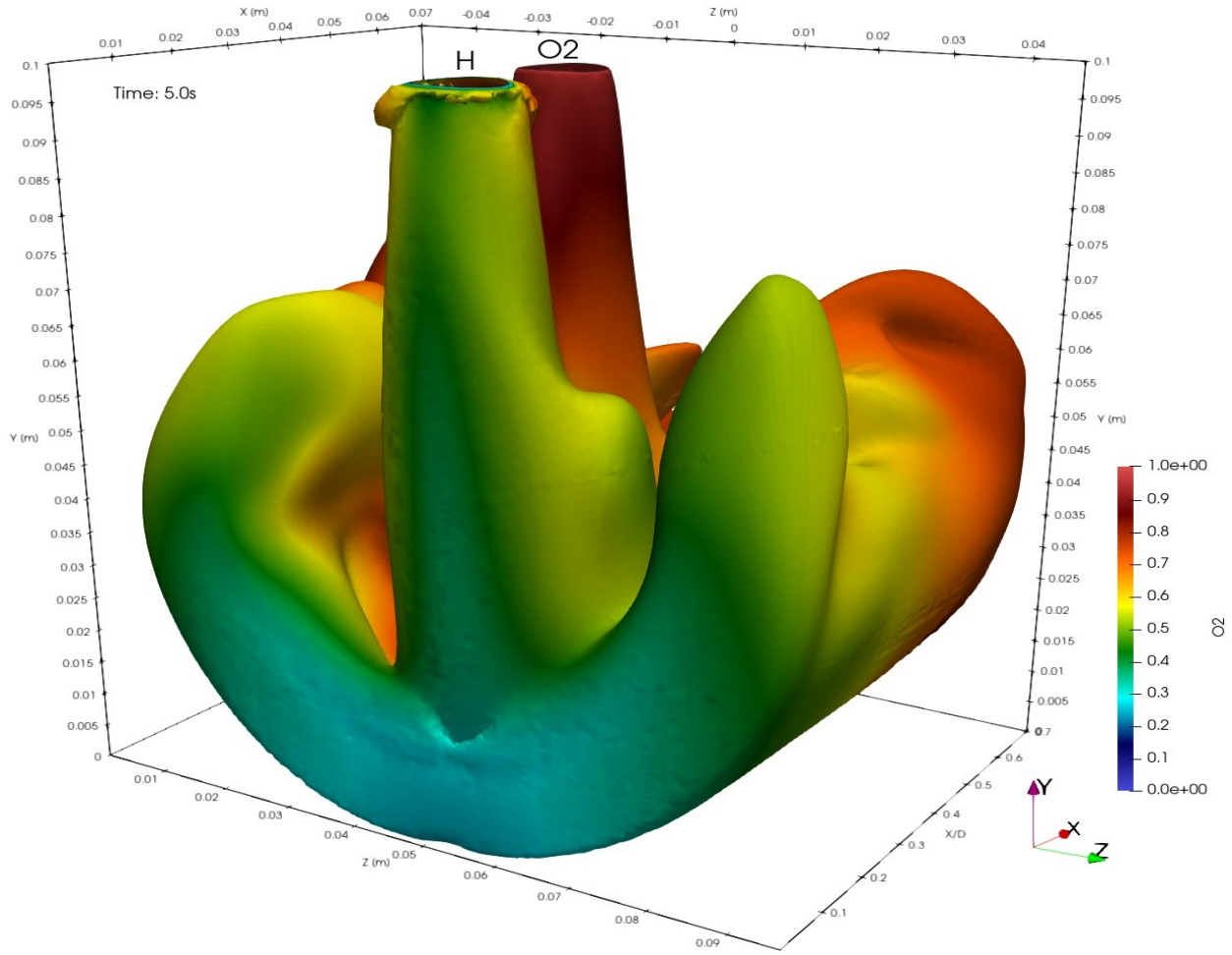

Figure 4.8: Isosurface plot of velocity profile at 5s into the simulation, overlay with oxygen mass flow

4.1 Stability

The conditions for stability are categorized into two types: computational stability and combustion chamber stability. Conditions for computational stability are defined in Chapter 3, whereas physical requirements for combustion chamber stability are outlined in Chapter 1. As presented in Figure 1.1, stability is maintained when the acoustic transit time is much shorter than the vortex

rotation period τ_v. The chamber had a diameter of 0.1m, and the speed of sound in air was 343 m/s, resulting in an acoustic transit time $\tau_a = 0.3ms$.

In Figure 4.9, at 0.1s into the simulation and x=0.1D where the hydrogen inlet was located, the hydrogen flow reaches the opposite side of the cylinder, at which point it turns and begins to counterrotate. This occurs well beyond the acoustic transit time of 0.3ms. The hydrogen flow, as shown in Figure 4.10(a), reaches the opposite end of the chamber first. Both hydrogen and oxygen jets impinge upon the opposite wall directly below the inlet nozzles, Figure 4.11.

The hydrogen inlet speed was set to 10m/s while the oxygen inlet flow speed was 1.5m/s. The time for the largest vortex to complete a full rotation greatly exceeded the acoustic transit time, thereby satisfying the presumed requirement for combustion stability. Specifically, the time for an acoustic wave to travel across the chamber was much shorter than the time required for a vortex to complete one full rotation or the vortex rotation period, $\tau_v \sim 1.5s$.

Figures 4.10 (c) and (d) present the Line Integral Convolution (LIC) mapped over the concentration profile of oxygen and hydrogen. The LIC is calculated directly from the velocity data. The visualization of the flow pattern is generated by tracing the streamlines of the velocity vector field. Essentially, showing the direction and magnitude of the flow and creating a textured pattern that aligns with the streamlines. At 1.5s into the simulation, the upward flow curls inward toward what will become the vortex core. Around this time, the flow begins to develop a counterrotating vortex pair, as discussed in Chapter 1, Figure 1.2

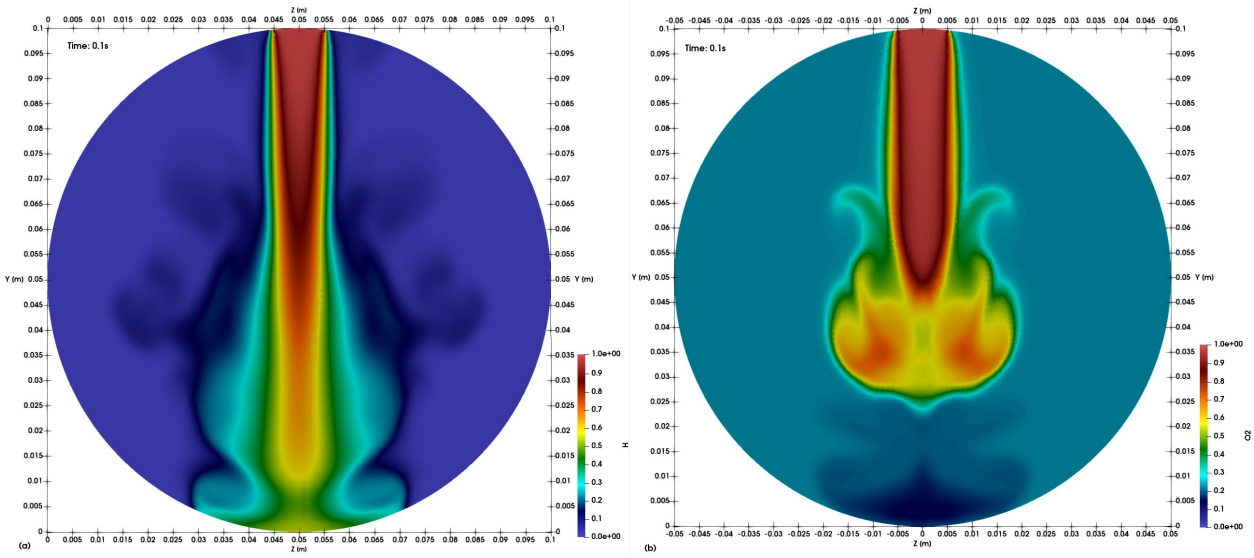

Figure 4.9: Cross section at 0.1s (a) centered at hydrogen inlet at x=0.1D (b) centered at oxygen inlet x=0.3D

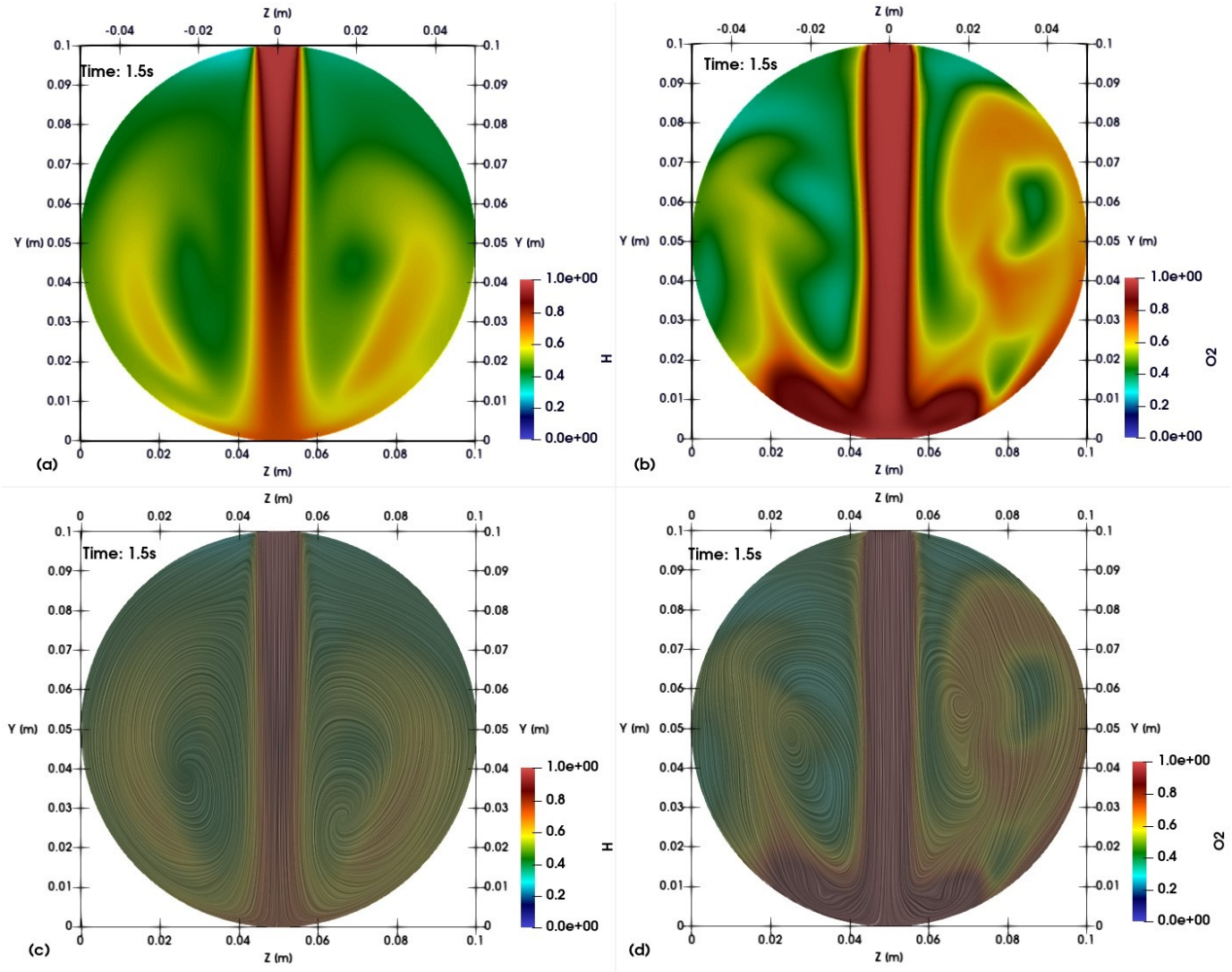

Figure 4.10: Cross section at 1.5s (a) centered at hydrogen inlet at x=0.1D (b) centered at oxygen inlet x=0.3D (c) hydrogen inlet LIC profile (d) oxygen inlet LIC profile

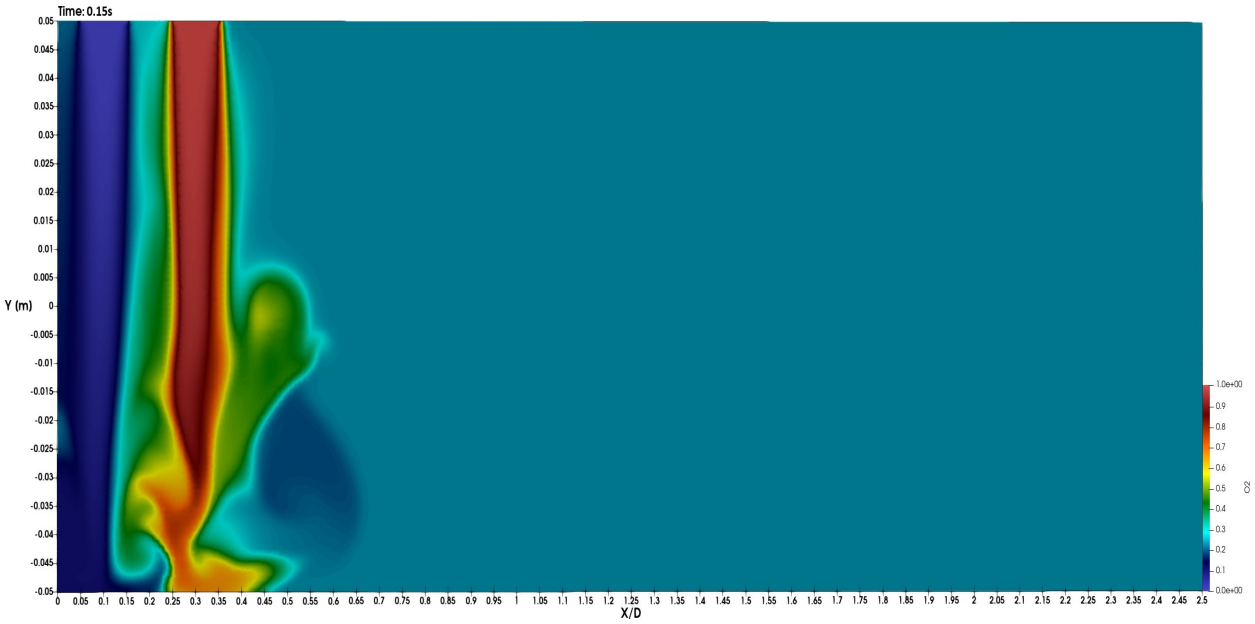

Figure 4.11: Second inlet with oxygen flow traverses down to impinge on the opposite wall directly below at t=0.15s

Chapter 5: Mixing Study

The design of the combustor relied on an understanding of where sufficient mixing was achieved downstream of the inlets. Investigating successive cross sections along the length of the combustion chamber was necessary for isolating areas of appreciable mixing. Cross sectional slices along the combustion chamber were then studied at different simulation timesteps. To identify where near perfect mixing occurred, the concentration profiles of each inert scalar species were analyzed. The total fractions of ambient mass within the chamber were set at 77% nitrogen and 23% oxygen (see Chapter 2.3). As the cylinder filled with hydrogen fuel and oxygen oxidizer, the nitrogen and ambient oxygen were pushed out toward the outlet. Once the mass fraction of nitrogen was purged from the combustion chamber, only fuel and oxidizer remained.

The concentration field downstream of the inlets was simulated at 0.1m intervals, as shown in Figure 5.1. In Figure 5.2(b), at 4s into the simulation, the nitrogen had already been purged up to 1.6D or 0.16m. Nitrogen was purged well before reaching the full length of the combustion chamber (L=0.25m). Indicating that near perfect mixing of the inert species occurred before 1.6D downstream. Therefore, a chamber length of 0.5m was unnecessarily long for this specific transverse jet configuration.

5.1 Equivalence ratio

The equivalence ratio ϕ in combustion refers to the actual fuel-to-oxidizer mixture to the stoichiometric (ideal) fuel-to-oxidizer mixture. This term is used to express whether the mixture is rich in

fuel ($\phi > 1$), lean in fuel($\phi < 1$), or stoichiometric($\phi = 1$). A stoichiometric mixture (equivalence ratio equal to one) indicates regions within the computational domain that are perfectly mixed. The equivalence ratio is defined as:

$$\phi = \frac{(\text{Fuel/Oxidizer})_{experimental}}{(\text{Fuel/Oxidizer})_{stoichiometric}} = \frac{\left(\frac{H}{O_2}\right)_E}{\left(\frac{H}{O_2}\right)_S} = \frac{\left(\frac{O_2}{H}\right)_S}{\left(\frac{O_2}{h}\right)_E} \tag{5.1}$$

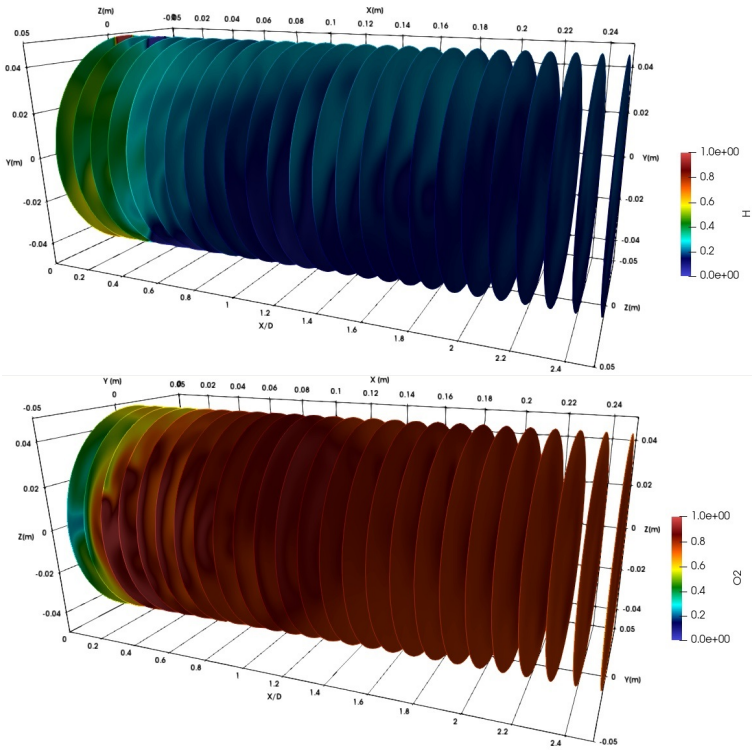

Figure 5.1: Cross sections at 4s into the simulation

The stoichiometric ratio for equation 3.1 was 2:1; that is, for every 2 moles of hydrogen atoms (H), 1 mole of oxygen molecules (O2) was required to react and produce 2 moles of oxygen atoms (O) and 2 moles of hydroxyl radicals (OH). A balanced equation has a coefficient of 2 in front of the hydrogen atom,

$$2\,H + O_2 \longrightarrow 2\,OH \tag{5.2}$$

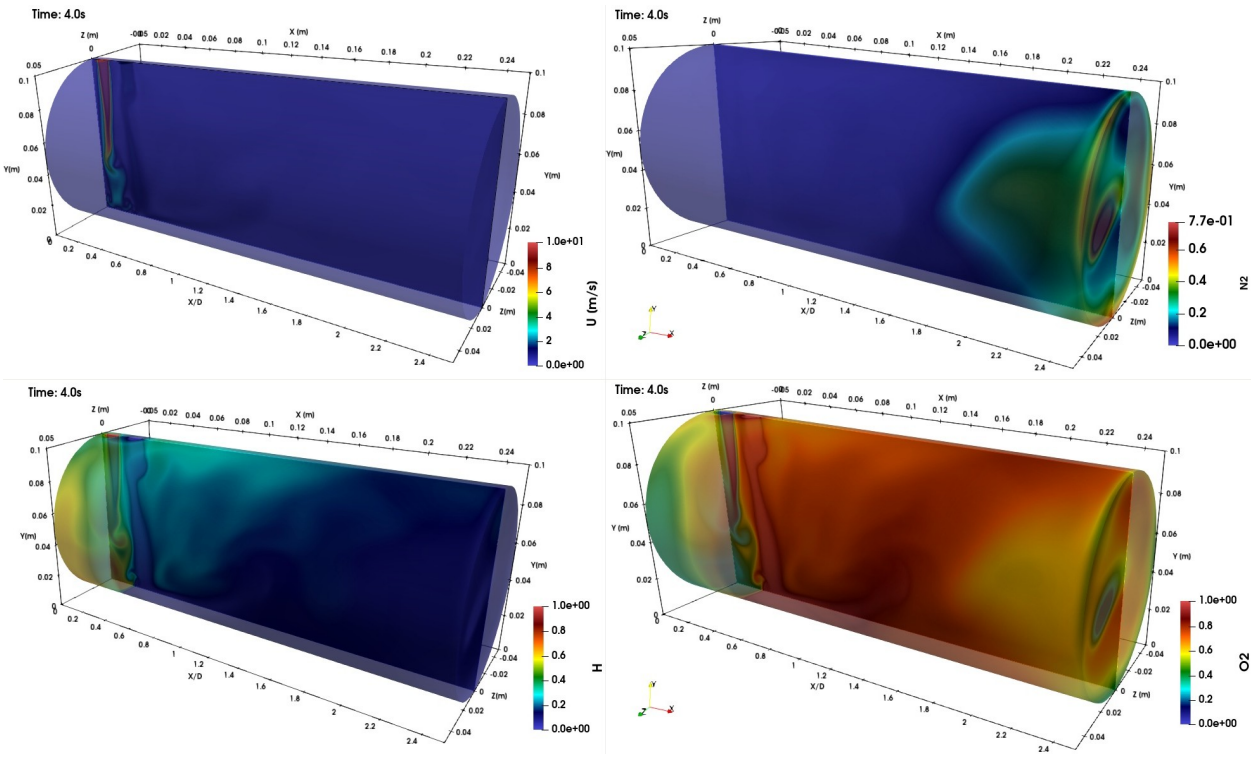

Figure 5.2: LES results at 4s $\Delta x = 1 \times 10^{-3} m, U_H = 10 m/s, U_{O2} = 1.5 m/s$ (a) Velocity profile, (b) Nitrogen mass fraction, (c) Hydrogen mass fraction (d) Oxygen mass fraction

The overall balanced reaction for the combustion of hydrogen to form water was the following.

$$2\,H_2 + O_2 \longrightarrow 2\,H_2O \tag{5.3}$$

The reaction $H + O_2 \longrightarrow O + OH$ was an intermediate step in the overall reaction between hydrogen and oxygen to form water. The overall balanced reaction was analyzed to study the mixing behavior through the equivalence ratio.

The stoichiometric ratio was

$$\left(\frac{O_2}{H_2}\right)_s = \frac{1}{2} \tag{5.4}$$

where $\left(\frac{O_2}{H}\right)_E$ was the experimental ratio calculated from the simulation.

In Figure 5.3b, all the ambient air was purged by 5s. The equivalence ratio was calculated

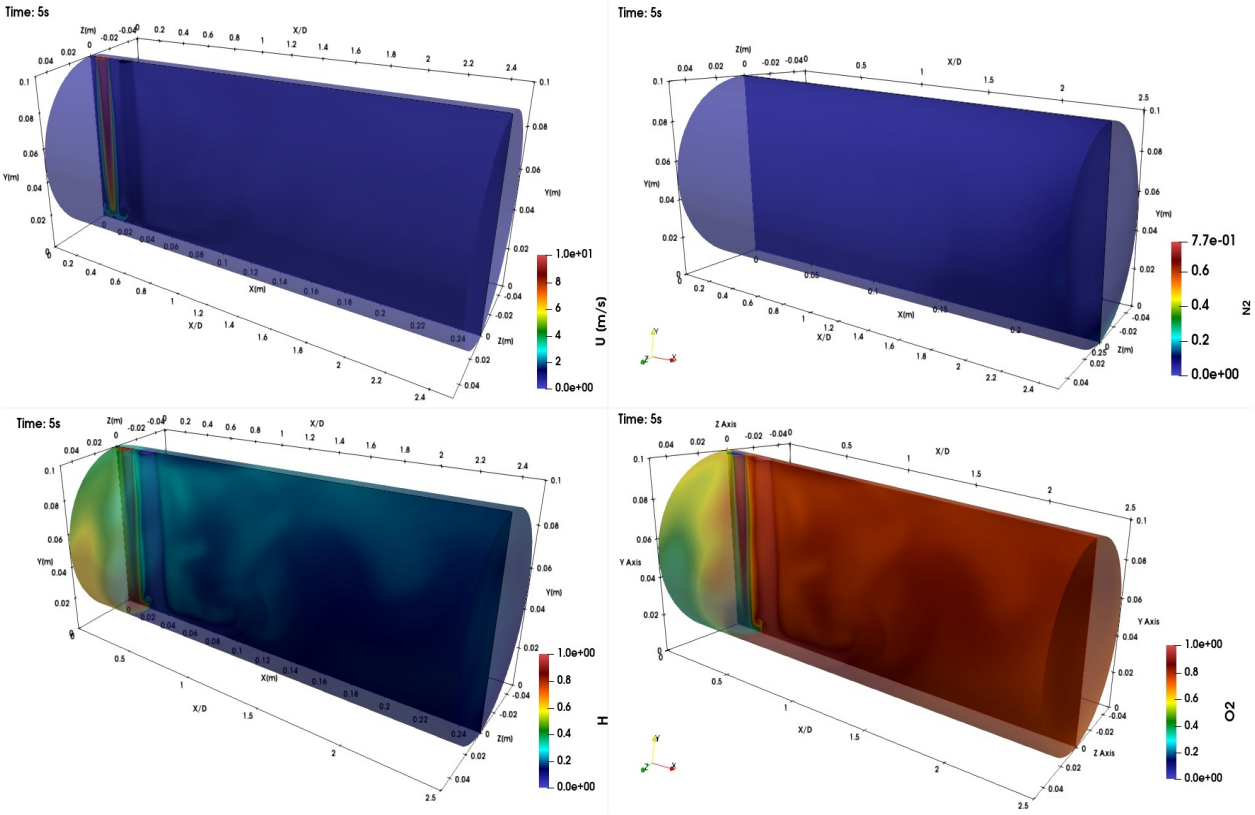

Figure 5.3: LES results at 5s $\Delta x = 1 \times 10^{-3} m, U_H = 10 m/s, U_{O2} = 1.5 m/s$ (a) Velocity profile, (b) Mass fraction of Nitrogen, (c) Mass fraction of Hydrogen, (d) Mass fraction of Oxygen

across each cross section of Figure 5.1. The probability density function (PDF) for the equivalence ratio across each cross section was plotted in Figure 5.4. The PDFs show an equivalence ratio of ϕ>1 across all the cross sectional profiles downstream of the inlets. This indicated that the mixture was fuel rich. The injection was not setup stoichiometrically, hence the higher fuel concentration.

At approximately 0.7D or 0.07m away from the upstream wall, the PDF peaks and appears Gaussian. Consequently, the mass fraction of nitrogen along successive cross sections, shown in Figure 5.7, revealed small traces of nitrogen. At 0.7D, there was still a mass fraction of approximately 0.0015 or 0.15% of nitrogen remaining in the chamber. Further downstream, the successive cross sections showed an increase in nitrogen concentration. The nitrogen while small had not completely purged downstream of the 0.7D. This could lead to skewing the equivalence ratio away from a perfect mixture.

Injecting stoichiometrically would also result in a better mixture. The equivalence ratio was approximately 2 in the PDF's of Figure 5.4, indicating more hydrogen than oxygen. The simulation was initially set up with a one-to-one mass fraction ratio of hydrogen to oxygen at the inlets. Priority was placed on reducing computational complexity by maintaining a Re$\sim$500. The mixing behavior can still be observed and studied regardless of the concentrations. It was not necessary to maintain a near perfect mixture to observe the mixing behavior of each nonreactive species.

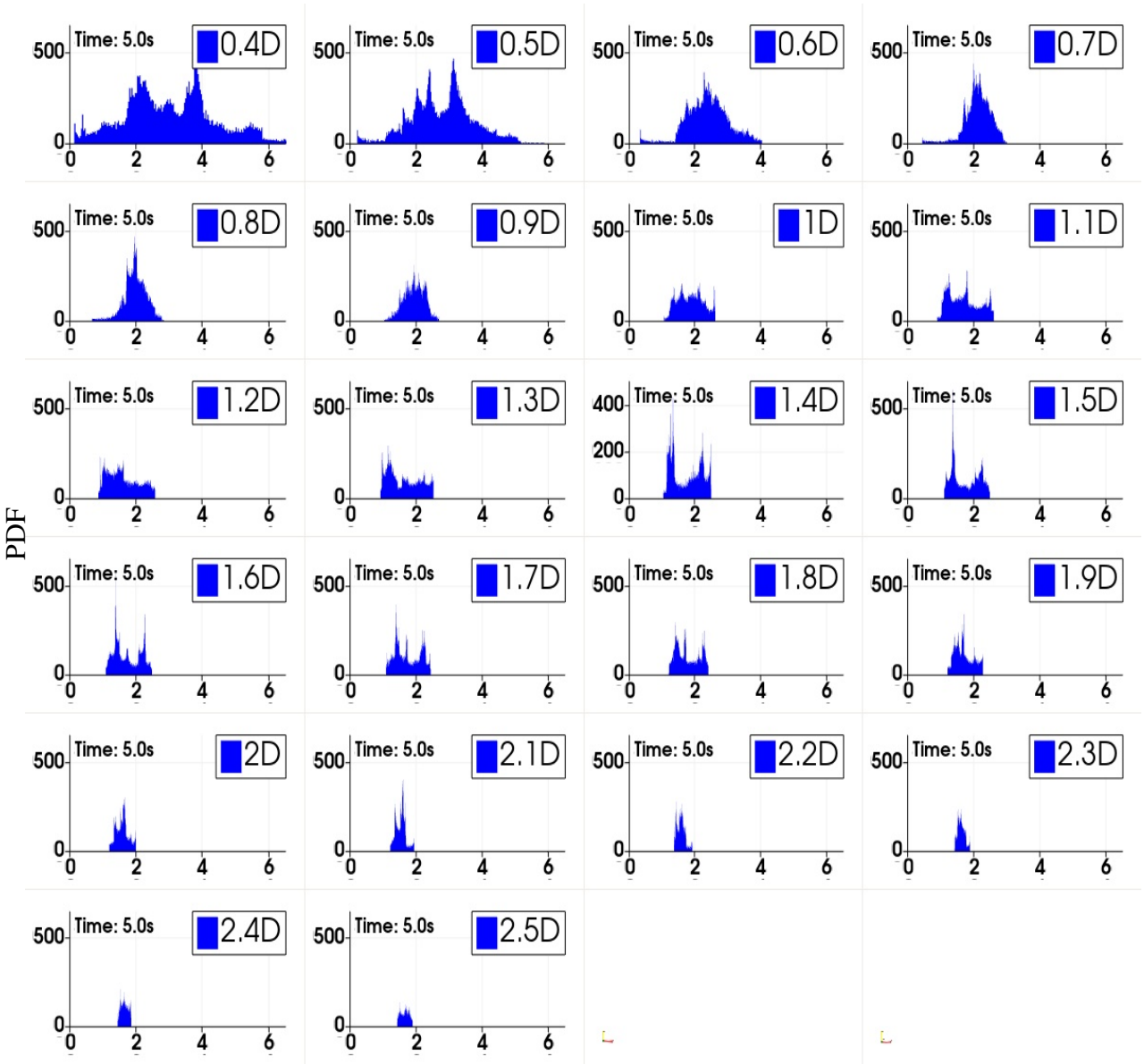

Figure 5.4: Equivalence ratio at 5s and 0.1D cross-sections along the combustion chamber length of 0.25m, x-axis represents the equivalence ratio and the y-axis represents the probability density.

5.2 Concentration Study

The PDF for each inert gas was plotted for cross sections at a $\Delta x = 0.01m$ separation downstream of the left wall (see Figures 2.2 and 5.1). The hydrogen and oxygen inlets were located at 0.1D and 0.3D. The concentration profiles start at 0.4D ahead of the oxygen inlet and end at the outlet of the combustion chamber. At 0.8D and 5s into the simulation, the profiles peak and appear Gaussian. The oxygen profile peaks at 80% and hydrogen at 20%. There was very little to no nitrogen, indicating that the primary fluid was fully purged up to 0.8D downstream from the left wall.

Further downstream, the concentration profiles deviated from Gaussian behavior. Although the nitrogen concentration remained low, it began to increase again, likely influencing the overall concentration profiles and impacting the mixing process. The equivalence ratio beyond 0.8D showed a decreased frequency of mixed fluid, as reflected in the reduced intensity and occurrence observed in the plots. This indicates that the mixing efficiency diminishes after 0.8D, resulting in less mixed fluid downstream.

The areas under each cross section for any particular species are observed to vary when compared to others. This variation occurs because the sum of the concentrations of all constituent species must always be equal to 1 (or 100%) in every cross section. Although the concentration of any individual species changes as the flow progresses downstream from the left wall, the total concentration of all species remains constant at 100%. For instance, at 0.8D, the PDF of oxygen concentration peaks at approximately 80%, hydrogen is around 20%, and nitrogen at 0%. This all adds to 100% concentration at 0.8D. Together, these values sum to 100% at this cross, demonstrating the conservation of total concentration. This behavior is consistent across all cross sections, indicating that conservation property is upheld throughout the flow.

This conservation property is essential for maintaining the validity of the simulation. It ensures that the observed variations in individual species' concentrations are attributed to the mixing and reaction dynamics within the system, rather than errors or inconsistencies in the computational

setup. Furthermore, this principle validates the accuracy of the simulation results and highlights the importance of monitoring how the constituent species evolve along the length of the combustion chamber.

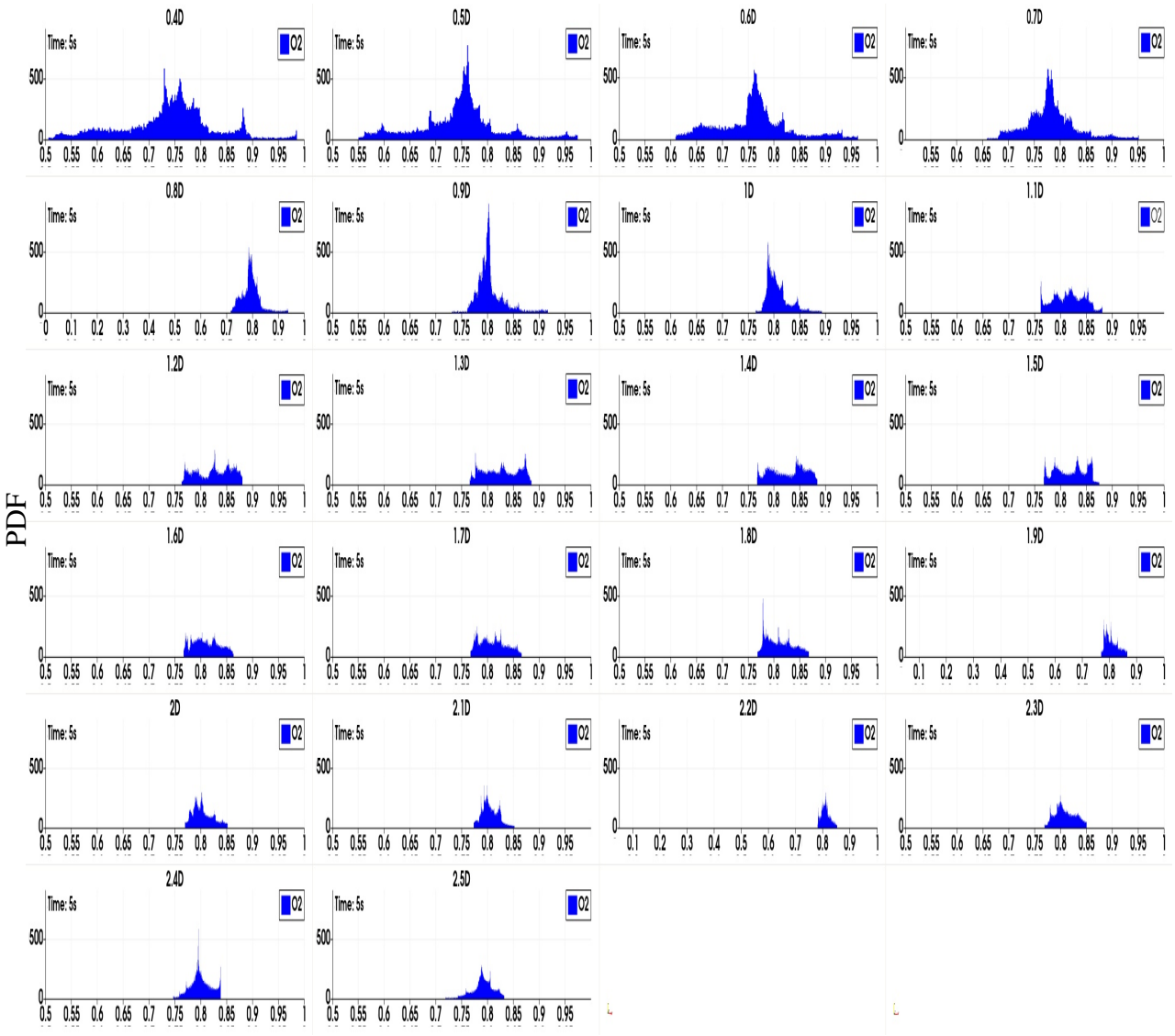

Figure 5.5: Oxygen concentration at 5s for cross section profiles downstream of inlets with combustion chamber L=0.25m, the x-axis represents the oxygen mass fraction, and the y-axis represents the probability density.

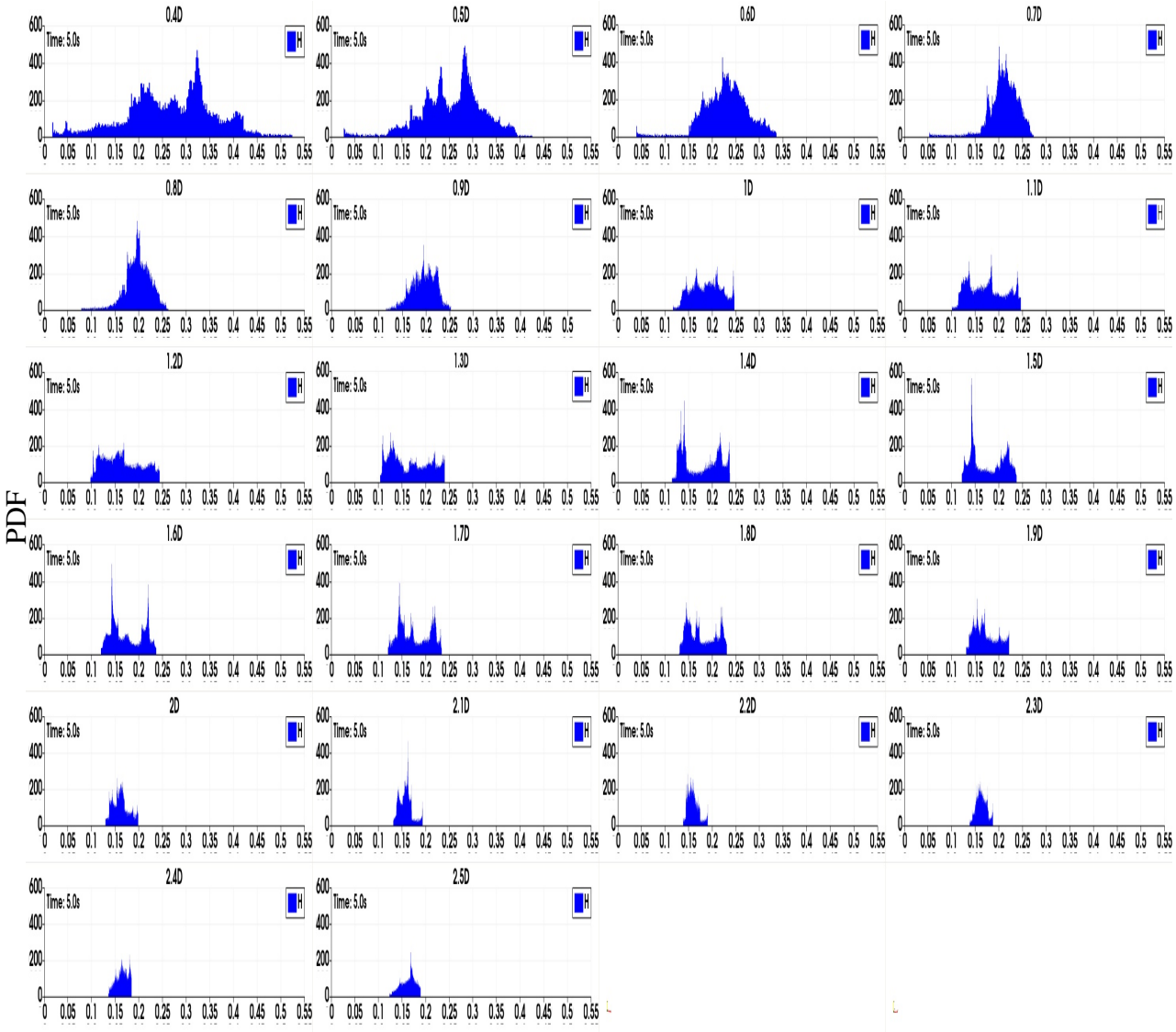

Figure 5.6: Hydrogen concentration at 5s for cross section profiles downstream of inlets with combustion chamber L=0.25m, the x-axis represents the hydrogen mass fraction, and the y-axis represents the probability density.

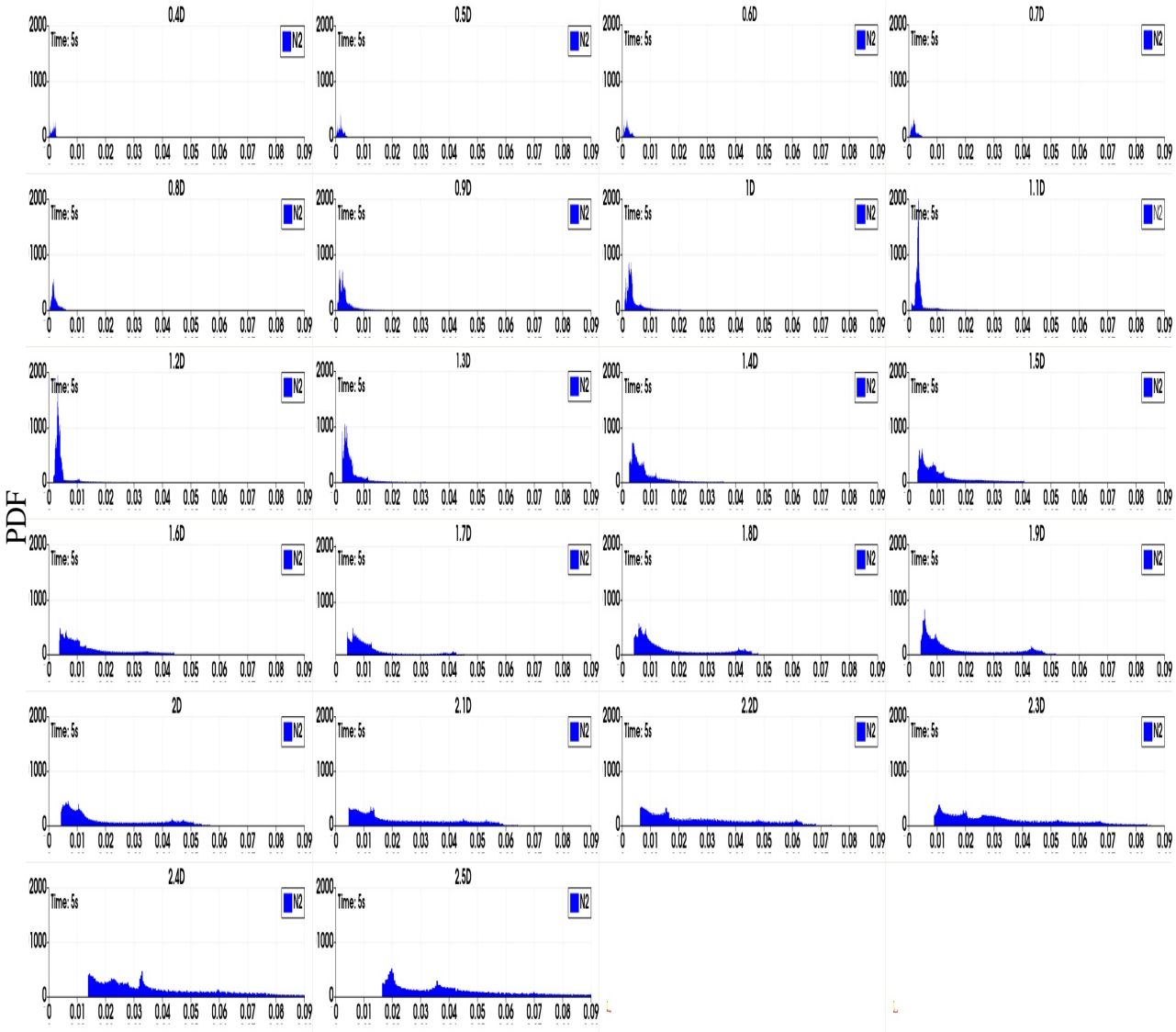

Figure 5.7: Nitrogen mass fraction at 5s for a cross section profiles downstream of inlets with combustion chamber L=0.25m, x-axis represents the nitrogen mass fraction and the y-axis represents the probability density.

The integral of the concentration in each cross section is presented in Figure 5.8. This integral represents the total concentration, corresponding to the area under the curve at each cross section. After 1D, the oxygen and hydrogen integrals remain approximately constant. Prior to 1D, nitrogen had zero total concentration at each cross section. However, beyond 1D, the nitrogen integral begins to increase, indicating a small but detectable presence of nitrogen. Hydrogen, being lighter, accelerates in the streamwise direction under the influence of the initial pressure gradient in the chamber. It moves significantly faster downstream compared to the heavier oxygen. In the near field, closer to the inlets, hydrogen accelerates more rapidly than oxygen. By 5s into the simulation, a steady-state, statistically stationary concentration profile is established within the cavity. Consequently, the total hydrogen concentration decreases downstream due to the initial pressure gradient, which continues to accelerate hydrogen away from the inlet.

Using the integral of each cross section, normalized PDFs were plotted and are found in Appendix E. The area of each normalized PDF is approximately one.

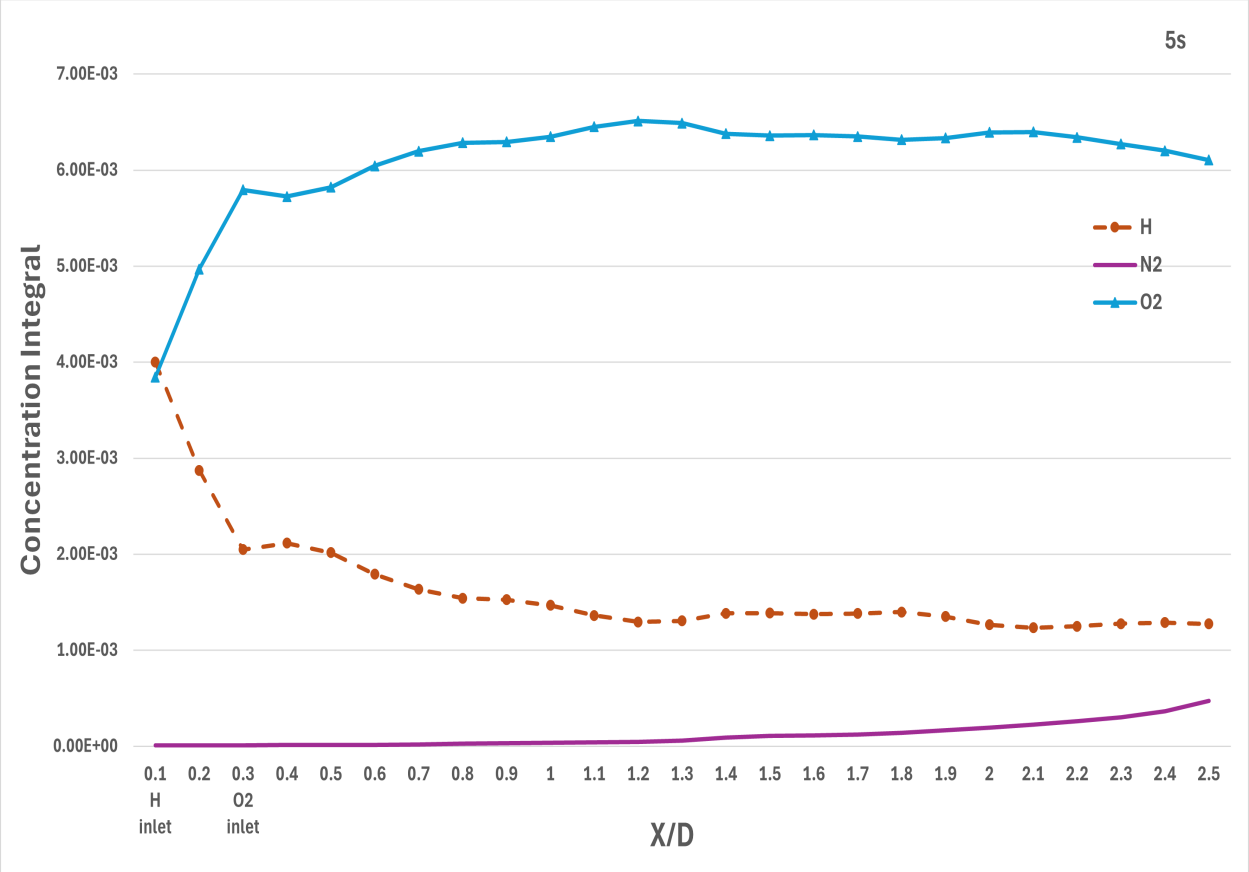

Figure 5.8: Integral of concentrations each cross sectional 0.1D slice

5.3 Concentration Over Time

Further examination was conducted to the concentrations over time and along the length of the combustion chamber. The PDF of the concentration profiles from section 5.2, begins to exhibit a Gaussian at 0.7D and 0.8D. This observation is consistent with the results for the equivalence ratio shown in Figure 5.4 where a fuel-rich mixture is identified at these locations.

It can be inferred that the first location where the flow approaches a near perfectly mixed state is at 0.7D. The slice at 0.7D marks the downstream position where the constituent nonreactive species were most optimally mixed. To investigate the concentrations over time, probes were placed at this location, see Figure 5.9. Specifically, at 0.7D, nine points arranged in a grid pattern were used to probe the slice, yielding detailed insights into the flow behavior at this location.

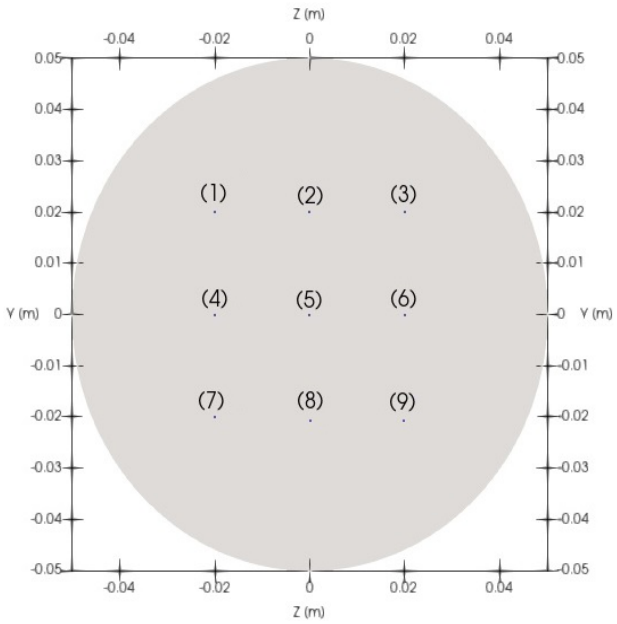

Figure 5.9: Cross section with nine probes

In Figure 5.10, the concentrations of the nine points across the slice at a distance of 0.7D downstream were plotted over time. The mass fraction of oxygen and hydrogen gradually increased, while nitrogen decreased. By 5s, oxygen asymptotically reached a concentration of approximately

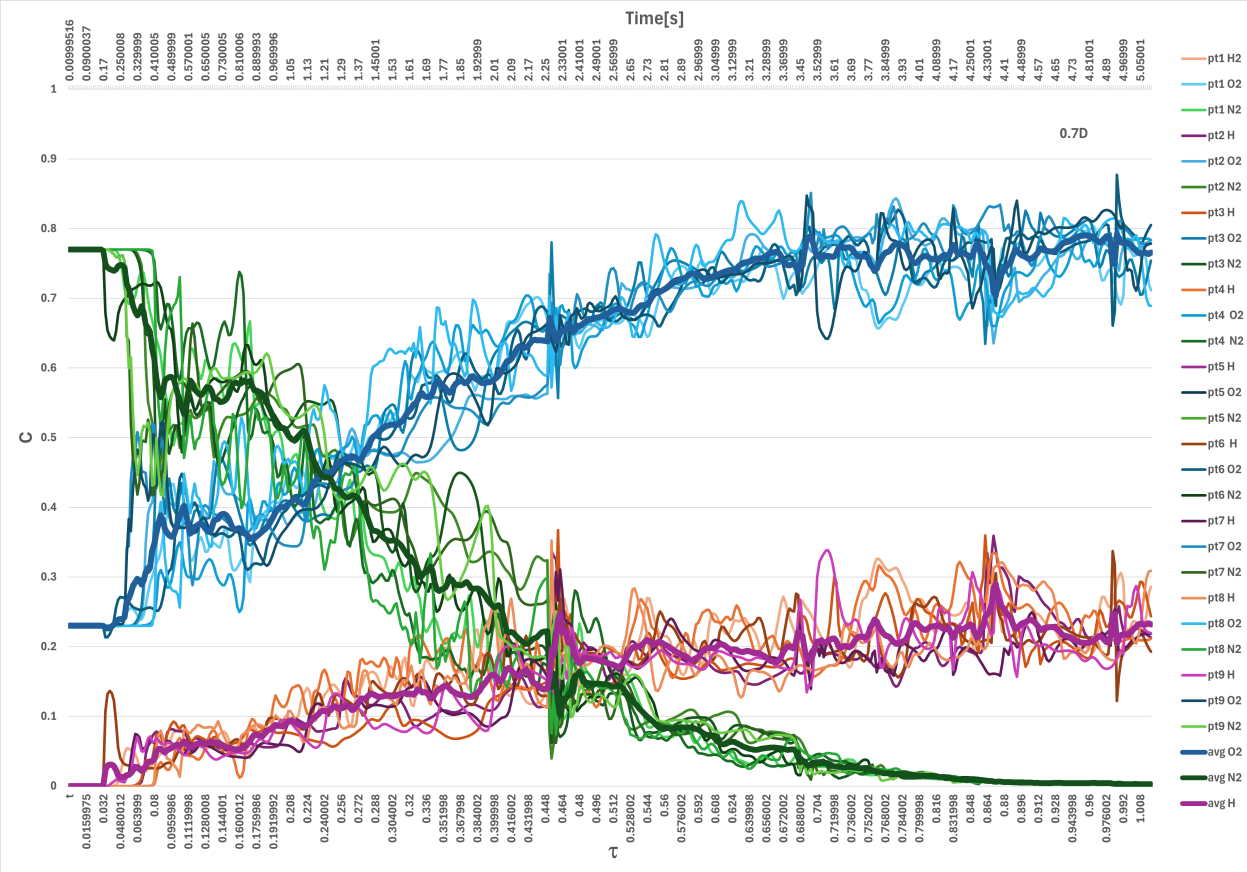

Figure 5.10: Mass fraction Concentrations over time with overlapping average at a cross sectional slice 0.7D downstream of the combustion chamber left wall

80%. The maximum concentration of hydrogen was about 20%. Nitrogen was purged out of the chamber by the constituent nonreactive species and its concentration dropped to about zero by 4s. At about 3s, the plots for oxygen and hydrogen reached an inflection point before the final concentration was reached. There is are large jumps in concentration at about 2.3s from the nitrogen and hydrogen concentrations. It is at this point where the hydrogen overtakes the nitrogen. There is a notable jump in the average concentration of hydrogen before it comes back down to its final value. Conversely, there is a dip in the nitrogen at the same time followed by a small rise before gradually decreasing to zero. Oxygen has a similar behavior but is not as notable as that of hydrogen. By about 2.3s into the simulation the nitrogen and hydrogen concentration reach a point where they are approximately equal in concentration. This is a turning point where the hydrogen overtakes the

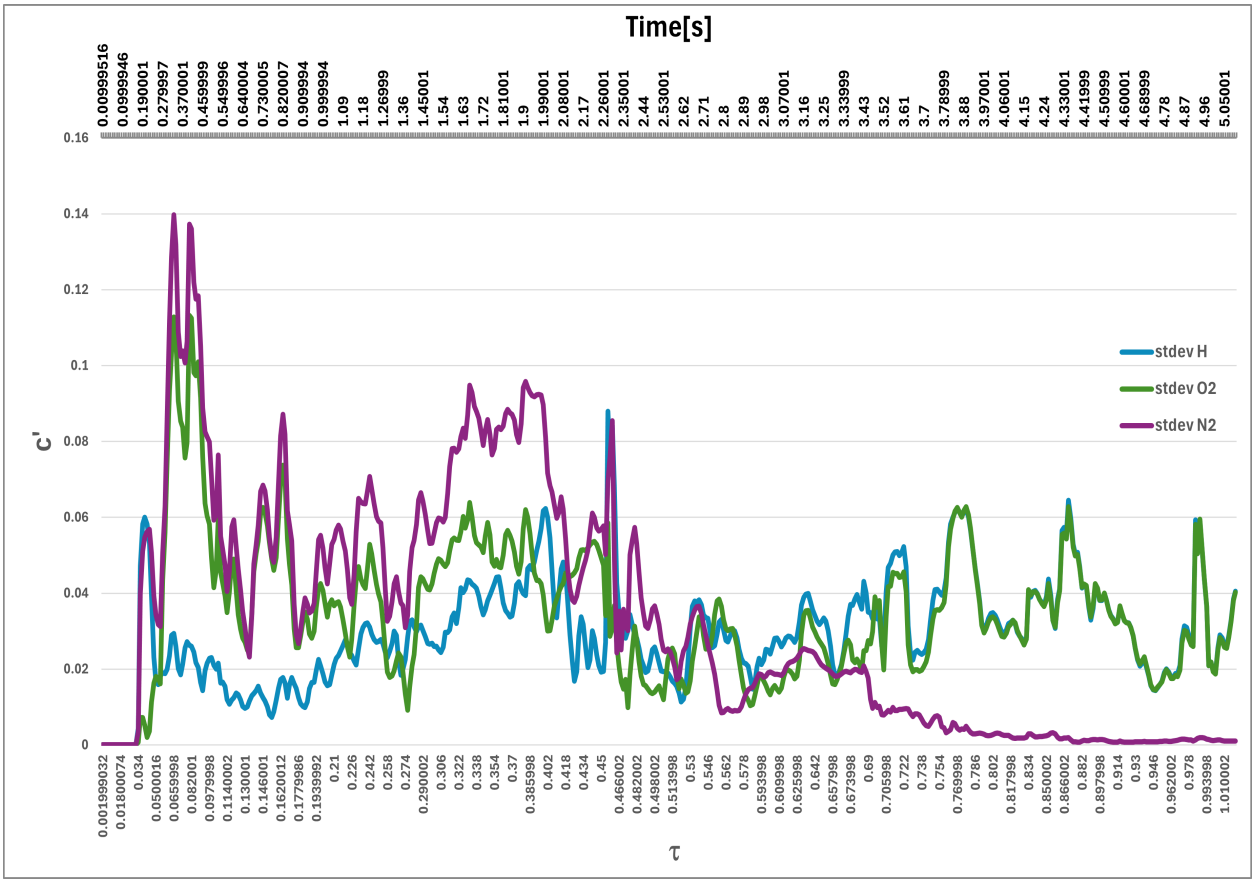

Figure 5.11: Standard deviation of the mass fraction concentrations over time at a cross-sectional slice 0.7D downstream of the combustion chamber left wall

nitrogen.

The standard deviation represents the concentration fluctuations for each species in the combustion chamber and is plotted in Figure 5.11. Significant variations in concentration fluctuations appear before 2.5s for each constituent species. After 2.7s, the standard deviation dropped to near zero for nitrogen, indicating that any primary gas or the ambient air is effectively purged by 4s.

A different scenario happens with the oxygen and hydrogen. Around 3.7s, the fluctuations indicated by the green and blue lines begin to merge. Once the primary gases are fully purged, any fluctuations in hydrogen concentration become equal and opposite to those in oxygen, as there is essentially no third or ambient air to influence the injected species. As no other gases remain except for the injected oxygen and hydrogen, when one gas goes up in concentration the other goes

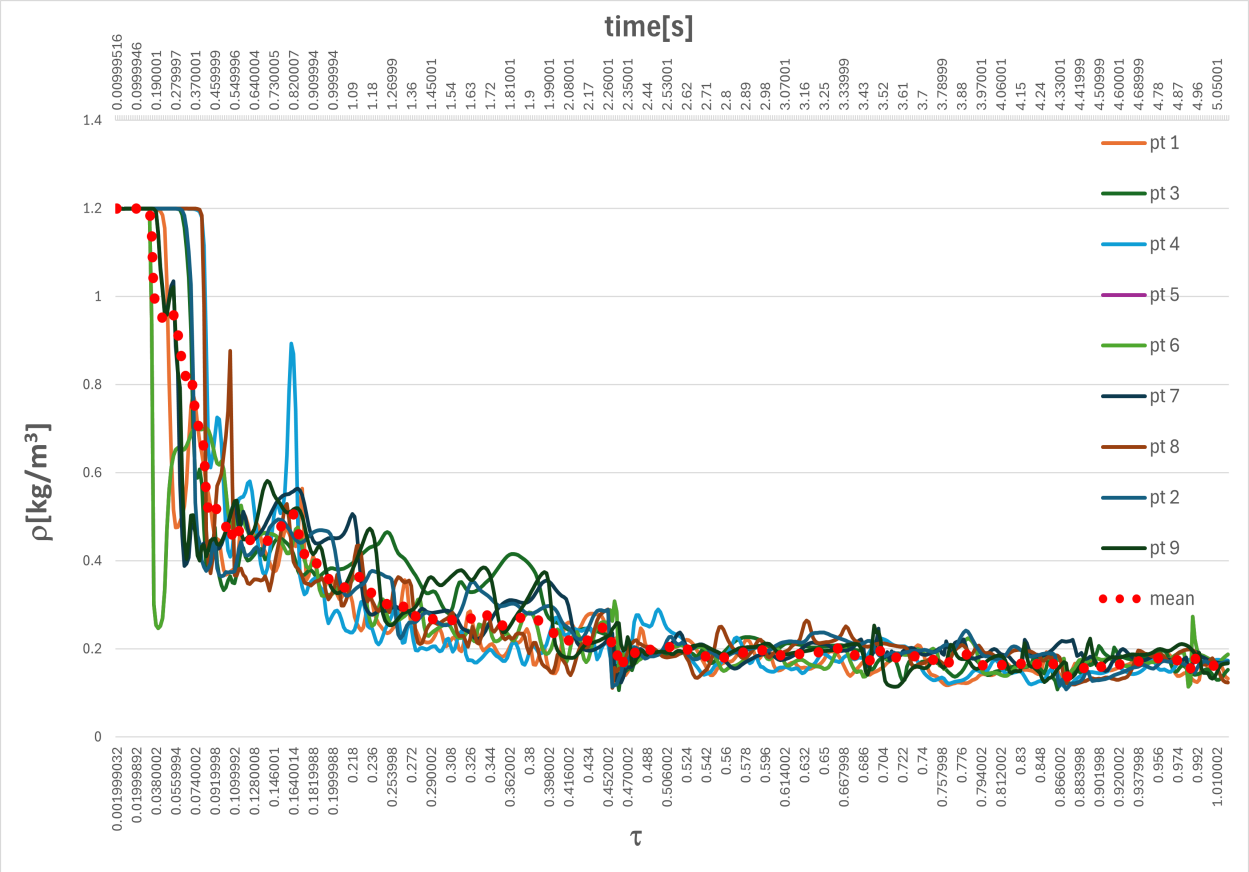

Figure 5.12: Density over time at of 9 probe points, at cross section 0.7D downstream from the left wall

down. As a result, their standard deviations must match exactly. The fluctuations, indicated by the blue and green lines, subsequently merge and follow a synchronized trend.

The plot of the density over time, Figure 5.12, shows that the density across all points in the cross section had larger variations before 1s. After 1s, changes in density across the cross section converge to a final value of approximately $0.2kg/m^2$. The standard deviation of the density is plotted in Figure 5.13 and represents fluctuations in density. At about 2.3s, the fluctuations start to reduce. Between 2.3 and 5s, the standard deviation remains somewhat constant and below $\rho = 0.05$. The corresponding time of 2.3s, from the concentration profiles of Figure 5.10, shows that this time is where the hydrogen overtakes the nitrogen concentration. It is represented as a larger bump in the hydrogen concentration and a dip in the nitrogen concentration. Nitrogen is

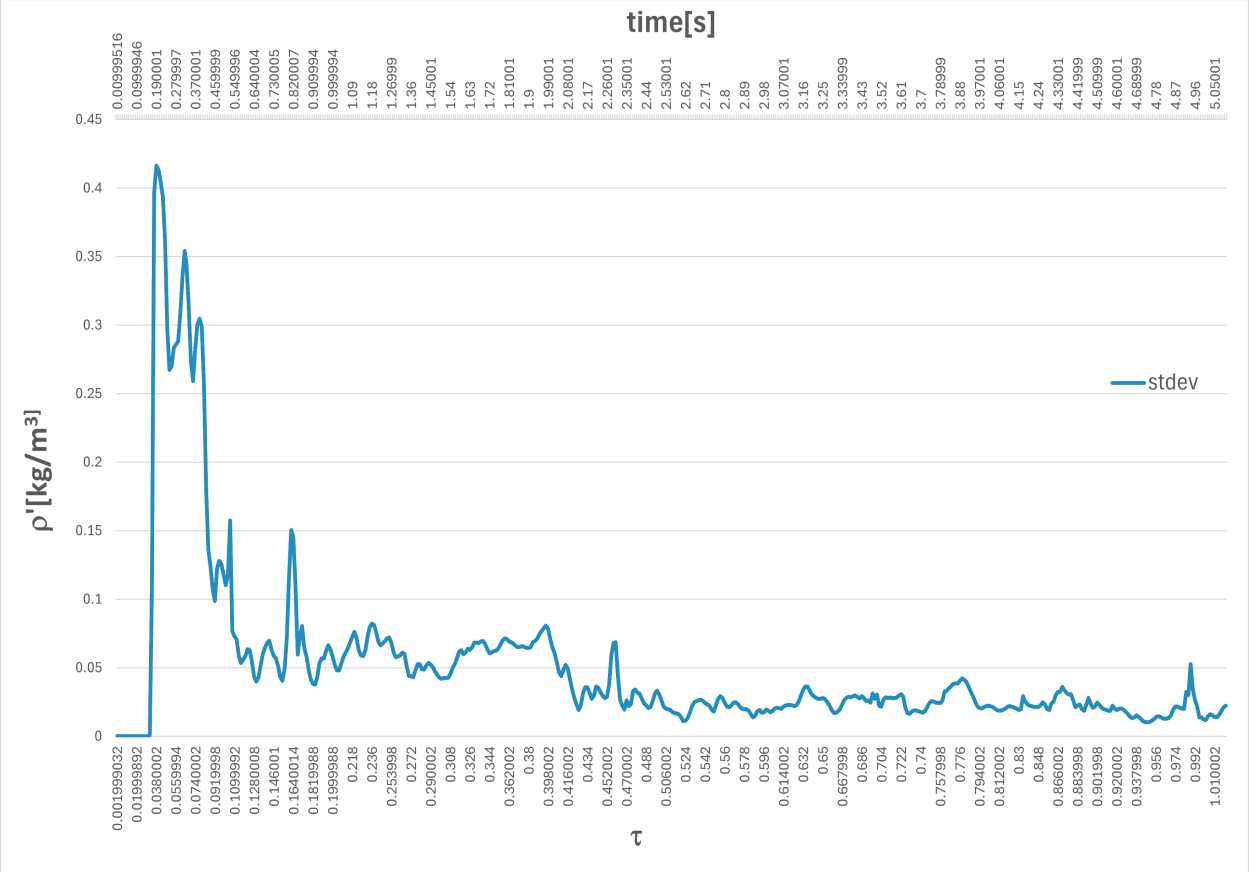

Figure 5.13: Standard deviation over time of density across 9 probes points, cross section 0.7D of the left wall

followed by a gradual decline to zero concentration and hydrogen is followed by an asymptotic increase to its final concentration.

Each plot of concentration, average, standard deviation, and density reveals an inflection point at approximately 2.3s into the simulation. After this point, hydrogen and oxygen become the dominant species in the chamber, asymptotically reaching their final concentrations. Fluctuations in mixing are captured in standard deviation plots. Density fluctuations decrease to nearly zero after 2.3s. While, concentration profiles exhibit a slightly different trend. The fluctuations in oxygen and hydrogen concentrations merge around 3.7s, indicating that beyond this point, both species are fully mixed into a single fluid composition with a constant density, exhibiting similar behavior.

The nine-point probes used to examine the cross section at 0.7D are extended to probe lines along the length of the cylinder; see Figure 5.14. The concentration for each probe line at 5s into the simulation is plotted in Figure 5.15. The hydrogen inlet is located 0.1D away, and the oxygen 0.3D away from the left wall. That is reflected in the plot of concentration along the length of the cylinder by a hydrogen spike at 0.1D and an oxygen spike at 0.3D. Further downstream of the inlets, the concentrations of hydrogen and oxygen across the nine probe lines begin to converge at approximately 0.7D downstream. This is where perfect mixing was observed in the PDFs of the concentration and the equivalence ratio, chapter 5.1 and chapter 5.2. Consequently, at 5s into the simulation, nitrogen is completely purged up to a distance of 1.2D downstream of the inlets.

There were three different methods for looking at the concentration of the inert scalars and primary fluid within the chamber. The first was to look at the probability density functions, PDFs, of the transverse slices downstream of the inlets. This was a spatial analysis where the time was constant and the position of the slices changed. The second was a temporal analysis in which nine-point probes were placed on a cross-sectional slice. The concentrations for the second method were sampled over time. The third method was another spatial analysis that extended the nine-point probes into lines along the length of the cylinder.

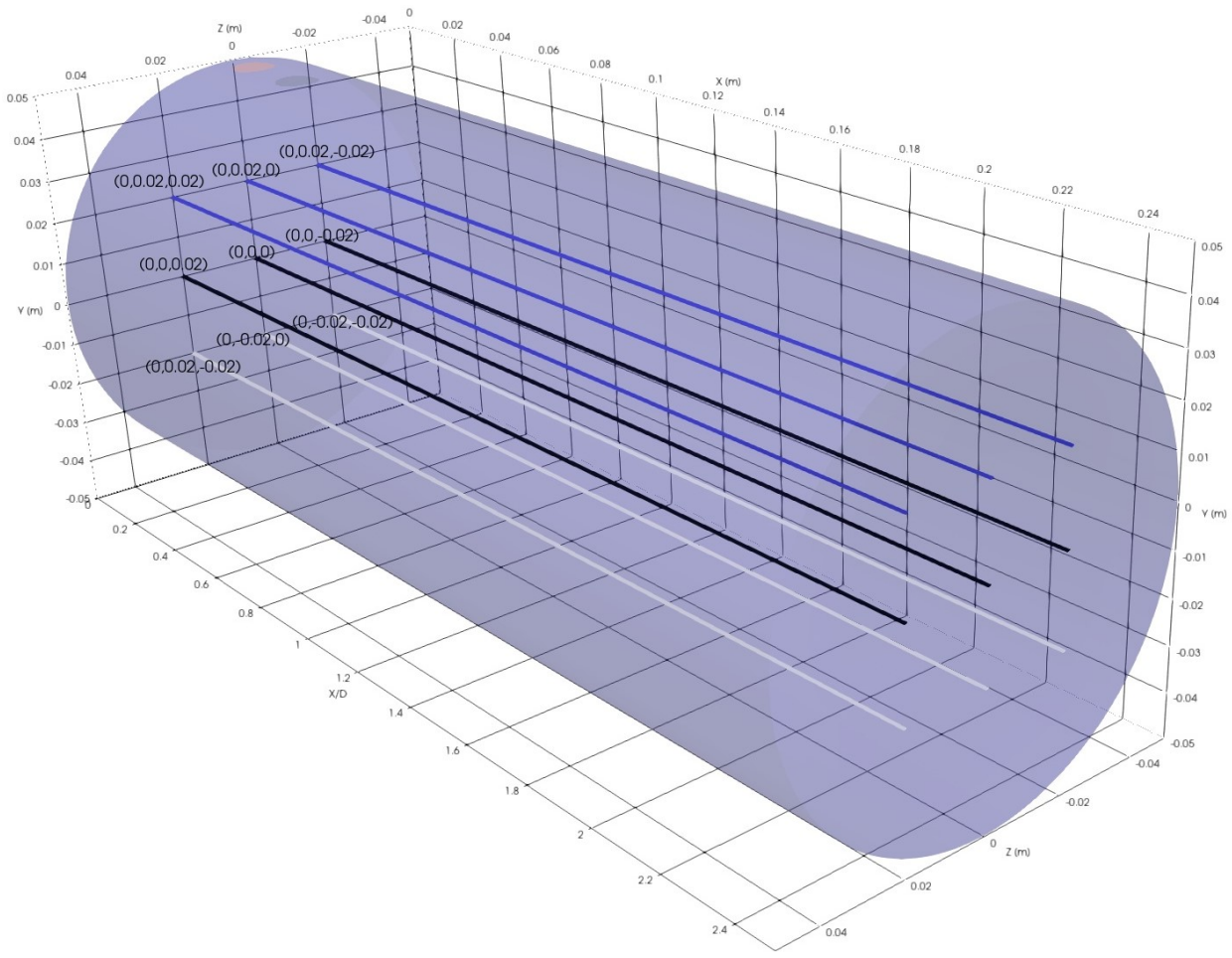

Figure 5.14: Probe lines along the length of the combustion chamber

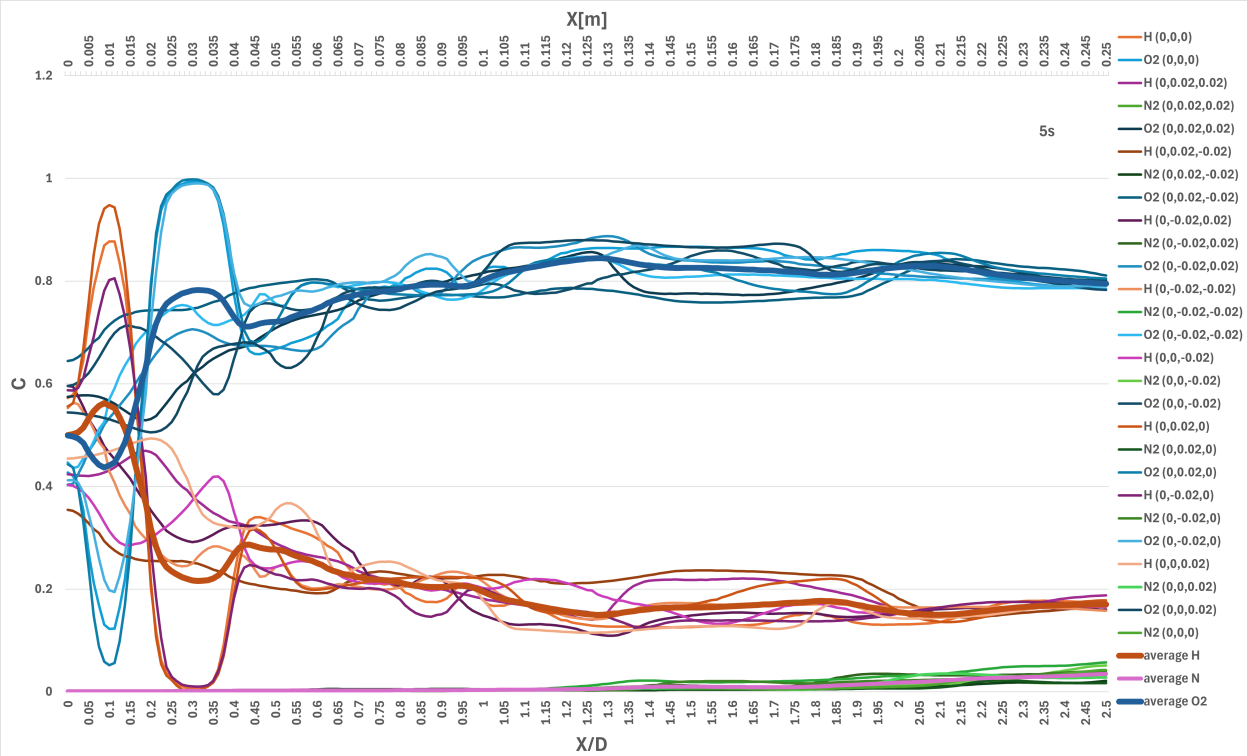

Figure 5.15: Mass fraction concentrations probe lines along the length of the combustion chamber at 5s into the simulation

5.4 Concentration and Velocity Fluctuations

At 5s into the simulation, the mean, standard deviation, and concentration fluctuations over the entire cross sections were examined. In Figure 5.16, the mean concentration in the entire cross section is represented as $\bar{c}$ and is plotted on the y-axis. Tabulated details can be found in the Appendix D.1

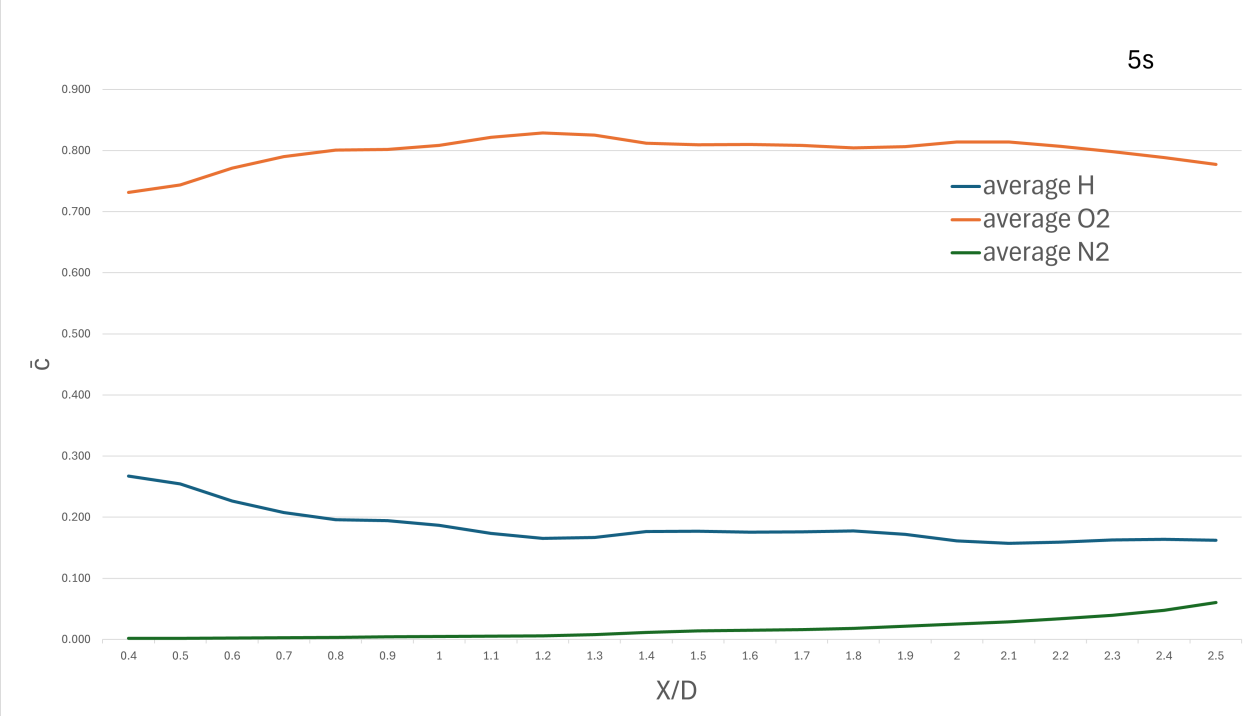

Figure 5.16: Mean concentrations at downstream cross-sections 5s into simulation

The standard deviation represents the concentration fluctuations; see Appendix D.2. Fluctuations in concentration across the cross section as a function of downstream distance are shown in Figure 5.18. The x-axis is nondimensionalized using the X/D ratio, representing stations downstream of the inlets. A 1/X relationship is observed between 0.4D and 0.7D. Beyond 0.7D, the fluctuations begin to increase, indicating that concentration variability is influenced by any remaining residual primary gas.

The green line in Figure 5.17 represents the remaining nitrogen, which was part of the original

gas composition. Additionally, the primary gas consisted of 23% oxygen. The interaction between these two components contributes to the observed fluctuations, reflecting the dynamic behavior downstream.

The ratio of the concentration fluctuations with that of the mean is shown in Figure5.18, see Appendix D.3. Nitrogen has the most amount of variation from its mean value. Meanwhile, oxygen and hydrogen follow a decline up to 0.9D. After this point, hydrogen levels off to a steady state while oxygen experiences more variations. The residual primary oxygen would likely follow the same patterns as that of the nitrogen. Hence, this contributes to more variations in the oxygen profile. The nitrogen represented by the green line has the most variations. This happens because the average nitrogen concentration is very small; see Figure 5.16. Dividing by a small number would result in large variations. In contrast, the mean concentration for oxygen and hydrogen levels off at a higher concentration than that of nitrogen. Resulting in less variation in their concentration fluctuation ratio.

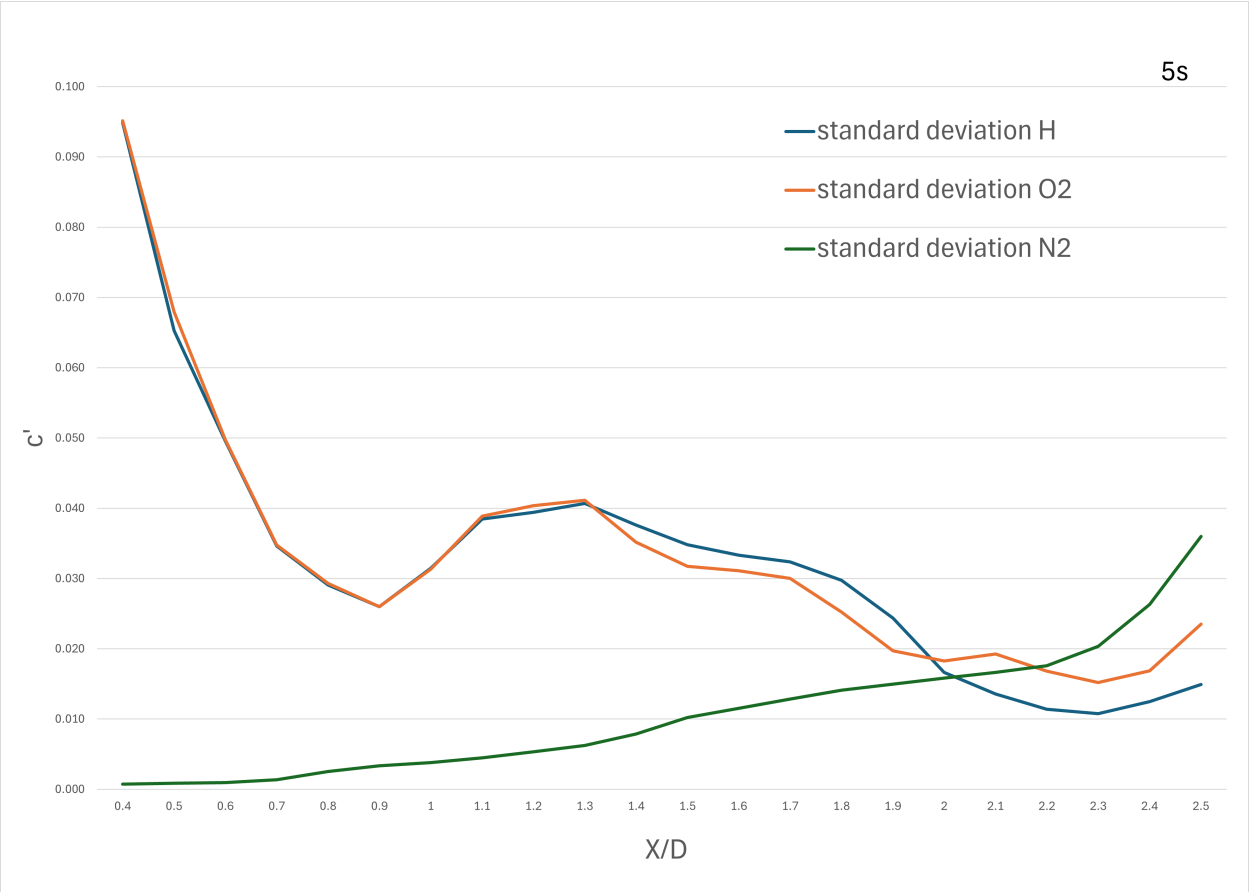

Figure 5.17: Concentration fluctuations at downstream cross sections 5s into simulation

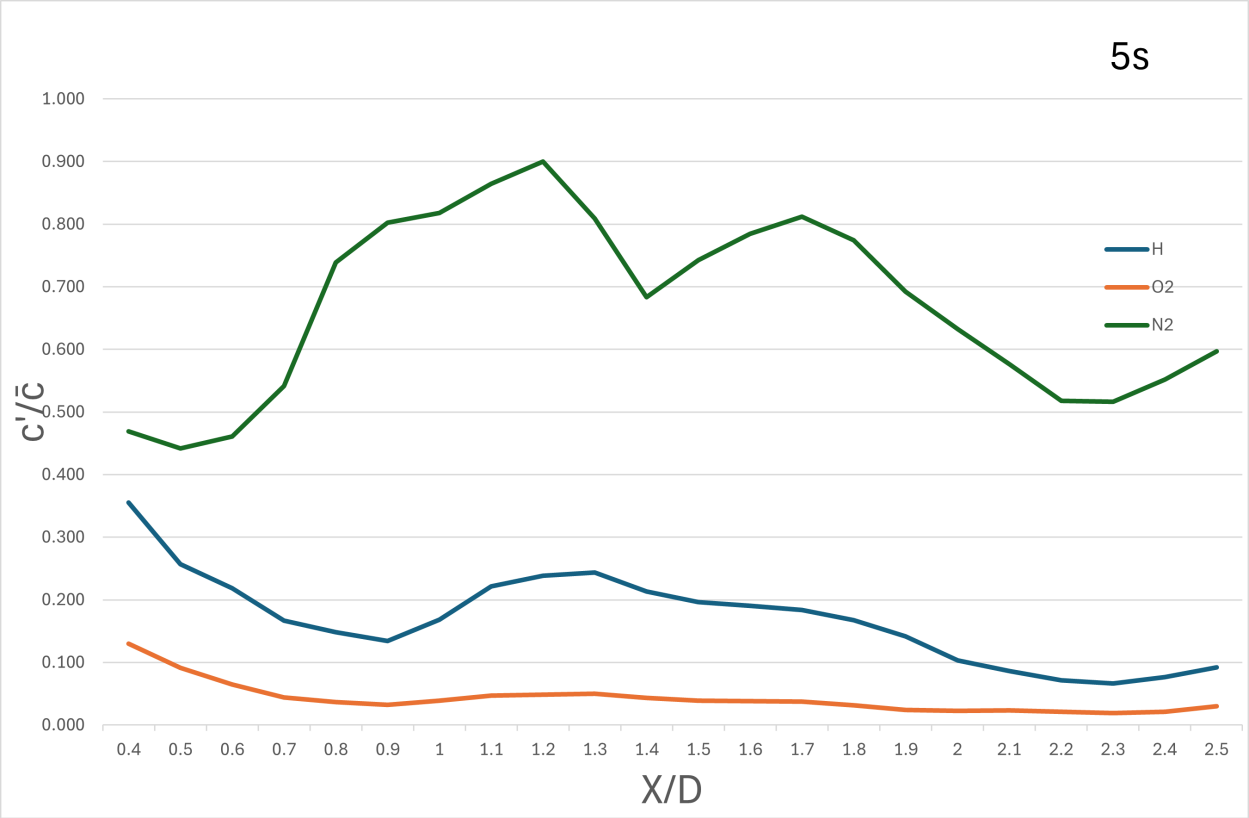

Figure 5.18: Concentration fluctuation ratio at downstream cross sections 5s into simulation

A fit was made to the concentration fluctuation ratio for hydrogen and oxygen to compare the simulation results with that of mixing theory stated in equation 1.5 and plotted in Figure 5.19. Using a Galilean transformation, the concentration fluctuations can be expressed as a function of velocity and distance.

$$\frac{c'}{\bar{c}} = \frac{\tau}{t} = \frac{\tau U}{x} \tag{5.5}$$

where $\tau \sim 1.5s$ is the time it takes the vortex to complete one full rotation and was obtained directly from the simulation results, see Figure 4.10. The velocity is the inlet velocity for hydrogen and oxygen and a scaling factor to the numerator.

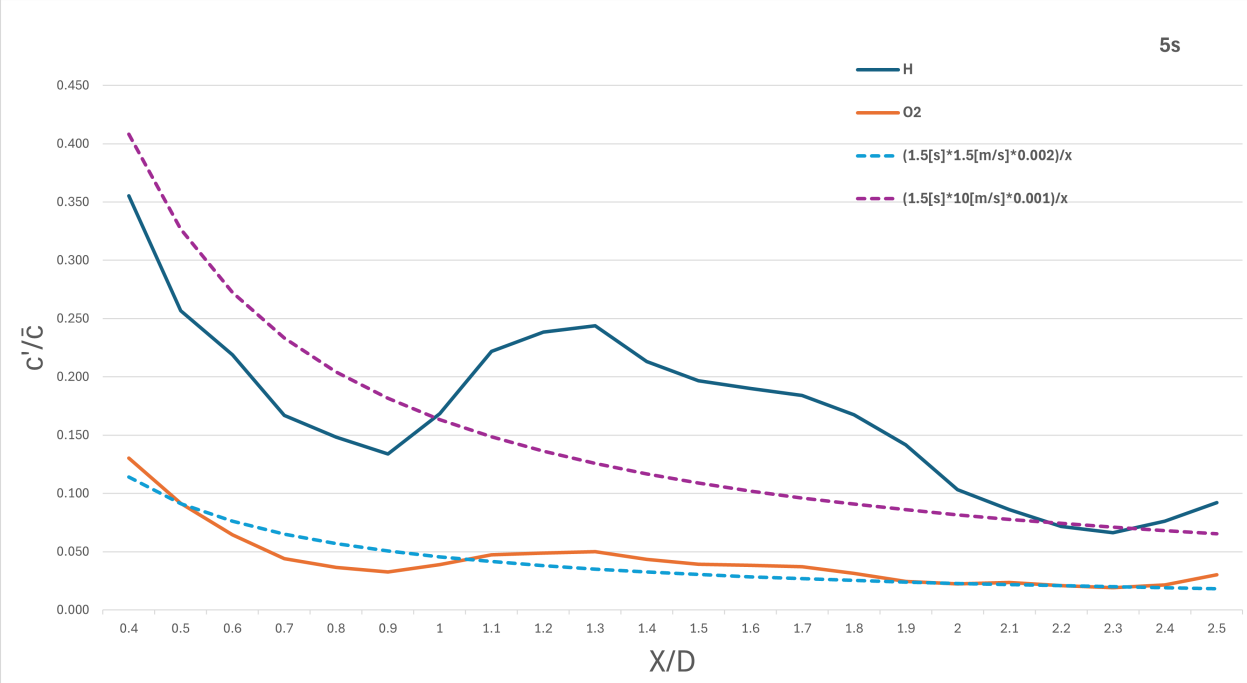

Figure 5.19: Fit to ratio of concentration fluctuations 5s into simulation

At approximately 1.1D normalized concentration fluctuations for oxygen is approximately 5%. The concentration fluctuations actually drop lower than 5% before 1.1D and between 0.7D to 1D. Indicating appreciable uniformly mixed gases to within about 5%. Further downstream, at 2.5D there is still good uniformity at about 6.5%.

The mean velocity over the entire cross section, $\overline{U_x} \sim 0.11 m/s$, in the downstream direction, is almost constant compared to the mean velocities in the y and z directions. The velocity in the y-axis follows the path of the inlet flow and the direction of gravity. The z-axis is the traverse of the y-axis. The most variations in the mean occur on the y-axis and z-axis.

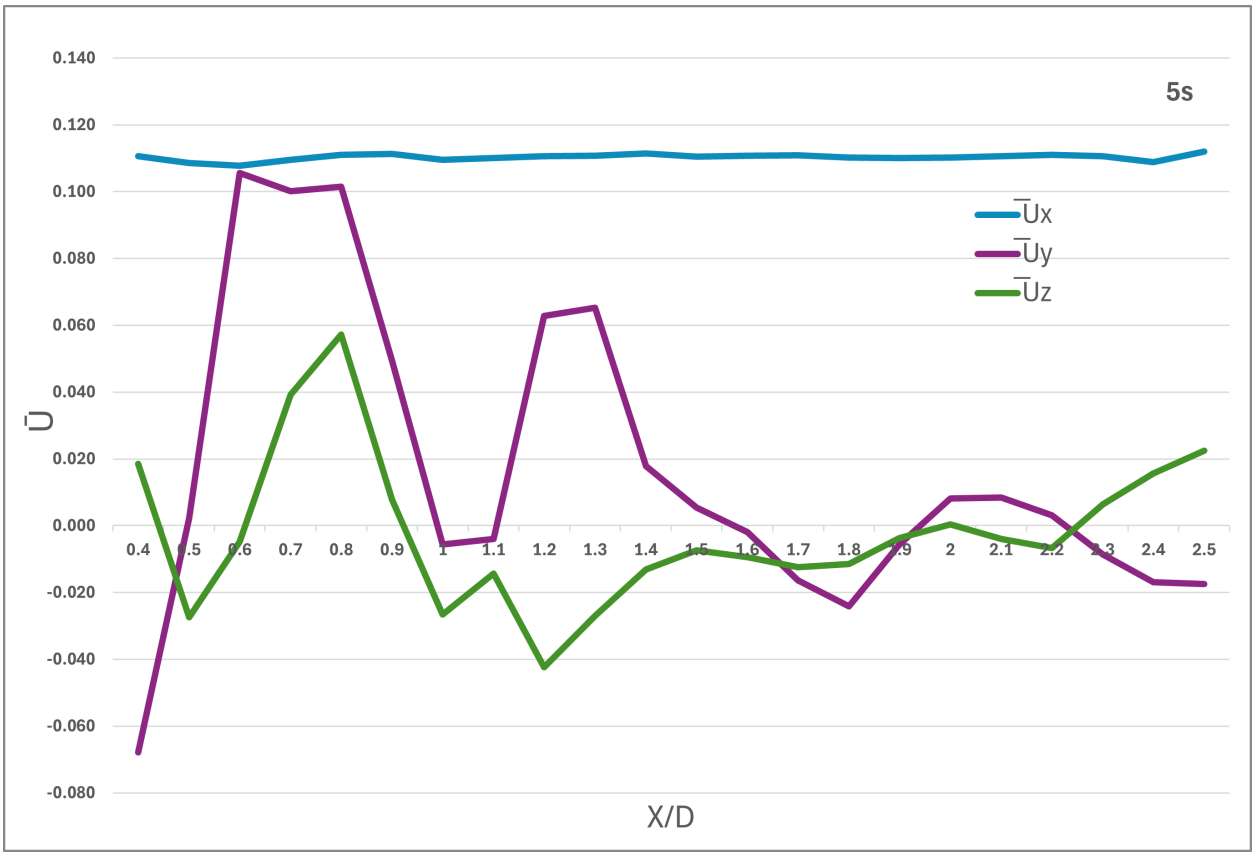

Figure 5.20: Mean velocity $\overline{U}$ at downstream cross sections 5s into simulation

The velocity fluctuations are represented in the standard deviation of the velocity, Figure 5.21. This shows a gradual drop-off in velocity fluctuations. As expected, the magnitudes of the velocity fluctuations for all three components are comparable.

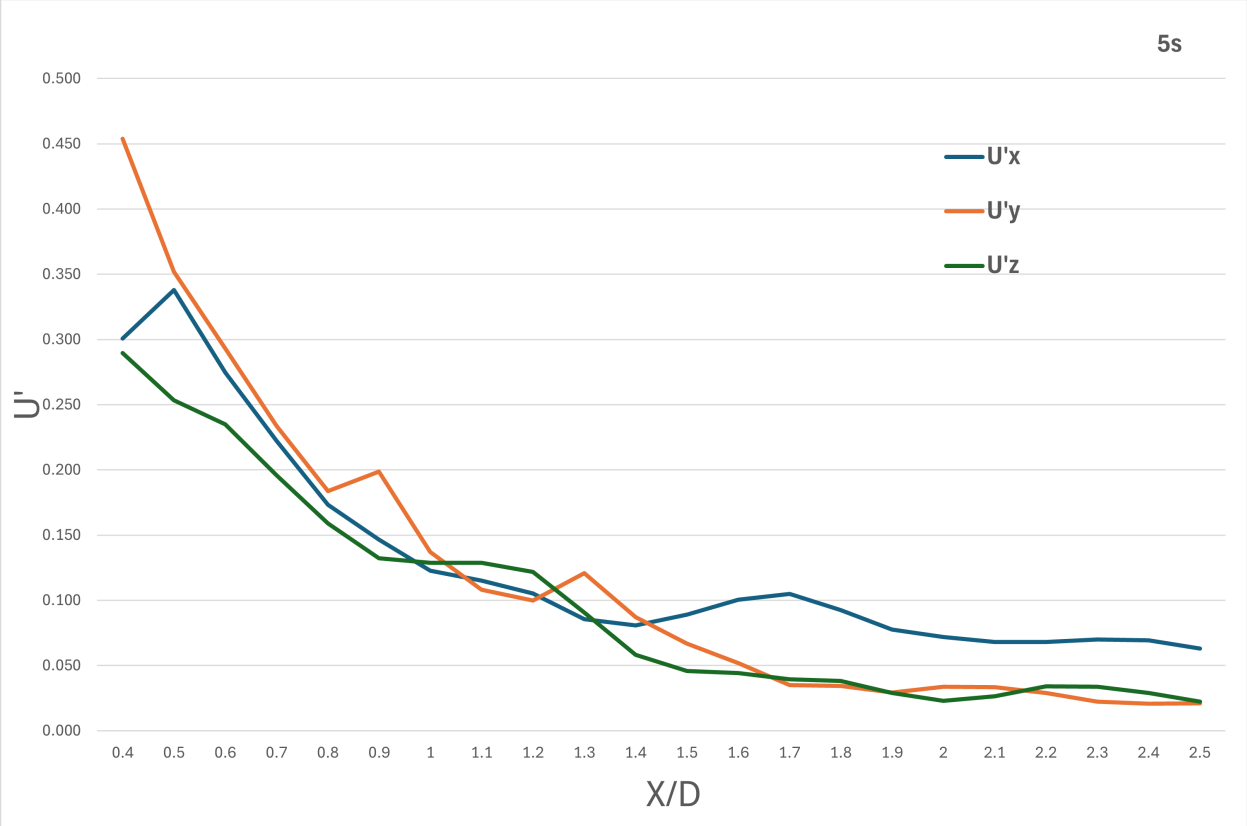

Figure 5.21: Standard deviation and fit of velocity U fluctuations at downstream cross sections 5s into simulation

The normalized velocity fluctuations are shown in Figure 5.22. Using the Galilean transformation, a similar 1/x trend was found in the velocity fluctuations. The x component of the velocity was used to normalize because the y and z components are constrained by the walls of the chamber. The average velocity is zero because the flow cannot pass through the walls.

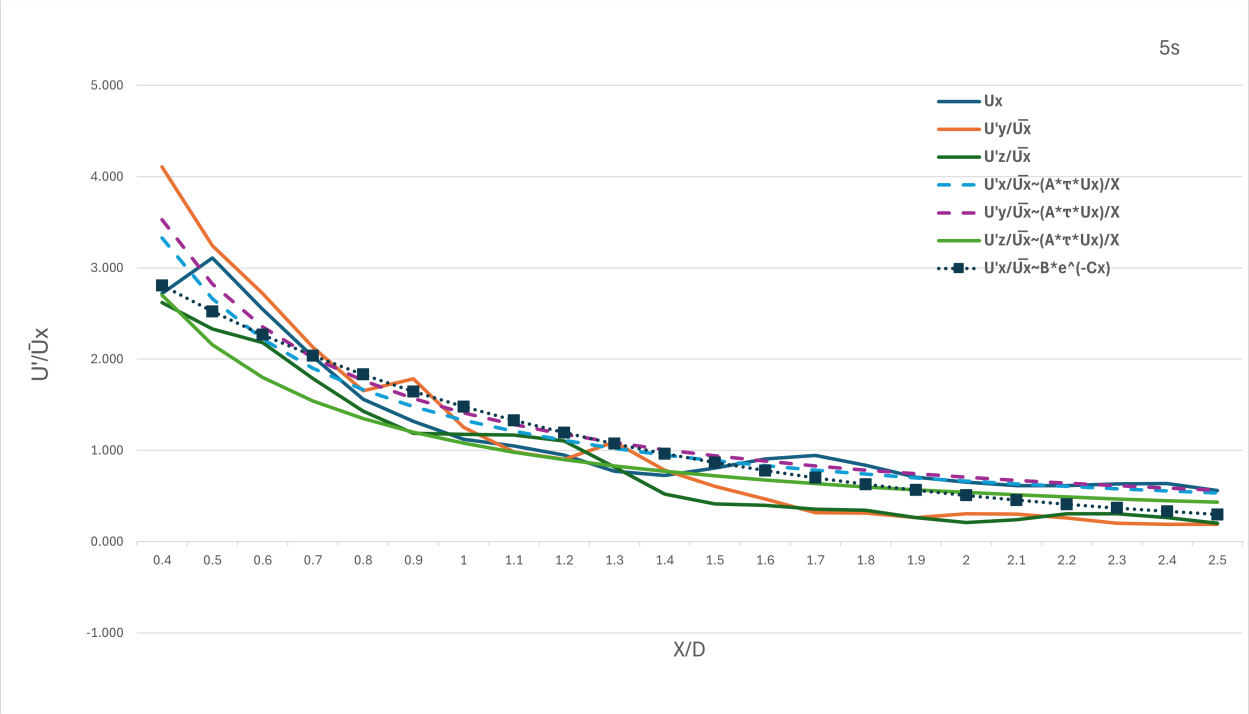

Figure 5.22: Normalized velocity fluctuation $U'/\overline{U}$ at downstream cross sections 5s into simulation

A fit of $(AU\tau)/X$ and Be^{CX} that were computed for the normalized with scaling terms A,B,C. The trends look comparable with the exponential fit slightly better results.

5.5 Mixing Time

The geometry under study has no streamwise flow before the transverse injection. The effective momentum ratio of transverse to axial momentum is relatively low and is determined by the volume flow rate of the injected gases. In this sense, it may not really be the momentum ratio that controls the mixing behavior but rather the ratio of the transverse momentum to the virtual momentum of the incident primary flow established by the volume flow rate and thus the residence time of the axial flow under the transverse jets.

Another difference with the experiment of Edwards et al. [4] is that while the present combustion chamber is two-dimensional, the mixing process is three-dimensional, at least close to the nozzles in the near field. Of course, if the combustion chamber was many diameters long, then the far-field flow many diameters from the injection nozzles would be two-dimensional. However, this far-field regime is not expected to be encountered in light and compact rocket engines and was not pursued in this research.

There are two theoretical regimes for injection behavior that were considered: short-pulse and long-pulse (Breidenthal et al.) [51]. In the long-pulse regime, the axial flow past the nozzles is sufficiently slow such that the counter-rotating vortex pair has grown to fill the entire cross section of the cylinder while still directly under the injection nozzles. The thrust force from the nozzles is thus the relevant physical property of the nozzles that determines the spinning up of the vortex pair. The long-pulse regime is defined by,

$$\tau_t >> \tau_v \tag{5.6}$$

where τ_t is the time interval in which the force due to the thrust of the nozzles acts on a Lagrangian fluid parcel flowing downstream in the cylinder, and τ_v is the time for the largest vortex to complete one full rotation.

The long-pulse regime is possible in the simulation if the injected fluid from the second nozzle impinges on the opposite wall directly below the second nozzle, see Figure 4.11. Conversely, if the injected fluid from the second nozzle impinges on the bottom of the chamber far downstream from the station of the second nozzle, this is the short-pulse regime.

In the short-pulse regime, the primary fluid is pushed downstream by a relatively large volume flow rate. The thrust of the nozzles only exerted a force on the fluid for a time interval much less than it took the vortex pair to grow to fill the cylinder. The short pulse regime corresponds to

$$\tau_t << \tau_v. \tag{5.7}$$

According to the simulations, each transverse jet penetrates across the entire diameter of the combustion chamber and impinges on the opposite wall directly below the respective injection nozzle. This implies that the mixer is operating in the long-pulse regime. Therefore, it is the jet thrust rather than the jet impulse that controls the mixing rate.

It follows from dimensional considerations that the characteristic mixing time τ must be the square root of the ratio of ρD^4 over the total jet thrust $\sum \rho_j V_j^2 A_j$, where ρ is the density of the mixed fluid and ρ_j is the density of the injected fluid. Of course, since there are two injected fluids, what matters is the total thrust of both of them added together.

Note that the injected fluid is subsonic in the present simulations, so the injected nozzle thrust is just the product of the mass flow rate and the injection velocity. However, if the injection is supersonic, then the total nozzle thrust would also need to account for the pressure term associated with any under- or over-expansion of each nozzle.

From Edwards et al. ([4]), the normalized concentration fluctuation $c'/\overline{c}$ is simply the characteristic mixing time τ divided by the elapsed time t following the flow. Assuming a Galilean transformation, the elapsed time t corresponds to the downstream station x for $t = x/U$, where U is the streamwise speed of the mixed fluid and $\overline{\rho}$ is the average density.

Thus

$$\frac{c'}{\overline{c}} = \frac{\tau}{t} = \frac{U_x}{x}\sqrt{\frac{\overline{\rho}D^4}{\sum \rho_j V_j^2 A_j}} \tag{5.8}$$

The plot of the normalized concentration fluctuations is plotted below. The theory has a dimensionless coefficient, which is implicitly assumed to be one. However, the theory is equally valid even if that dimensionless coefficient is approximately one or close to one. This can be used as a scaling term to perform a fit to the hydrogen and oxygen concentration fluctuation profiles. In the figure below, the theoretical concentration fluctuation from the long-pulse normalized concentration fluctuations of equation 5.8 is plotted in red. The blue and red dotted lines represent the fits of the theoretical normalized concentration with dimensionless coefficients A and B for the normalized fluctuations in hydrogen and oxygen concentrations. The solid lines are the simulated results for the hydrogen and oxygen normalized concentration fluctuations.

The dimensionless coefficients were A=0.15 and B=0.52. The theoretical plot in red predicts an appreciable alignment with the hydrogen concentration fluctuations between 1.3 and 1.8 diameters. However, there are higher concentration fluctuations for X/D below 1.3 and above 1.8.

The simulations reveal that good quality mixing is already realized in the near field at X/D of about 1 to 2. This suggests that a transverse injection design can achieve a light and efficient spacecraft engine. These results indicate that the theory is in approximate agreement with the near-field simulations, even though the theory was developed for the far field.

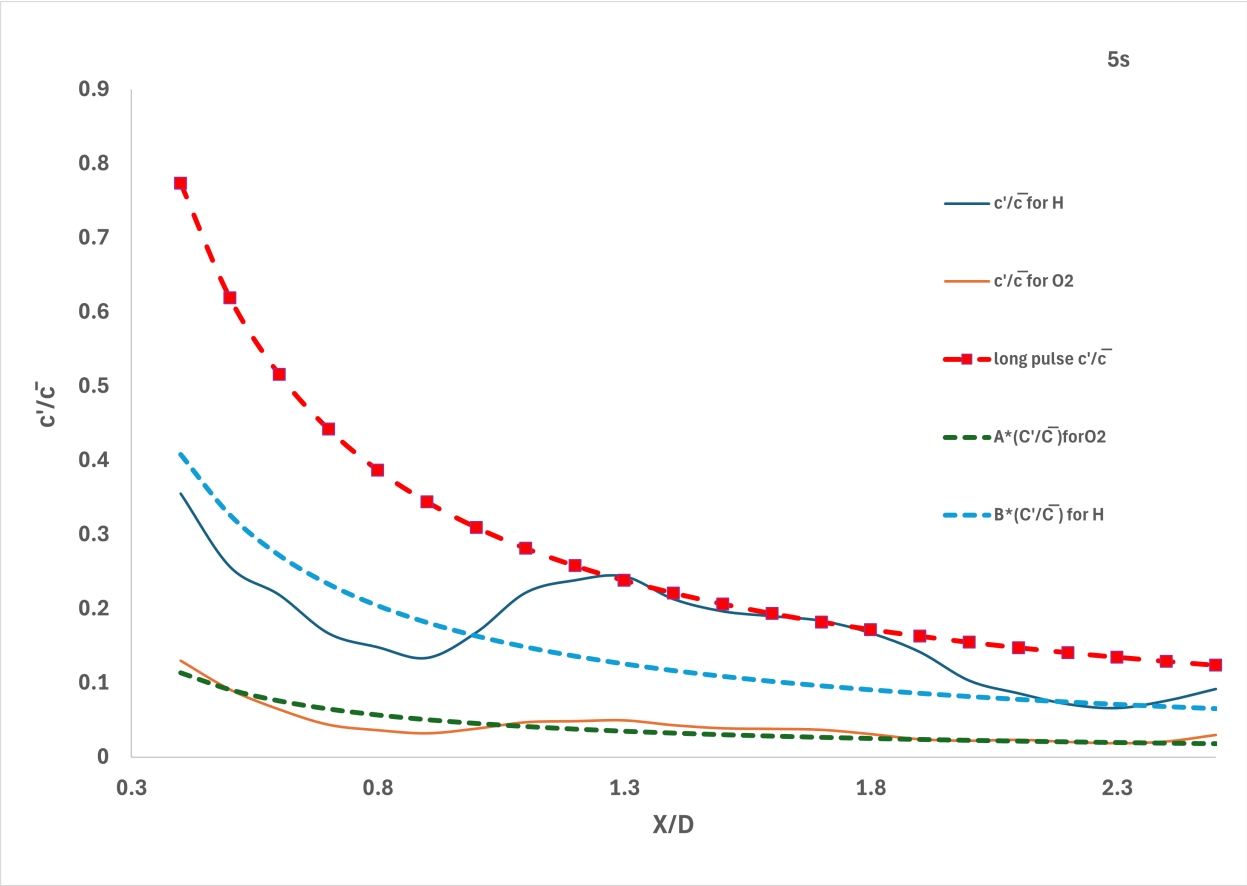

Figure 5.23: Long pulse normalized concentration fluctuations

The corresponding log-log graphs are plotted in Figure 5.24.

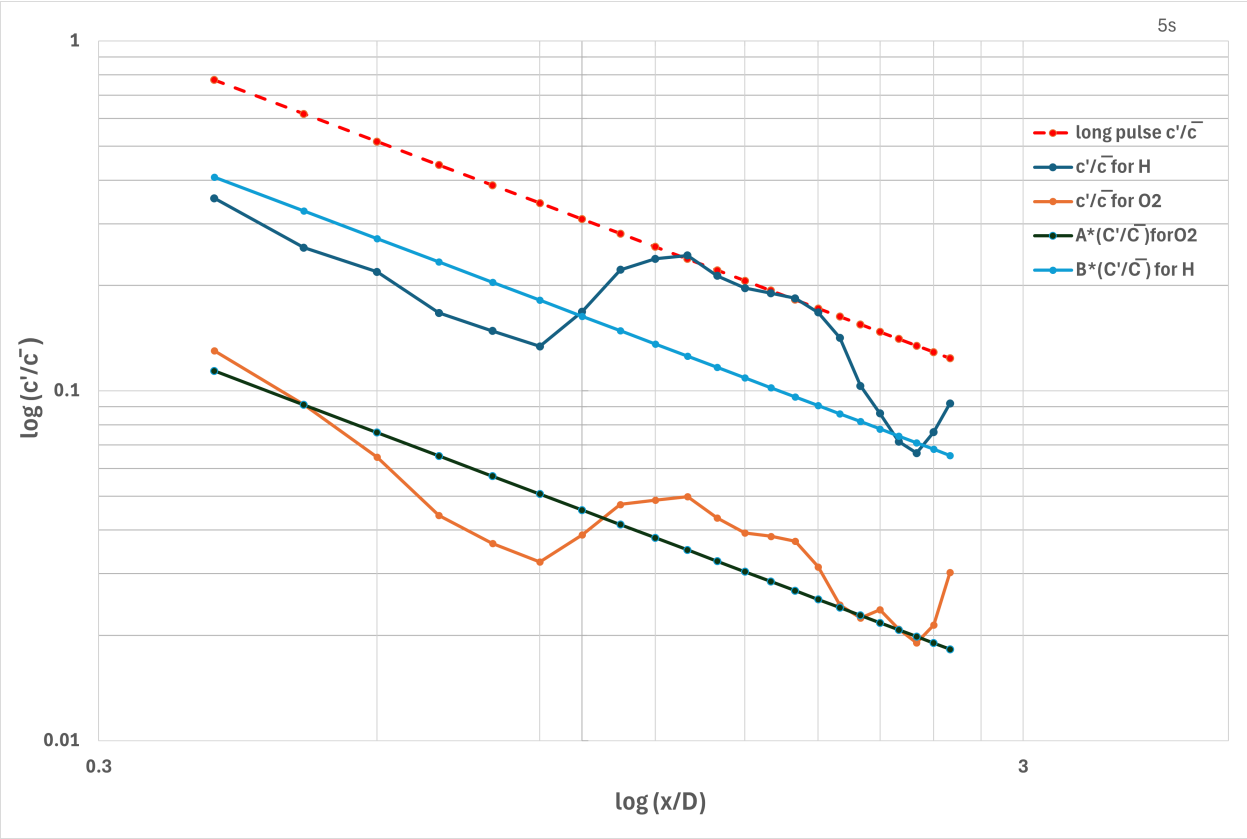

Figure 5.24: Log-log normalized concentration fluctuations

In summary, the characteristic mixing time and the behavior of the transverse jets were influenced by the interaction between the thrust force of the nozzles and the axial flow conditions within the combustion chamber, with distinct regimes defining the mixing characteristics. In the long pulse regime, the thrust force was the mechanism that continuously pushed the primary fluid and produced counterrotation in the flow.

5.6 Flammability Limits

The contours of the flammability limits of hydrogen can provide insight into the potential placement of an ignition source for combustion modeling. At 5s into the simulation, nitrogen has been

flushed out up to 1D. Figure 5.25, displays the rich flammability limit in red and the lean flammability limit in blue. The red limit is represented by the red contour at 4%, and the upper limit is the green contour at 75%.

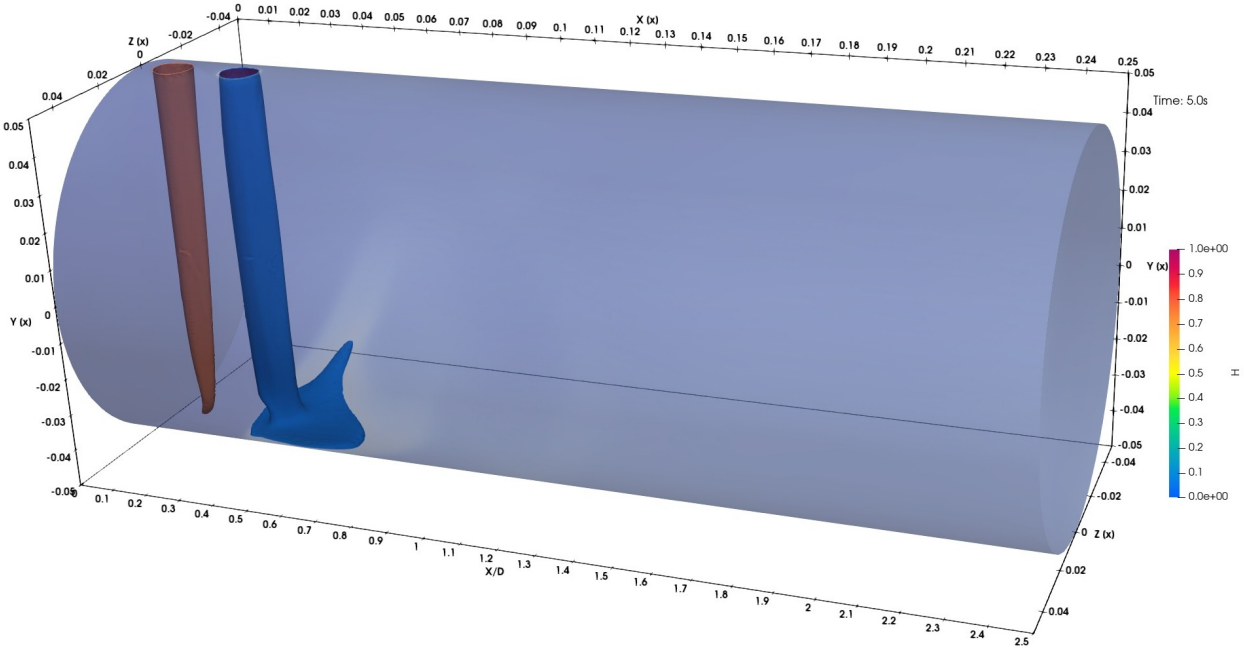

Figure 5.25: Flammability limits hydrogen, low limit is 4% represents as the blue contour and the high limit is 75% represented as the red contour

The red contour represents the upper flammability limit and follows the flow pattern from the hydrogen inlet. The blue contour represents the lean flammability limit and tracks the flow of the oxygen inlet down to where the flow impinges on the opposite wall. Neither of these locations is ideal for an ignition source.

Examining an intermediate contour, located approximately midway between the high and low contours, can provide insight into where the ignition source could rationally be placed. About 35% is approximately midway and is represented by the green contour in Figure 5.26.

Figure 5.27 shows contours both lower and higher than the median flammability limit. The contours are represented in translucent colors and between 35% and 25%. A contour of 50% is included in magenta to show where the upper end of the flammability trends. This shows that the

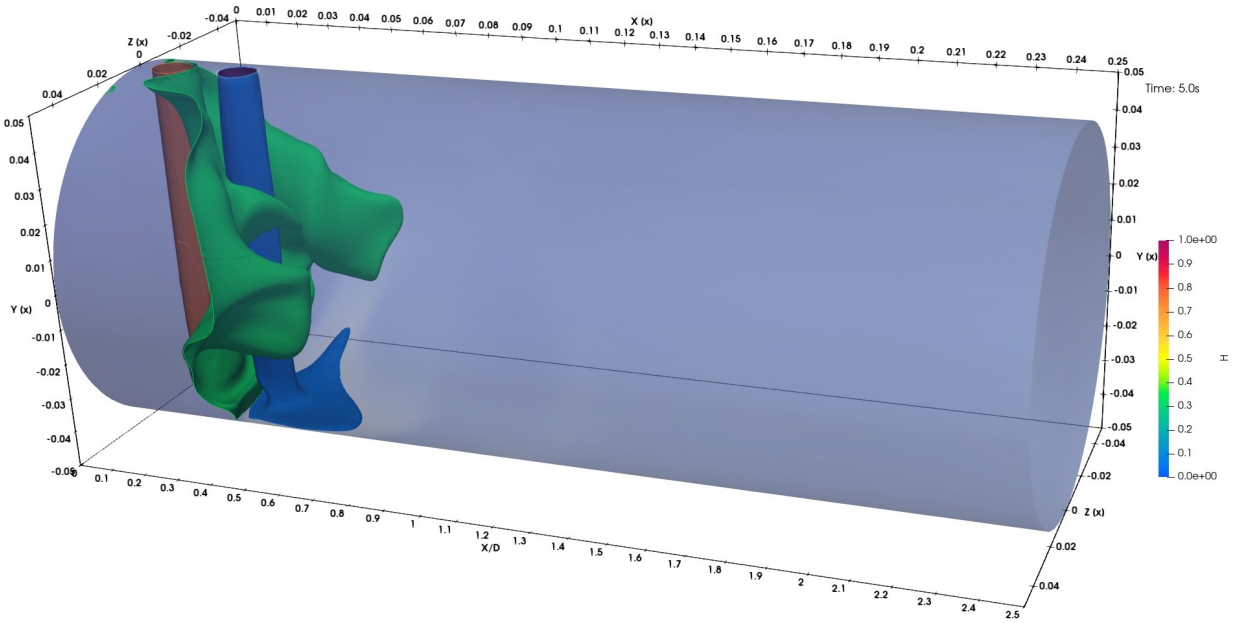

Figure 5.26: Flammability limits hydrogen with medium value of 35% in green

higher limit tends to move towards the hydrogen inlet and away from areas with lower concentration fluctuations. At about 25%, the translucent yellow contour crosses the 0.7D downstream station, where essentially all the gas is mixed to concentrations well within the flammability limits. The concentration of hydrogen at 0.7D is mostly centered between $\pm 0.03m$. An ignition source would be feasible at 0.7D for this geometry.

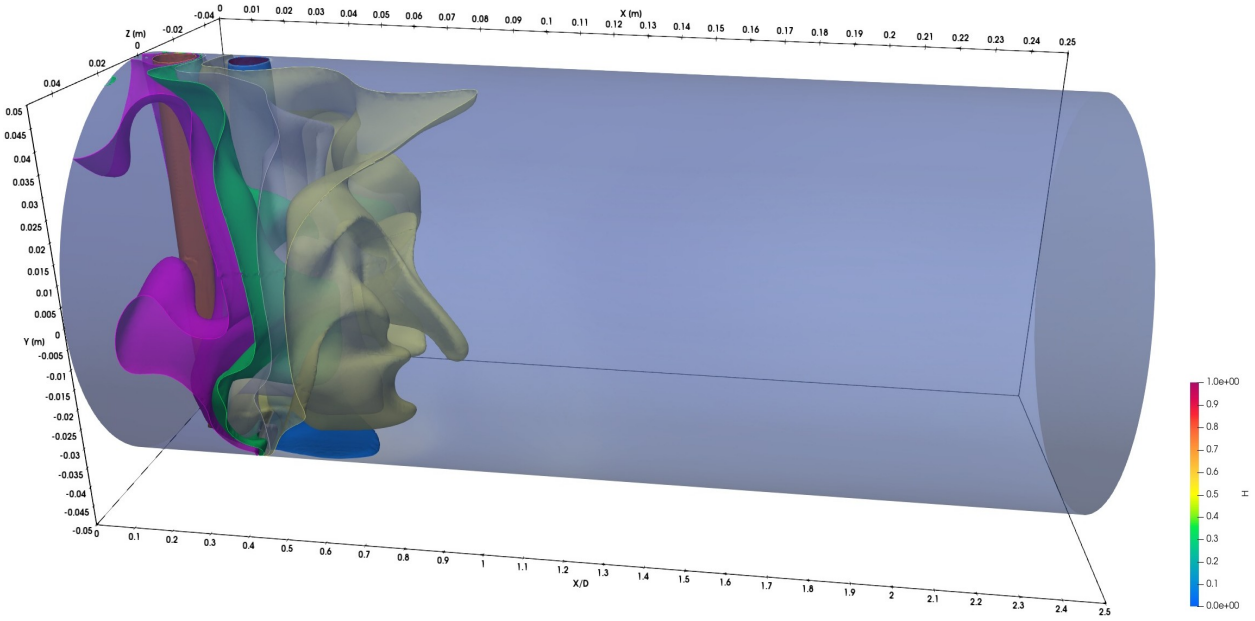

Figure 5.27: Flammability limits hydrogen concentration ranging from 50% to 25%

Chapter 6: Conclusion

6.0.1 Summary

DNS and LES simulations were compared to study the mixing behavior in a transverse jet combustion chamber configuration. Hydrogen and oxygen were selected as the test gases due to their highly combustible nature and common use in propulsion systems. However, combustion was disabled in the simulation to focus exclusively on the inert mixing behavior. This approach ensured that only the transport equations for species and other scalar and vector fields, such as velocity, density, mass fraction, and pressures, were active. By removing chemical reactions, the analysis was streamlined, and the computational complexity was reduced. Future work will explore the reacting case to build on these findings.

Chamber length optimization revealed that a range between 1D and 2.5D supports effective mixing while maintaining manageable computational grids. LES proved to be efficient for longer chambers, while DNS was feasible only for shorter configurations. At 1.3s, LES and DNS produced comparable results, validating LES as an appropriate method for studying inert mixing.

Simulations demonstrated that by 5s, nitrogen concentrations were fully purged, resulting in steady-state hydrogen and oxygen mixing. Counterrotating vortices, observed in streamline plots, contributed to rapid and efficient mixing. Gaussian distributions of equivalence ratios at 0.7D and 0.8D indicated fuel-rich mixtures in regions of near perfect mixing. Normalized concentration fluctuations followed the predicted 1/x trend, though minor deviations downstream suggested

residual ambient air effects or unaccounted interactions. Good quality mixing in the near field was observed at approximately 1D to 2D.

The geometry is a good candidate to avoid combustion instabilities. The simulations demonstrated the combustion chamber's ability to achieve rapid mixing within a compact region, vital for spacecraft design, as it reduces mass and minimizes heat transfer to the walls. This design mitigates dependency on regenerative cooling systems, simplifying engineering requirements. The presence of robust, counterrotating vortices enhances mixing efficiency while resisting the influence of pressure waves on the rate of heat release, offering a potential solution to reduce combustion instabilities in rocket motors. In addition, the broad flammability range of hydrogen and oxygen allows flexible placement of an ignitor, simplifying ignition design. The chamber may also act as a flameholder, stabilizing combustion without the need for continuous ignitor operation, thereby improving overall system efficiency and reliability.

6.0.2 Future work

Further development of the transverse rocket engine can take several directions:

- Conduct additional simulations with stoichiometric inlet flows to validate the regions of near perfect mixing observed in this study.
- Introduce an ignition source to the mesh. This can be implemented during a simulation restart, ensuring flameholding properties of the flow are tested. The ignition source location will likely be placed between 0.7D and 0.8D, where near perfect mixing occurs.
- Employ URANS (Unsteady Reynolds-Averaged Navier-Stokes) simulations as an intermediate step to capture time-dependent turbulence phenomena on coarser meshes. URANS could quickly estimate ignition source locations and averaged species compositions, guiding configurations for more detailed LES or DNS studies.

- Explore the flameholding capability of the flow to determine practical ignitor placement and ensure stable combustion during operation.

These future efforts aim to refine the simulation methodology, test reacting flows, and advance the design of transverse rocket engines.

Bibliography

[1] Garry L. Brown and Anatol Roshko. On density effects and large structure in turbulent mixing layers. *Journal of Fluid Mechanics*, 64(4):775–816, 1974.

[2] M.J Aarnio. Mixing by turbulent streamwise vortices confined in a duct. *Ph.D. thesis, University of Washington*, 1994.

[3] Donald Coles. Prospects for useful research on coherent structure in turbulent shear flow. *Proceedings of the Indian Academy of Sciences Section C: Engineering Sciences*, 4:111–127, 1981.

[4] AC Edwards, WD Sherman, and RE Breidenthal. Turbulent mixing in tubes with transverse injection. *AIChE journal*, 31(3):516–518, 1985.

[5] Robert E Breidenthal, Kwok-On Tong, Grant S Wong, Rolf D Hamerquist, and Peter B Landry. Turbulent mixing in two-dimensional ducts with transverse jets. *AIAA journal*, 24(11):1867–1869, 1986.

[6] Jacob A Boening, Eric A Wheeler, Joseph D Heath, James V Koch, Arthur T Mattick, Robert E Breidenthal, Carl Knowlen, and Mitsuru Kurosaka. Rotating detonation engine using a wave generator and controlled mixing. *Journal of Propulsion and Power*, 34(6):1364–1375, 2018.

[7] J. E. Broadwell and R. E. Breidenthal. A simple model of mixing and chemical reaction in a turbulent shear layer. *Journal of Fluid Mechanics*, 125:397–410, 1982.

[8] Suman Muppidi and Krishnan Mahesh. Two-dimensional model problem to explain counter-rotating vortex pair formation in a transverse jet. *Physics of Fluids*, 18(8):085103, 08 2006.

[9] J. E. Broadwell and R. E. Breidenthal. Structure and mixing of a transverse jet in incompressible flow. *Journal of Fluid Mechanics*, 148:405–412, 1984.

[10] Jacob A Boening, Joseph D Heath, Trever J Byrd, James V Koch, Arthur T Mattick, Robert E Breidenthal, Carl Knowlen, and Mitsuru Kurosaka. Design and experiments of a continuous rotating detonation engine: a spinning wave generator and modulated fuel/oxidizer mixing. In *52nd AIAA/SAE/ASEE Joint Propulsion Conference*, page 4966, 2016.

[11] Parviz Moin and Krishnan Mahesh. Direct numerical simulation: A tool in turbulence research. *Annu. Rev. Fluid Mech.*, 30:539–578, 01 1998.

[12] Robert D. Moser and Parviz Moin. The effects of curvature in wall-bounded turbulent flows. *Journal of Fluid Mechanics*, 175:479–510, 1987.

[13] Nils T. Basse. Turbulence intensity scaling: A fugue. *Fluids*, 4(4):180, October 2019.

[14] S.B. Pope. *Turbulent Flows*. Cambridge University Press, 2000.

[15] I. Wygnanski and H. Fiedler. Some measurements in the self-preserving jet. *Journal of Fluid Mechanics*, 38(3):577–612, 1969.

[16] Christophe Bogey and Christophe Bailly. Turbulence and energy budget in a self-preserving round jet: direct evaluation using large eddy simulation. *Journal of Fluid Mechanics*, 627:129 – 160, 2009.

[17] Brian Edward Launder and Bahrat I Sharma. Application of the energy-dissipation model of turbulence to the calculation of flow near a spinning disc. *Letters in heat and mass transfer*, 1(2):131–137, 1974.

[18] Fiona Spencer, Giovanni Nino, Janna Wai, Jonathan M Wai, and Robert Breidenthal. Mixing in a novel rocket engine. In *AIAA SCITECH 2024 Forum*, page 0346, 2024.

[19] Wolfgang Rodi. Experience with two-layer models combining the k-epsilon model with a one-equation model near the wall. In *29th Aerospace sciences meeting*, page 216, 1991.

[20] MENTER FR. Two-equation eddy-viscosity turbulence models for engineering applications. *AIAA J*, 32:269–289, 1994.

[21] ANSYS Fluent et al. Ansys fluent theory guide. *Ansys Inc., USA*, 15317:724–746, 2011.

[22] Joel H Ferziger and Milovan Perić. *Computational methods for fluid dynamics*. Springer, 2002.

[23] Stephen R Turns et al. *Introduction to combustion*, volume 287. McGraw-Hill Companies New York, NY, USA, 1996.

[24] Si Ok Ryu, S. M. Hwang, and Martin Jay Rabinowitz. Shock tube and modeling study of the H + O2 = OH + O reaction over a wide range of composition, pressure, and temperature. *The Journal of Physical Chemistry*, 99:13984–13991, 1995.

[25] Zekai Hong, David Davidson, E.A. Barbour, and R.K. Hanson. A new shock tube study of the H+O2→OH+O reaction rate using tunable diode laser absorption of H2O near 2.5μm. *Proceedings of the Combustion Institute*, 33:309–316, 12 2011.

[26] Garry L Schott. Further studies of exponential branching rates in reflected-shock heated, nonstoichiometric H2COO2 systems. *Combustion and Flame*, 21(3):357–370, 1973.

[27] Nobuyuki Fujii and Kuan S Shin. Rate constant for H+ O2→ O+ OH by laser absorption spectroscopy of oh in shock-heated h2-o2-ar mixtures. *Chemical physics letters*, 151(4-5):461–465, 1988.

[28] H Yang, WC Gardiner, KS Shin, and N Fujii. Shock tube study of the rate coefficient of H+ O2→ OH+ O. *Chemical physics letters*, 231(4-6):449–453, 1994.

[29] Alexander A Konnov. Remaining uncertainties in the kinetic mechanism of hydrogen combustion. *Combustion and flame*, 152(4):507–528, 2008.

[30] Priyank Saxena and Forman A Williams. Testing a small detailed chemical-kinetic mechanism for the combustion of hydrogen and carbon monoxide. *Combustion and Flame*, 145(1-2):316–323, 2006.

[31] Charles K Westbrook and Frederick L Dryer. Chemical kinetic modeling of hydrocarbon combustion. *Progress in energy and combustion science*, 10(1):1–57, 1984.

[32] Kuan S Shin and JV Michael. Rate constants for the reactions H+ O2→ OH+ O and D+ O2→ OD+ O over the temperature range 1085–2278K by the laser photolysis–shock tube technique. *The Journal of chemical physics*, 95(1):262–273, 1991.

[33] Gregory P. Smith, David M. Golden, Michael Frenklach, Nigel W. Moriarty, Boris Eiteneer, Mikhail Goldenberg, C. Thomas Bowman, Ronald K. Hanson, Soonho Song, William C. Gardiner Jr, Vitali V. Lissianski, and Zhiwei Qin. Gri-mech 3.0: A detailed chemical kinetics mechanism for natural gas combustion. `http://combustion.berkeley.edu/gri-mech/version30/text30.html`. Gas Research Institute, Accessed: 2025-03-09.

[34] William Sutherland. Lii. the viscosity of gases and molecular force. *The London, Edinburgh, and Dublin Philosophical Magazine and Journal of Science*, 36(223):507–531, 1893.

[35] Frank M White and Joseph Majdalani. *Viscous fluid flow*, volume 3. McGraw-Hill New York, 2006.

[36] Jr. M. W. Chase. *NIST-JANAF Thermochemical Tables, 4th Edition*. American Institute of Physics, 1998. National Institute of Standards and Technology.

[37] Yang Li, Adamu Alfazazi, Balaji Mohan, Efstathios Alexandros Tingas, Jihad Badra, Hong G Im, and S Mani Sarathy. Development of a reduced four-component (toluene/n-heptane/iso-octane/ethanol) gasoline surrogate model. *Fuel*, 247:164–178, 2019.

[38] Randall J LeVeque. *Finite difference methods for ordinary and partial differential equations: steady-state and time-dependent problems*. SIAM, 2007.

[39] Noor Muhammad, F. D. Zaman, and M. T. Mustafa. OpenFOAM for computational combustion dynamics. *European Physical Journal Special Topics*, 231(13-14):2821–2835, September 2022.

[40] John Charles Butcher. *Numerical methods for ordinary differential equations*. John Wiley & Sons, 2016.

[41] Henk Kaarle Versteeg. *An introduction to computational fluid dynamics the finite volume method, 2/E*. Pearson Education India, 2007.

[42] Joel H Ferziger, Milovan Perić, and Robert L Street. *Computational methods for fluid dynamics*. springer, 2019.

[43] OpenFOAM Foundation. *OpenFOAM v11 User Guide: Numerical Schemes*, 2023. `https://doc.cfd.direct/openfoam/user-guide-v11/fvschemes`.

[44] Fadl Moukalled, Luca Mangani, Marwan Darwish, F Moukalled, L Mangani, and M Darwish. *The finite volume method*. Springer, 2016.

[45] Jiri Blazek. *Computational fluid dynamics: principles and applications*. Butterworth-Heinemann, 2015.

[46] S Bose, Parviz Moin, and Frank Ham. Explicitly filtered large eddy simulation on unstructured grids. *Annual Research Briefs (Center For Turbulence Research)*, 01 2011.

[47] T. Bose. Explicitly filtered large-eddy simulation : with application to grid adaptation and wall modeling. *Ph.D. thesis, University of Washington*, 2012.

[48] Lars Davidson. Large eddy simulations: How to evaluate resolution. *International Journal of Heat and Fluid Flow*, 30(5):1016–1025, 2009. The 3rd International Conference on Heat Transfer and Fluid Flow in Microscale.

[49] Hauke Wurps, Gerald Steinfeld, and Stefan Heinz. Grid-resolution requirements for large-eddy simulations of the atmospheric boundary layer. *Boundary-Layer Meteorology*, 175(2):179–201, 2020.

[50] Stephen B Pope. Ten questions concerning the large-eddy simulation of turbulent flows. *New journal of Physics*, 6(1):35, 2004.

[51] RE Breidenthal, VR Buonadonna, and MF Weisbach. Molecular mixing via jets in confined volumes. *Journal of fluid mechanics*, 219:531–544, 1990.

Chapter A: Appendix One

Physical properties configuration file physicalProperties file in OpenFOAM specifies the physical properties of the reactants in the combustion simulation. The type of thermophysical model was configured to the hePsiThermo model, enthalpy based thermophysical model for compressibility.

```
/*--------------------------------*- C++ -*----------------------*\
  =========                 |
  \\      /  F ield         | OpenFOAM: The Open Source CFD Toolbox
   \\    /   O peration     | Website:  https://openfoam.org
    \\  /    A nd           | Version:  12
     \\/     M anipulation  |
\*---------------------------------------------------------------*/
FoamFile
{
    format      ascii;
    class       dictionary;
    location    "constant";
    object      physicalProperties;
}
// * * * * * * * * * * * * * * * * * * * * * * * * * * * * * * * * *//

thermoType
{
    type            hePsiThermo;
```

```
    mixture         multicomponentMixture;
    transport       sutherland;
    thermo          janaf;
    energy          sensibleEnthalpy;
    equationOfState perfectGas;
    specie          specie;
}

defaultSpecie N2;

#include "thermo" //from GRI-mech
// ************************************************************//
```

Chapter B: Appendix Two

Chemistry properties configuration file combustionProperties defined the settings and parameters for combustion modeling.

```
/*---------------------------------*- C++ -*-------------------------*\
  =========                 |
  \\      /  F ield         | OpenFOAM: The Open Source CFD Toolbox
   \\    /   O peration     | Website:  https://openfoam.org
    \\  /    A nd           | Version:  12
     \\/     M anipulation  |
\*-----------------------------------------------------------------*/
FoamFile
{
    format          ascii;
    class           dictionary;
    location        "constant";
    object          chemistryProperties;
}
// * * * * * * * * * * * * * * * * * * * * * * * * * * * * * * * * * * * *//

chemistryType
{
    solver          ode;
}
```

```
chemistry       off;

initialChemicalTimeStep 1e-07;

odeCoeffs
{
    solver          seulex;
    absTol          1e-08; //tuneable
    relTol          0.1;  //tunable, 0.01
}

//#include "reactionsGRI"

reactions
{
 un-named-reaction-37
    {
        type            reversibleArrhenius;
        reaction        "H + O2 = O + OH";
        A               2.65e+10; //most sensitive one,can change any of these 3
        beta            -0.6707;
        Ta              8574.881901;
    }
}
// ************************************************************************//
```

Chapter C: Appendix Three

C.1 Numerical schemes for DNS and LES

The fvSchemes file in OpenFOAM is a configuration file that specifies the numerical schemes used for different terms in the numerical simulations and governing equations. The file is located in the system directory in OpenFOAM and case setup and defines various discretization schemes used in DNS and LES, as well as other types of simulations. The numerical are configured as shown below,

```
/*--------------------------------*- C++ -*----------------------*\
  =========                 |
  \\      /  F ield         | OpenFOAM: The Open Source CFD Toolbox
   \\    /   O peration     | Website:  https://openfoam.org
    \\  /    A nd           | Version:  12
     \\/     M anipulation  |
\*---------------------------------------------------------------*/
FoamFile
{
    version     2.0;
    format      ascii;
    class       dictionary;
    location    "system";
    object      fvSchemes;
```

```
}
// * * * * * * * * * * * * * * * * * * * * * * * * * * * * * * * * * * * * //

ddtSchemes
{
    default         Euler;
}
gradSchemes
{

    default         Gauss linear; //DNS and LES

}
divSchemes
{
    default         none;

        div(phi,U)          Gauss limitedLinearV 1;
        div(phi,Yi_h)       Gauss limitedLinear 1;
        div(phi,K)          Gauss limitedLinear 1;
        div(phid,p)         Gauss limitedLinear 1;
        div(phi,epsilon)    Gauss limitedLinear 1;
        div(phi,k)          Gauss limitedLinear 1;
        div(phi,e)          Gauss LUST grad(e);

    div(((rho*nuEff)*dev2(T(grad(U))))) Gauss linear;
}
laplacianSchemes
{
    default         Gauss linear orthogonal; //DNS and LES
}
```

```
interpolationSchemes
{
    default         linear;
}
snGradSchemes
{
    default corrected; //DNS and LES
}
// ************************************************************//
```

Chapter D: Appendix Four

D.1 Mean concentration at 5s into simulation

The average, $\bar{c}$ of the concentrations over the entire cross section

X/D	average H	average O2	average N2	sum of concentrations
0.4D	0.267	0.731	0.002	1
0.5D	0.254	0.744	0.002	1
0.6D	0.227	0.771	0.002	1
0.7D	0.207	0.790	0.003	1
0.8D	0.196	0.801	0.003	1
0.9D	0.194	0.802	0.004	1
1.0D	0.187	0.809	0.005	1
1.1D	0.173	0.821	0.005	1
1.2D	0.165	0.829	0.006	1
1.3D	0.167	0.825	0.008	1
1.4D	0.177	0.812	0.011	1
1.5D	0.177	0.809	0.014	1
1.6D	0.175	0.810	0.015	1
1.7D	0.176	0.808	0.016	1
1.8D	0.178	0.804	0.018	1

1.9D	0.172	0.806	0.022	1
2.0D	0.161	0.814	0.025	1
2.1D	0.157	0.814	0.029	1
2.2D	0.159	0.807	0.034	1
2.3D	0.163	0.798	0.039	1
2.4D	0.164	0.789	0.048	1
2.5D	0.162	0.777	0.060	1

D.2 Concentration fluctuation at 5s

The standard deviation is the concentration fluctuation c'.

X/D	c'(H)	c'(O2)	c'(N2)
0.4D	0.095	0.095	0.001
0.5D	0.065	0.068	0.001
0.6D	0.050	0.050	0.001
0.7D	0.035	0.035	0.001
0.8D	0.029	0.029	0.003
0.9D	0.026	0.026	0.003
1.0D	0.031	0.031	0.004
1.1D	0.038	0.039	0.004
1.2D	0.039	0.040	0.005
1.3D	0.041	0.041	0.006
1.4D	0.038	0.035	0.008
1.5D	0.035	0.032	0.010
1.6D	0.033	0.031	0.012
1.7D	0.032	0.030	0.013

1.8D	0.030	0.025	0.014
1.9D	0.024	0.020	0.015
2.0D	0.017	0.018	0.016
2.1D	0.014	0.019	0.017
2.2D	0.011	0.017	0.018
2.3D	0.011	0.015	0.020
2.4D	0.012	0.017	0.026
2.5D	0.015	0.024	0.036

D.3 Ratio of concentration fluctuations and mean $c'/\overline{c}$ at 5s.

X/D	H	O2	N2
0.4D	0.355	0.130	0.469
0.5D	0.257	0.091	0.442
0.6D	0.219	0.065	0.461
0.7D	0.167	0.044	0.541
0.8D	0.148	0.037	0.739
0.9D	0.134	0.032	0.803
1.0D	0.168	0.039	0.818
1.1D	0.222	0.047	0.865
1.2D	0.238	0.049	0.900
1.3D	0.244	0.050	0.809
1.4D	0.213	0.043	0.684
1.5D	0.197	0.039	0.742
1.6D	0.190	0.038	0.784

1.7D	0.184	0.037	0.812
1.8D	0.167	0.031	0.774
1.9D	0.142	0.024	0.692
2.0D	0.103	0.022	0.632
2.1D	0.086	0.024	0.576
2.2D	0.072	0.021	0.518
2.3D	0.066	0.019	0.517
2.4D	0.076	0.021	0.552
2.5D	0.092	0.030	0.597

Chapter E: Appendix 5

Normalized PDF of concentration at every 0.1D cross section downstream of the inlets

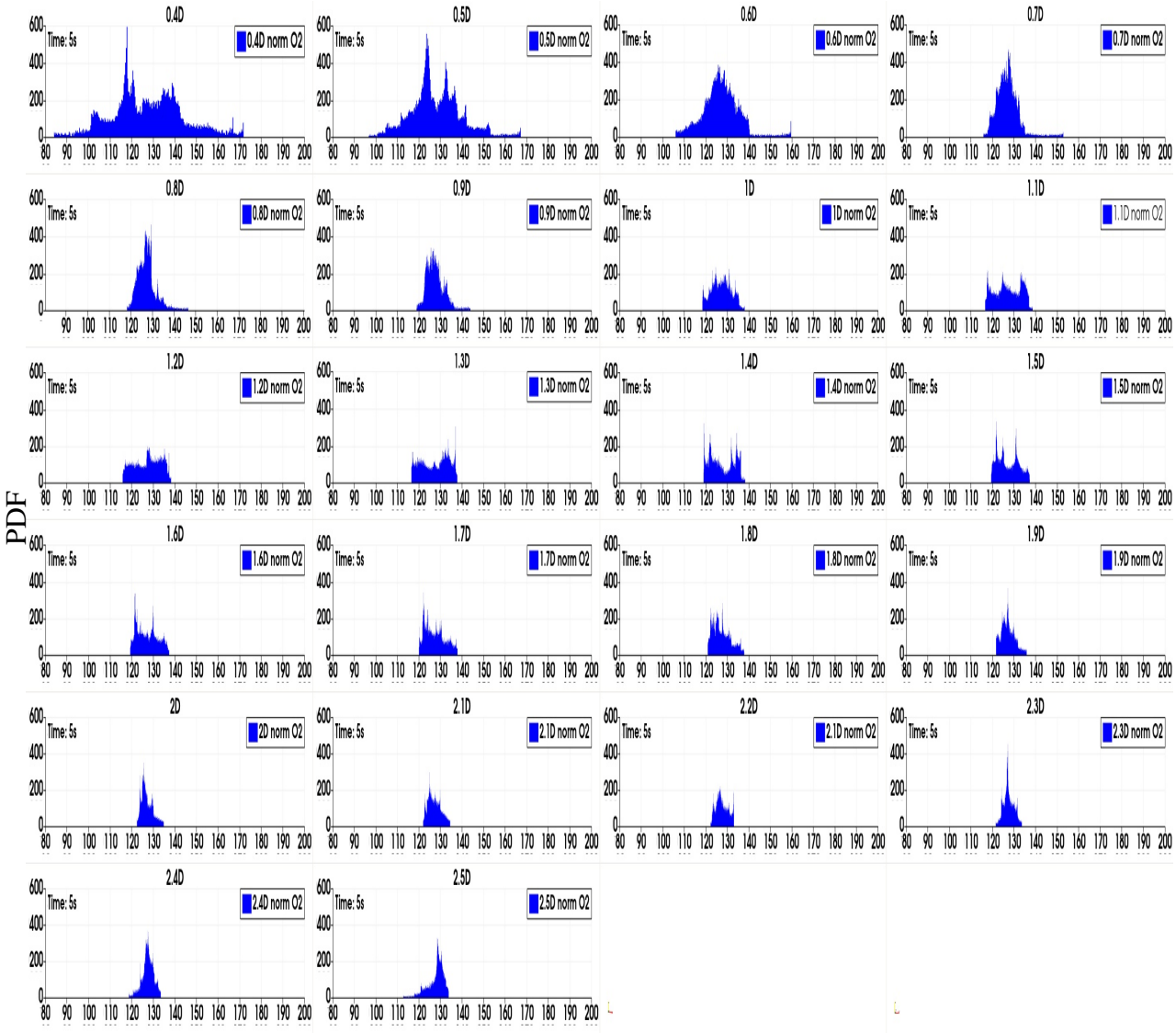

Figure E.1: Normalized PDF of oxygen concentration at 5s for cross-section profiles downstream of inlets with combustion chamber L=0.25m, x-axis represents the nitrogen mass fraction and the y-axis represents the frequency.

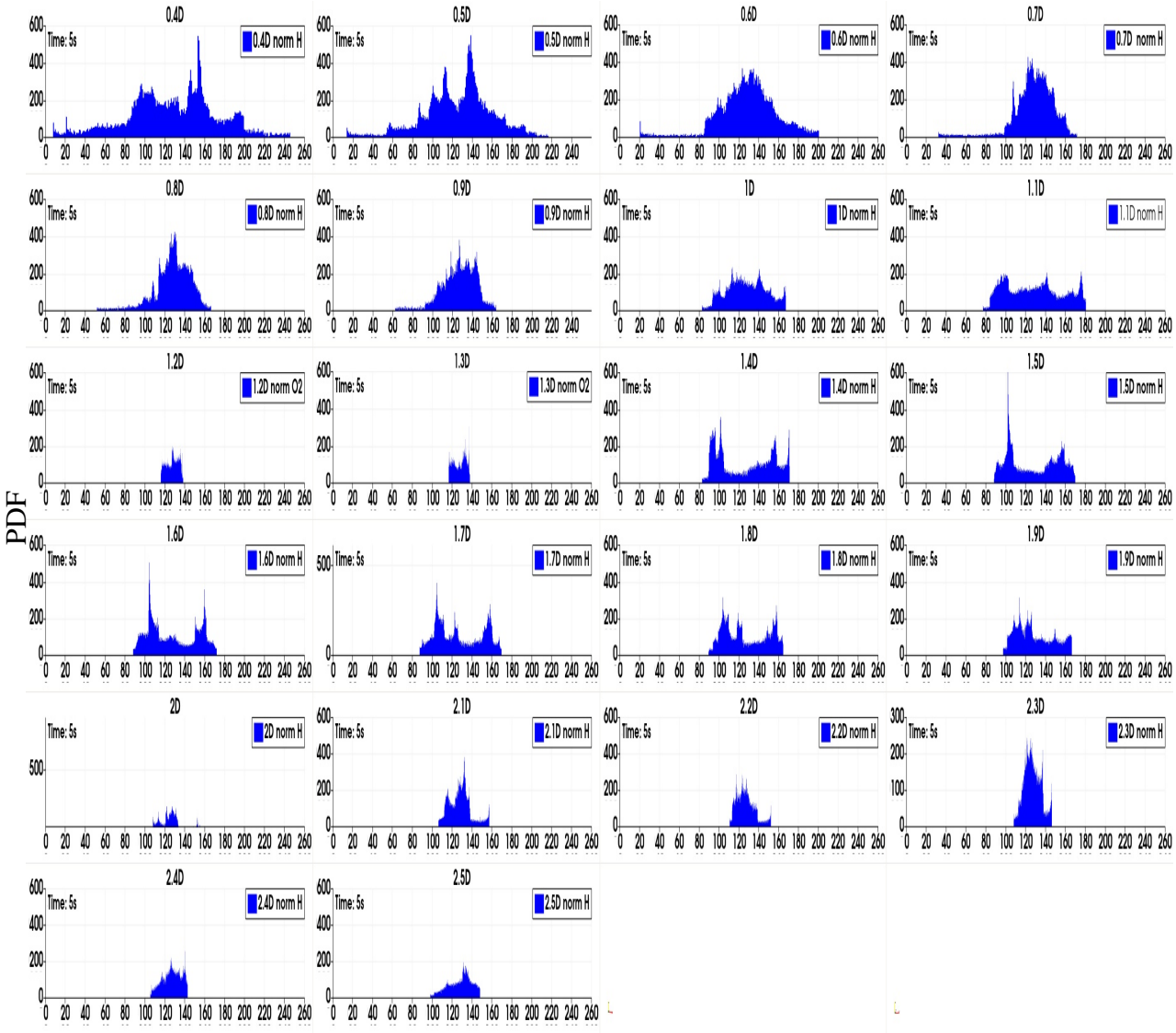

Figure E.2: Normalized PDF of nitrogen concentration at 5s for cross-section profiles downstream of inlets with combustion chamber L=0.25m, x-axis represents the nitrogen mass fraction and the y-axis represents the frequency.

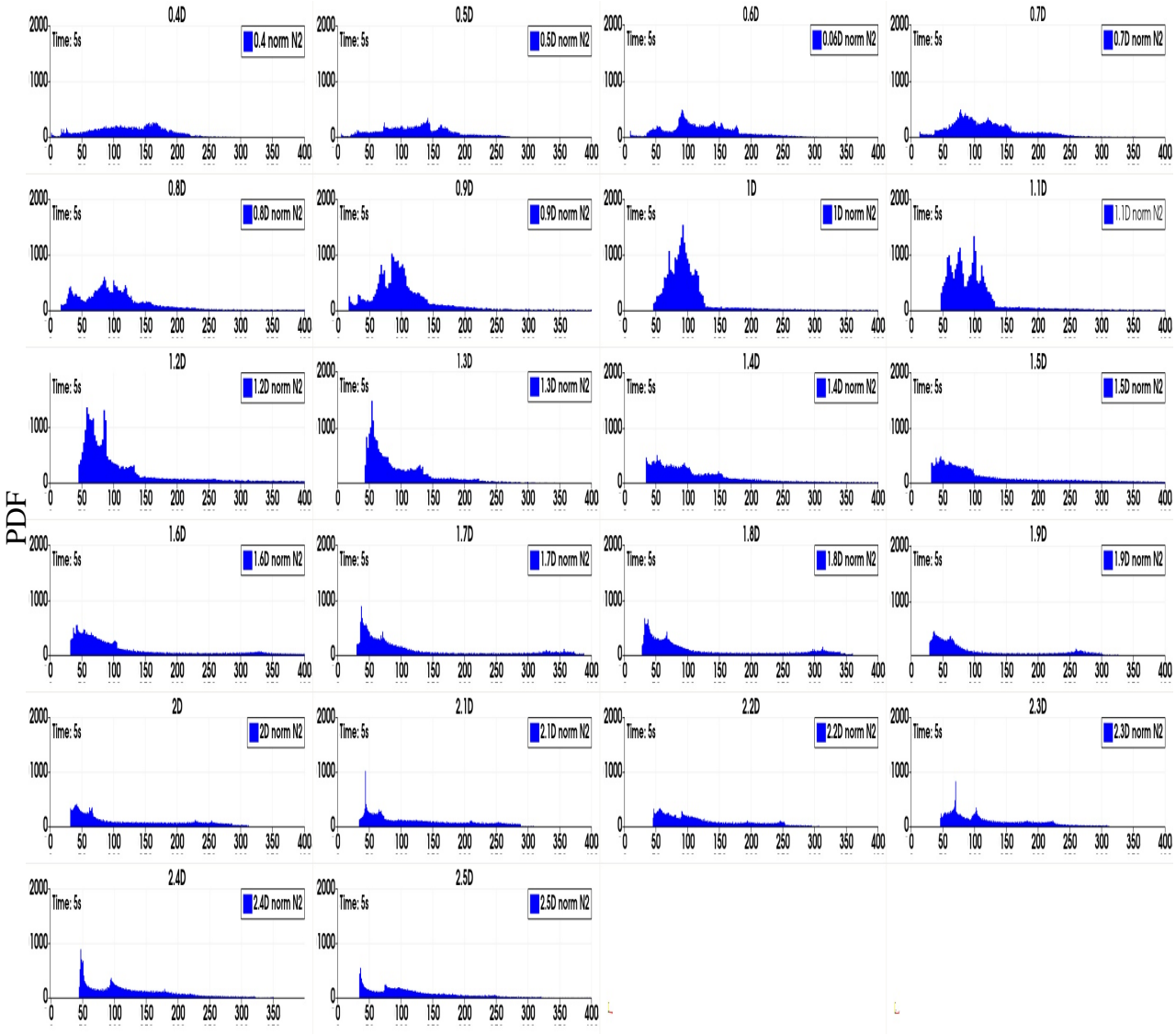

Figure E.3: Normalized PDF of nitrogen concentration at 5s for cross-section profiles downstream of inlets with combustion chamber L=0.25m, x-axis represents the nitrogen mass fraction and the y-axis represents the frequency.